UNIVERSITY OF CALIFORNIA SAN DIEGO

Interactions between Large-Scale Oscillatory Flows and Bathymetry

A dissertation submitted in partial satisfaction of the
requirements for the degree
Doctor of Philosophy

in

Oceanography

by

Isabella Beatriz Arzeno

Committee in charge:

Sarah N. Giddings, Co-Chair
Geno R. Pawlak, Co-Chair
Peter J. S. Franks
Jan Kleissl
Julie L. McClean
Robert Pinkel

2020

The dissertation of Isabella Beatriz Arzeno is approved, and it is acceptable in quality and form for publication on microfilm and electronically:

_____

_____

_____

_____

_____
Co-Chair

_____
Co-Chair

University of California San Diego

2020

DEDICATION

This dissertation is dedicated to members of the Puerto Rican and undocumented community, whose brilliance is often undervalued. As a professor, I will encourage more underrepresented students to pursue careers in science.

TABLE OF CONTENTS

LIST OF FIGURES

LIST OF TABLES

ACKNOWLEDGEMENTS

First and foremost, I would like to thank my advisors, Sarah and Geno; they have really shaped the scientist I've become. Thank you for your countless support, for believing in me when I did not, for encouraging me to share my ideas, for teaching me to question everything, for highlighting my work to others, and for giving me the opportunity to become a leader. I would not have reached this point without you.

I would also like to thank the members of my committee, who have kindly made themselves available to discuss my work and help me grow as a scientist. Thank you, Peter, for teaching me what I currently know about biology and always being happy to advise me on my professional development. Thank you, Julie, for enriching my research with your model and ideas. Thank you, Rob, for teaching me much of what I know about data analysis and seeding the initial questions for two of my chapters. Thank you, Jan, for your support; though our interactions were limited, I became very close with some members of your lab who have been priceless to me.

I extend my gratitude to the co-authors and mentors that have helped me along the way, including Audric Collignon, Mark Merrifield (UCSD), Yi-Leng Chen (UH-Honolulu), He Wang (UCSD), Craig Lee (APL-UW), Luc Rainville (APL-UW), Jeff Koseff (Stanford University), Stephen Monismith (Stanford University), and Ken Brink (WHOI). My research would not have been possible without your data, instruments, scientific insights, and advice. I am also grateful for my funding sources: the Office of Naval Research, and the Ford Foundation for the grants and fellowships that have enabled my studies.

Much of my work took place in the Seychelles. As such, I would like to thank the Seychellois community that supported my research there, as well as the invaluable friends who helped me during the long laborious days of field work. Thank you to the Seychelles Fishing Authority, Seychelles Meteorological Authority, and the Better Life Foundation for sharing your data and exchanging ideas with us during our multiple meetings. Thank you to Ralph, Eric, and Dominique for your patience and boating expertise. I also want to give a huge and immense thank

you to Rich Walsh, Hugo Sánchez-Ulloa, Rob Grenzeback, Lillian McCormick, André Amador, Madeleine Harvey, Beverly French, Alfredo Girón, Katelin Pedersen, and Mohammad Sederat for venturing to the field with me and enduring many long, hard days of work. Multiple strong friendships emerged from this bonding time, and I am eternally grateful for all of you.

Thank you to my lab mates, past and present, for all the conversations we've shared (goofy and intellectual): Angelica Rodriguez, Madeleine Harvey, Lauren Kim, Duncan Wheeler, Alma Castillo-Trujillo, Jacqueline McSweeney, Xiaodong Wu, André Amador, Hugo Sánchez-Ulloa, and Annie Adelson. Thank you, also, to my original PO cohort for all your help throughout the years: Bia Villas-Boas, Derek Grimes, Olavo Badaró Marques, Stephen Holleman, Effie Fine, and Paul Chamberlain.

This dissertation would not have been possible without the unwavering support of all my friends. Thank you to my MAE crew: Mónica Zamora Zapata, Elynn Wu, José Ortíz Tarín, and Ingram Vargas for all our weekend dinners, outdoor trips, and philosophical conversations. Thank you also to Kristen Brañez, Tyler Gay, Mika Siegelman, Jess Garwood, Sabrina de Vera, Jonathan Navarrete, and Charlotte Rivera for the integral role you've played in my life. Thank you to my communities for enriching my life beyond the academic. Thank you, again, to Rich Walsh for coming to my rescue every day and a special thank you to my partner, Kaily Heitz, for her amazing support during these stressful pandemic dissertation times.

Last but not least, thank you to my family for staying by my side for the last (almost) 30 years. Thank you to my parents (Esther Soltero and George Arzeno); they are firm believers in the power of education, and I have obtained much of my drive to become a professor from them. Thank you also to my siblings (Claudia, Natalia, Paola, and George), my siblings' partners (Patrick, Gabriel, Michael, and Tiffany), and my wonderful nieces (Daniela, Adriana, and Mariana) for inspiring me, checking-in on me, making me laugh, and comforting me throughout this process. Thank you all for being sources of joy when times get tough. You are all always on my mind.

It really does take a village, and I'm grateful for everyone that has played a part in this journey.

Chapter 1, in full, is a reprint of the paper "An Alongshore Momentum Budget Over a Fringing Tropical Fore-Reef" published in Journal of Geophysical Research: Oceans by I. B. Arzeno, S. N. Giddings, G. Pawlak, and M. Merrifield in 2018. The dissertation author was the primary investigator and author of this paper.

Chapter 2, in full, has been submitted for publication of the material as it may appear in Geophysical Research Letters (2020), by I. B. Arzeno, S. N. Giddings, G. Pawlak, and R. Pinkel. The dissertation author was the primary investigator and author of this paper.

Chapter 3, in full, is currently being prepared for submission for publication of the material to Journal of Geophysical Research: Oceans by I. B. Arzeno, S. N. Giddings, G. Pawlak, J. L. McClean, and H. Wang. The dissertation author was the primary investigator and author of this paper.

VITA

2012	B. S. in Earth Systems, with Honors, Stanford University
2013	M. S. in Civil and Environmental Engineering, with specialization in Environmental Fluid Mechanics and Hydrology, Stanford University
2020	Ph. D. in Oceanography, University of California, San Diego

PUBLICATIONS

Arzeno, I. B., Giddings, S. N., Pawlak, G., McClean, J. L. & Wang, H. "Generation of low-latitude seamount-trapped waves: a case study of the Seychelles Plateau", in prep. for *Journal of Geophysical Research: Oceans*.

Arzeno, I. B., Giddings, S. N., Pawlak, G. & Pinkel, R. "Generation of Quasi-Biweekly Yanai Waves in the Equatorial Indian Ocean", under review for *Geophysical Research Letters*.

Arzeno, I. B., Collignon, A., Merrifield, M., Giddings, S. N., & Pawlak, G. (2018). "An Alongshore Momentum Budget over a Fringing Tropical Fore-Reef", *Journal of Geophysical Research: Oceans*, 123(11), 7839-7855, doi: 10.1029/2018JC014238.

Arzeno, I. B., Beardsley, R. C., Limeburner, R., Owens, B., Padman, L., Springer, S. R., Stewart, C. L. & Williams, M. J. (2014). "Ocean variability contributing to basal melt rate near the ice front of Ross Ice Shelf, Antarctica", *Journal of Geophysical Research: Oceans*, 119(7), 4214-4233, doi:10.1002/2014JC009792.

Amador A., **Arzeno, I. B.**, Giddings, S. N., Merrifield, M. A., & Pawlak, G, "Cross-Shore Structure of Tidally-Driven Alongshore Flow over Rough Bathymetry", under review for *Journal of Geophysical Research: Oceans*.

Castillo-Trujillo, A. C., Giddings, S. N., Pawlak, G, **Arzeno, I. B.**, McClean, J. L. & Rainville, L. "Circulation around and atop the Seychelles Plateau", in prep. for *Journal of Geophysical Research: Oceans*.

ABSTRACT OF THE DISSERTATION

Interactions between Large-Scale Oscillatory Flows and Bathymetry

by

Isabella Beatriz Arzeno

Doctor of Philosophy in Oceanography

University of California San Diego, 2020

Sarah N. Giddings, Co-Chair
Geno R. Pawlak, Co-Chair

The topography of an environment is critical for influencing the hydrodynamics of a region and allowing diverse ecosystems to exist in areas with, otherwise, low productivity. We investigate the flow response associated with interactions of large-scale waves with bathymetry of two distinct spatial scales: coral reefs (O(1 km)) and seamounts (O(100 km)).

Momentum balances over coral reefs have mostly been estimated for cross-reef flow in wavy environments. In contrast, we examine the effect of coral reef roughness on alongshore tidal momentum; this is accomplished using month-long pressure, temperature, and velocity observations gathered over a 2-km stretch of a Hawaiian fringing reef system. We find that

temporal acceleration plays an important role in the momentum balance. The two dominant forces affecting the alongshore depth-averaged flow acceleration are the tidal pressure gradient and the drag exerted by the coral reef bottom. We estimate drag coefficients and discuss the importance of coral reef drag throughout a tidal cycle.

The interaction between flow and bathymetry on a larger scale is studied using, primarily, satellite data and numerical model output in tropical regions of the Indian Ocean. Satellite observations are employed to characterize the generation of quasi-biweekly Yanai waves, oscillations with a wavelength estimated around 4,000 km, roughly 63% of the width of the equatorial Indian Ocean. These observations provide the first full picture of a quasi-biweekly Yanai wave in the Indian Ocean. Careful analysis suggests that these waves are generated in the western region of the basin, near the Seychelles Plateau, a relatively shallow (60-100m), large ($\sim$200 km), steep submarine platform. We examine the connection between Yanai waves and the Seychelles Plateau using model output from the global Los Alamos Parallel Ocean Program Model 2 (POP2), a theoretical stratified seamount-trapped wave model, and limited mooring data. POP2 output suggests that Yanai wave energy enters the Plateau system near the surface, at the western edge, inducing a resonant trapped wave response. The trapped wave redistributes equatorial energy to smaller scales, vertically in the water column, and anticyclonically along the Plateau circumference.

Introduction

Bathymetry plays an important role in modifying flow, allowing diverse ecosystems to exist in barren regions of the ocean (e.g. Gove et al., 2016; Morato et al., 2010). Further understanding of bathymetry effects on the surrounding flow is necessary to improve modeling efforts, quantify energy pathways, and restructure ecosystem management policies. In this dissertation, we examine the interaction of basin-scale waves in tropical regions with nearby bathymetry, specifically focusing on changes in momentum and energy that emerge from the interaction of tides and Yanai waves with coral reefs and seamounts, respectively.

Tides are the most ubiquitous large-scale oscillatory flows. Tidal currents, such as those generated by the M_2 semidiurnal tidal constituent, play a role in tropical coral reef ecosystems by influencing larval dispersal and reef connectivity (Cowen et al., 2000; Gilg and Hilbish, 2003; Williams et al., 1984). Thus, knowledge of the flow structure is critical for improving ecosystem models. Although cross-shore hydrodynamic processes over coral reefs have been studied extensively (e.g. Hench et al., 2008; Lentz et al., 2018; Lowe et al., 2009b), the alongshore direction, where we expect tidal currents to be the strongest, has been understudied. In chapter 1, we explore the dominant momentum balance over 2 km of a tropical fringing reef in Hawai'i, using data from a mooring array on the 12 m isobath. This work has motivated a follow-up observational and theoretical study on the cross-shore variations of the momentum balance and drag coefficient (Amador et al., in review).

Yanai waves (also known as mixed Rossby-gravity waves) are lesser known, large-scale

equatorially-trapped flows characterized by a dispersion relation with characteristics akin to Rossby waves and inertio-gravity waves at low and high frequencies, respectively. Yanai waves are of interest because they drive upwelling (Horii et al., 2011; Tsai et al., 1992) and have been associated with enhanced primary productivity (Uz et al., 2001). Moreover, they can interact with the various islands and seamounts near the equatorial waveguide. However, research on Yanai waves in the equatorial Indian Ocean has been limited to theory, numerical models and current velocity data from spatially sparse moorings (e.g. Chatterjee et al., 2013; Masumoto et al., 2008; Miyama et al., 2006). Chapter 2 explores the generation and characteristics of quasi-biweekly Yanai waves in the tropical Indian Ocean using satellite data, providing the first comprehensive picture of the wave in the Indian Ocean, and enabling us to further look at the potential energy flux between this equatorial wave and one of the many seamounts in its path, the Seychelles Plateau.

The Seychelles Plateau is a large elliptical submarine platform in the southwestern equatorial Indian Ocean. It is an area of interest given its steep slopes of O(0.05), shallow average depth (60–100 m), large size ($\sim$ 200 km x $\sim$ 300 km), and location near the primary Yanai wave generation site identified in Arzeno et al. (in review, see chapter 2). Chapter 3 is a case study examining the forcing of seamount-trapped waves around the Seychelles Plateau by equatorial Yanai waves, as part of the larger North Arabian Sea Circulation autonomous research (NASCar) project (Centurioni et al., 2017) funded by the Office of Naval Research (ONR). Many of the existing observational, analytic, and numerical studies that discuss trapped waves address tidally-generated waves in mid and high-latitude environments (e.g. Brink, 1995; Chapman, 1989; Codiga and Eriksen, 1997; Haidvogel et al., 1993; Hunkins, 1986). Exploring the role of seamount-trapped waves in the energy pathway in the tropics is particularly relevant considering that equatorial regions are noted to have low dissipation and diapycnal diffusivity rates (Gregg et al., 2003; Kunze et al., 2006).

Although we address two different scales (O(1 km) and O(100 km)) and topics (momentum

versus energy) in this dissertation, the fundamental question is similar: How does the topography influence large-scale periodic flows? This dissertation contributes to the existing literature and encourages further research on such processes in tropical regions.

Chapter 1

An Alongshore Momentum Budget over a Fringing Tropical Fore-Reef

Abstract

Existing momentum budgets over coral reefs have predominantly focused on cross-reef dynamics, lacking analysis of alongshore processes. To complement existing cross-reef research and enhance our understanding of forcing variability at the semidiurnal period, this study examines the σ–coordinate, depth-averaged alongshore momentum budget over a fore-reef as a function of tidal phase. The observations were gathered over a three-week timespan, between the 12 m and 20 m isobaths of a Hawaiian fringing reef system, focusing on two moorings on the 12 m isobath, where median drag coefficients estimated from log fits are $C_D = 0.0080$ $[-0.002, +0.004]$ and $C_D = 0.0023$ $[-0.0006, +0.0009]$. Analysis at one location shows that the unsteadiness, barotropic pressure gradient, and bottom drag are equally important; and their combination is sufficient to close the momentum budget. However, bottom drag is less important at the second mooring; the difference between unsteadiness and pressure gradient suggests that advective acceleration plays a significant role.

Plain Language Summary

Coral reefs are important, productive ocean ecosystems that are highly influenced by hydrodynamic forcing. Although a lot of research has been done to understand what forces drive the flow across tropical reefs (from offshore to onshore), less is known about the forces that drive flow parallel to the shoreline (alongshore). Here we study the physical dynamics over a coral reef in Hawai'i and determine that two primary forces drive the alongshore flow acceleration. One of the dominant forces is the drag exerted by the bottom reef, since coral are rougher than typical sandy coastal beds. The other dominant force is the pressure gradient, associated with the difference in sea level set up by the tide. The tidal cycle and the resulting flow response has important implications for the reef environment, with relevance for reef biology and, eventually, for ecosystem management policies.

1.1 Introduction

Over the years, the study of physical processes on coral reefs has covered a wide range of relevant scales (Lowe and Falter, 2015; Monismith, 2007). Reef scale hydrodynamics are important for several biological processes including larval dispersal and reef connectivity (Black, 1993; Cowen et al., 2000; Gilg and Hilbish, 2003; Kitheka, 1997; Williams et al., 1984; Wolanski and Kingsford, 2014); they also determine sediment transport and turbidity levels on the reef environment (Douillet et al., 2001; Rogers, 1990). Additionally, reef hydrodynamics have implications on ecosystem management policies (Green et al., 2015). However, to date, the primary focus of reef-scale processes on coral reefs has been on cross-reef dynamics in either non-tidally driven environments or on non-tidal timescales.

Significant work has been accomplished, for example, on understanding the cross-shore momentum budget over reefs, particularly wave-driven reefs. The cross-shore momentum budget over a coral reef can often be reduced to a balance that includes the pressure gradient, bottom

drag, and/or radiation stress gradients—depending on the reef section under study—while the wind is less influential or negligible (Coronado et al., 2007; Hench et al., 2008; Lentz et al., 2018; Lowe et al., 2009b, 2010; Monismith, 2014; Taebi et al., 2011). Studies that particularly focus on cross-reef wave-driven flow have shown that waves may impact circulation patterns and residence times in these systems (Coronado et al., 2007; Lowe et al., 2009a), as well as play an important role in enhancing the effects of bottom friction (Grant and Madsen, 1979, 1986) by promoting near-bed momentum transfer and thus intensifying the apparent roughness. A recent study by Lentz et al. (2018) explores how to properly account for the influence of waves on estimates of bottom drag to improve closure of the cross-reef momentum budget.

Alongshore momentum balances over coral reefs have not been extensively analyzed in the literature. Lentz et al. (2016) study a shallow reef in the Red Sea ($1-2$ m deep) and assume an alongshore balance between wind stress and bottom stress; however, they find this simplified balance to be lacking some important dynamics. Rogers et al. (2018) briefly looks at the alongshore momentum budget over a shallow pool ($1-3$ m deep) in Ofu, American Samoa, and determine the main balance to be between the pressure gradient and the bottom drag. Monismith (2014) discusses an alongshore momentum balance over a lagoon by using a simple model and assuming a pressure-friction balance. On the other hand, more extensive research on alongshore momentum budgets over sandy environments does exist, albeit looking at subtidal flows. Fewings and Lentz (2010) and Lentz et al. (1999) suggest that subtidal fluctuations over the inner shelf (approximately $10-15$ m deep) are dominated in the alongshore direction by the pressure gradient, wind stress, and bottom stress; nonlinear terms are assumed to be insignificant. Given that estimated values of C_D over coral reefs are typically higher than over sandy substrate—a compilation of C_D from various studies, adjusted to the common definition in Rosman and Hench (2011), show $C_D = 0.01-0.12$ over coral reefs—, we expect to find that bottom stress is a dominant term in the alongshore momentum budget over coral reefs, in agreement with previous work.

In this study, we estimate the different terms in the depth-averaged tidal alongshore momentum budget using data from moored instruments on a coral reef off the west coast of Oahu, Hawai'i (Figure 1.1) at a time when gravity waves are relatively small and wind is weak. Here, we (1) quantify terms in the momentum budget, highlighting the four dominant forces and (2) outline how the dynamics change throughout a tidal cycle. Specifically, in Section 2, we discuss the observational methods. In Section 3, we present the governing equations. In Section 4, we outline basic results from our momentum budget estimates and relate them to the tidal phase. Section 5 compares our results with previous studies and discusses the implications. Section 6 summarizes the main results. The appendix includes details on uncertainty calculations and the log fit method used to find the drag coefficient.

1.2 Methods

Data were collected during September 2013 using an array of moored instruments situated offshore of the west coast of Oahu, Hawai'i (Arzeno et al., 2018). Specific instrument locations are shown in Figure 1.1. The bathymetry inshore of the 20 m isobath is generally homogeneous on the large-scale but subject to small-scale roughness variability (Figure 1.2). The root mean squared (RMS) roughness measured by the REMUS autonomous underwater vehicle over a 50 m^2 box—RMS calculations explained in Nunes and Pawlak (2008)— is O(10^{-3} m), higher than sandy substrates but lower than the bottom roughness typical of coral reefs (Jaramillo and Pawlak, 2011; Lentz et al., 2016; Nunes and Pawlak, 2008). The seafloor slope in the cross-shore direction is $O(10^{-2})$.

The mooring array consisted of two bottom-mounted RD Instruments Acoustic Doppler Current Profilers (ADCPs) located 257 m apart at mean depths of 13.6 m and 11.9 m, as well as a third ADCP located 274 m offshore of the other two instruments, at a mean depth of 21.8 m. From here on, we will refer to these as the 12mN, 12mS, and 20m ADCPs, based on their

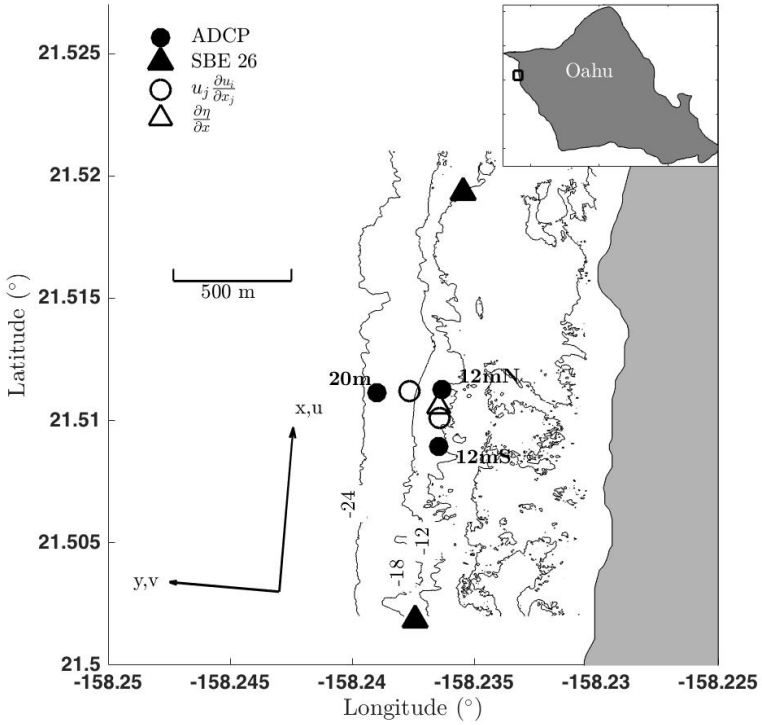

Figure 1.1: Location of instrument array and estimated momentum budget terms. The inset shows the general study site location on Oahu, Hawai'i. The map bathymetry is taken from SHOALS lidar, with contours depicting the 6, 12, 18, and 24 m depths. ADCP and pressure sensor locations are shown in shaded black dots and triangles, respectively. The approximate location of the advective acceleration estimates are shown as open circles, while that of the barotropic pressure gradient is shown as an open triangle. The along-coast and across-coast coordinate system used in this study is depicted, consistent with the bathymetry.

locations in Figure 1.1. The 12 m and 20 m ADCPs resolved velocity profiles at vertical intervals of 0.25 m and 1.25 m, respectively. All ADCPs were sampling in Mode 12 (fast ping mode) at 0.5 Hz. Thermistor chains were deployed near the 20 m and 12mN ADCPs. An Acoustic Doppler Velocimeter (ADV) was deployed next to the 12mS ADCP (as seen in Figure 1.2). The ADV sampled at 16 Hz for 12 minutes every hour. Additionally, two pressure sensors were placed at the northern and southern edges of our sampling site, about 2km apart in the alongshore direction ($\sim 5^\circ$ from true North), at average depths of 12.2 m and 13.6 m, respectively. The wind velocity was not recorded at this site (nor nearby) during the experiment; instead, results from model runs produced at the University of Hawai'i (Y. Chen) with 1.5 km resolution were used.

These runs employ the Advanced Research Weather Research and Forecasting (WRF) dynamical solver developed and maintained by the Mesoscale and Microscale Meteorology Division of the National Center for Atmospheric Research. WRF model output has shown good agreement with QuikSCAT measurements, buoy observations, and satellite data (Hitzl et al., 2014; Li and Chen, 2017); however, local winds could be modified by nearby steep mountain topography. For this analysis, we use the hourly wind speed averaged over the nearest two grid points.

Figure 1.2: Photo of typical roughness at study site.

All time series, except for the ADV data, were averaged in 20-minute blocks of time with a 50% overlap. After averaging, the ADCP measurements from the top 15% of the water column were removed, and the velocities were extrapolated assuming no stress at the surface (i.e. no wind), replacing the near-surface data with a constant value equal to the uppermost available velocity. Velocities below the first bin ($\sim$ 1.0 mab) were estimated by extrapolating measurements to the seafloor, assuming a logarithmic profile, applying a no-slip boundary condition. All velocity measurements were interpolated to fall in the same depth bins as those in the northernmost ADCP (12mN). The principal axes for the 12mN, 12mS, and 20m ADCPs are 4.22°, 6.34°, and 1.38° from true North, respectively. The principal axes are not notably different (i.e. vary by less than a degree) if northward and southward velocities are considered separately. However, all velocities were rotated to 5.28°, from true North, roughly parallel to the coastline, in order to facilitate the calculation of gradient terms in the momentum budget. The alongshore and cross-shore directions are denoted by u and v, respectively.

1.3 Alongshore Momentum Budget

The alongshore momentum budget can be expressed by either a flux-conserving or non-flux-conserving form of the equation. When calculating spatial gradients, the flux-conserving form of the depth-averaged momentum budget (e.g. Lentz et al., 1999) avoids complications due to variations in the bathymetry by taking the spatial derivative of an already depth-integrated velocity product:

$$\frac{1}{D}\frac{\partial}{\partial x_j}\int_{-h}^{\eta} u_i u_j dx_3, \tag{1.1}$$

where $i, j = 1, 2$, $D = h + \eta$, h is the mean water depth, η represents the anomalies about h, and u is the depth-dependent velocity. This is in contrast to the non-flux conserving, depth-averaged form of the momentum equation, where the advective acceleration includes the vertical integral of a term with a spatial derivative:

$$\frac{1}{D}\int_{-h}^{\eta} u_j \frac{\partial u_i}{\partial x_j} dx_3, \tag{1.2}$$

and changes in bathymetry become a difficulty. These two forms are interchangeable only when the discretized gradients are centered on the same location, so that continuity is readily satisfied. Given our instrument positions, this assumption does not hold in this study because our cross-shore and alongshore gradients are offset (Figure 1.1). Since horizontal continuity, in its discretized form, is not zero for this study, i.e.,

$$u\frac{\partial u}{\partial x} + u\frac{\partial v}{\partial y} \neq 0, \tag{1.3}$$

and since we cannot calculate $u\frac{\partial w}{\partial z}$, the advective acceleration terms estimated in flux-conserving form (definition 1.1) yield values that are almost twice as large as the advective acceleration in the non flux-conserving form (definition 1.2).

Thus, in order to minimize uncertainty in the advective acceleration, we choose to analyze the momentum budget using the non-flux conserving form of the equation in depth-normalized coordinates, to accommodate any general bathymetric changes between instruments that may affect gradient calculations—such as the depth difference between the 12mN and 12mS moorings—when estimating the alongshore advective acceleration. Following Giddings et al. (2014), the depth-averaged, depth-normalized momentum equation, assuming hydrostatic conditions and $\eta \ll D$, can be described by

$$\underbrace{\frac{\partial U_i}{\partial t}}_{1} + \underbrace{\int_0^1 u_j \frac{\partial u_i}{\partial x_j} d\sigma}_{2} - \frac{\sigma}{D}\left(\int_0^1 \frac{\partial u_i}{\partial \sigma}\left(u_j \frac{\partial D}{\partial x_j} + \frac{\partial D}{\partial t}\right) d\sigma\right) + \int_0^1 \frac{w}{D}\frac{\partial u_i}{\partial \sigma} d\sigma + \frac{1}{D}\int_0^1 \frac{\left\langle \partial u_i' u_j' \right\rangle}{\partial x_j} d\sigma$$

$$+2\varepsilon_{ijk}\Omega_j U_k = \underbrace{-g\frac{\partial \eta}{\partial x_i}}_{3} - \frac{gD}{\rho_0}\frac{\partial}{\partial x_i}\int_0^1 \int_\sigma^1 \rho d\sigma d\sigma + \frac{g}{\rho_0}\frac{\partial D}{\partial x_i}\int_0^1 \int_\sigma^1 \sigma \frac{\partial \rho}{\partial \sigma} d\sigma d\sigma - \underbrace{\frac{1}{D\rho_0}(\tau_b - \tau_s)}_{4}, \quad (1.4)$$

where $i, j = 1, 2$, $\sigma = \frac{z}{D}$ (with $D = h + \eta$, where h is the mean water depth and η represents the anomalies about h), u_i is the depth-dependent velocity, $U_i = \int_0^1 u_i d\sigma$, and τ_s and τ_b are the surface and bottom stresses, respectively. All variables are 20-minute averages, except for u_i', the deviations from the average (both wave and turbulence-induced fluctuations). Brackets $\langle\rangle$ denote the time average of the nonlinear deviation terms. The unsteadiness, advective acceleration, barotropic pressure gradient, and bottom stress are highlighted, in order, by the numbers 1-4.

The σ-coordinate advective acceleration was discretized as

$$u_j \frac{\partial u_i}{\partial x_j} = \overline{u_j} \frac{\Delta u_i}{\Delta x_j}, \quad (1.5)$$

where $\overline{u_j}$ is the spatial average of the velocities. The sea surface displacement η is the deviation from the time mean pressure at each location, and the barotropic pressure gradient was calculated as the difference in sea surface displacement between the locations of our pressure gauges, assuming that there are no steady gradients on the timescale of the deployment. Thus, the discretized terms are not exactly at the same location (see Figure 1.1), but they are all within 150 m of the 12mN ADCP. The wind stress τ_s was parameterized using a typical quadratic drag law

$$\tau_s = \rho_a C_D U_i^w \sqrt{U_j^w U_j^w}, \tag{1.6}$$

where $i = 1,2$, $\rho_a = 1.2$ kg m^{-3} is air density, U_i^w is wind velocity, and C_D for the wind stress is taken to be $C_D = 1.1$ x 10^{-3}, according to Smith (1988). The bottom stress τ_b was estimated following

$$u_* = \sqrt{\frac{\tau_b}{\rho}}, \tag{1.7}$$

where u_* is the shear velocity in the alongshore direction. The shear velocity was found by fitting the boundary layer velocity to a log-law and defect-law profile.

If the velocity observations follow a log-law and defect-law profile, given a steady, fully developed flow, our mean vertical velocity profile can be described as

$$\langle u \rangle = \frac{u_*}{\kappa} \left\{ \ln\left(\frac{z - z_{\text{ref}}}{z_0}\right) + 2\Pi \sin^2\left[\frac{\pi(z - z_{\text{ref}})}{2\delta}\right] \right\}, \tag{1.8}$$

where $\kappa = 0.41$ is the Von Kármán constant, z_{ref} is a reference height for the velocity profile, z_0 is a roughness length scale, $\Pi = 0.2$ is Coles' wake strength parameter for high Reynolds number

flows (Coles, 1956; Nezu and Rodi, 1986), and δ is the boundary layer height, taken to be the last bin in the log fit, following Rosman and Hench (2011). (Details on the log fit method are described in Appendix A.) In addition, drag estimates from log fits were compared to those from independent calculations (not shown here) using cospectral fits from ADV and ADCP data (Gerbi et al., 2008; Kirincich et al., 2010; Kirincich and Rosman, 2011). The drag coefficients estimated using these three methods fall within error bars of each other.

The drag coefficient is defined from the values of shear velocity, following Lentz et al. (2018), as

$$C_D = \left(\frac{u_*}{\left\langle \int_0^1 u_i d\sigma \int_0^1 \sqrt{\overline{u_j u_j}} d\sigma \right\rangle} \right)^2, \tag{1.9}$$

where $i = 1,2$, u_i is the full (not time-averaged) velocity, and the brackets $\langle\rangle$ denote the 20-minute time-averaging. Although Lentz et al. (2017) and McDonald et al. (2006) note that the depth-averaged drag coefficient (C_D) generally depends on the ratio of total water depth (D) to roughness length scale (z_0), they also observe that, excluding waves, $C_D \to 0.01$ as the ratio of D to z_0 increases. In particular, Lentz et al. (2017) indicate that C_D asymptotes for $\frac{D}{z_0} > 100$, which we will argue in Section 5 to be the general case for our study site.

1.4 Overview of Results

General observations show that the semidiurnal tidal signal dominates the pressure fluctuations (Figure 1.3a), with a pronounced diurnal inequality and fortnightly cycle. The tidal range reached a maximum of ~ 0.55 m during our sampling period. Output from the WRF model runs shows that the wind was predominantly in the southwest direction during the observational period (Figure 1.3b) at an absolute speed less than 12 m s^{-1}. Significant wave heights (H_s) calculated using spectral analysis and linear wave theory were, on average, H_s=0.40 m and H_s=0.50 m at the

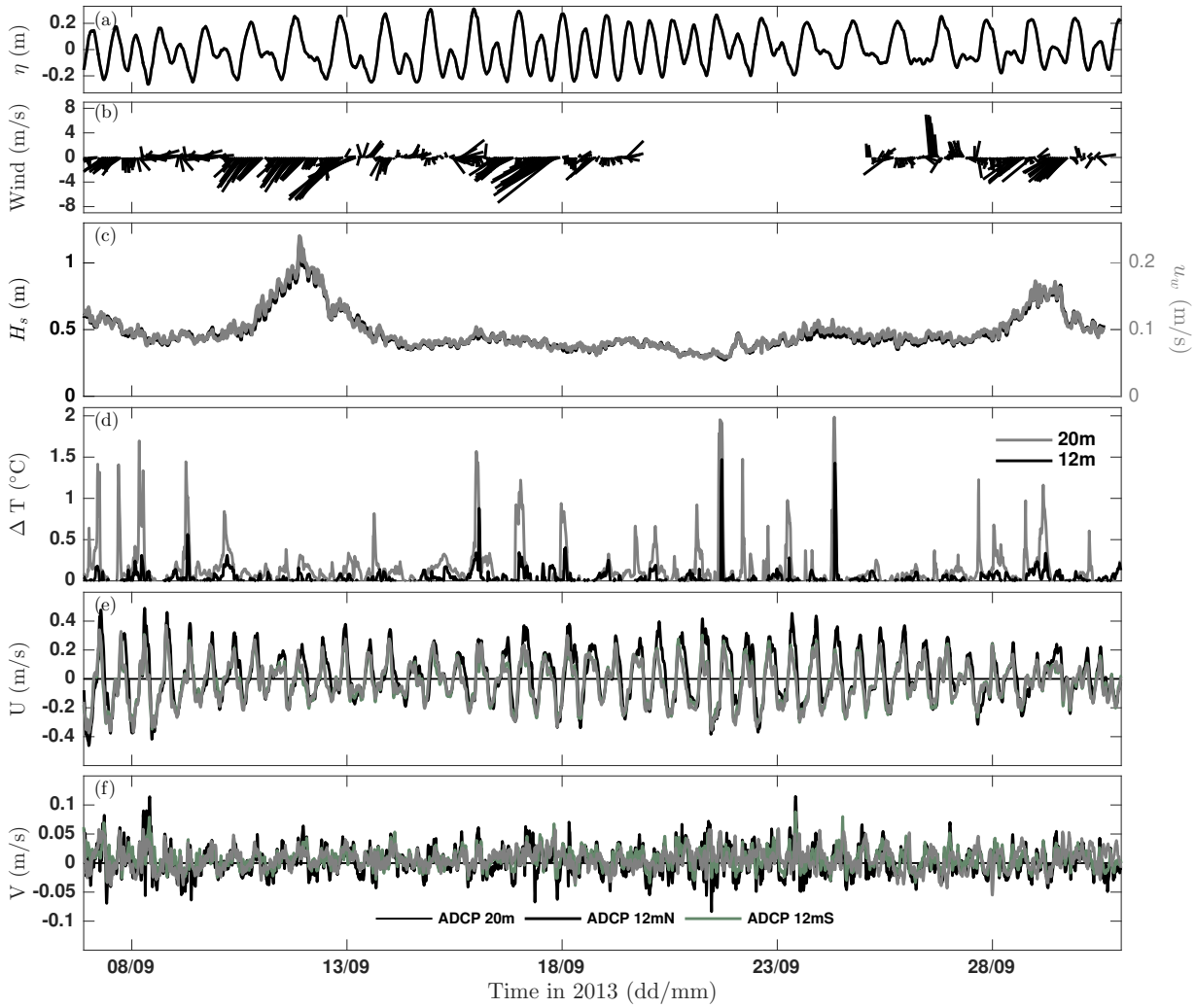

Figure 1.3: (a) Timeseries of sea surface displacement at the 12m N pressure sensor, (b) model output wind velocity near the study site, (c) wave height and bottom wave orbital velocity from spectral analysis and linear theory, (d) difference in temperature between top and bottom thermistors at the 12mN and 20m mooring sites, (e) alongshore and (f) cross-shore depth-averaged velocities (each defined in section 2).

northern and southern pressure sensor locations, respectively, with a maximum of $\sim$ 1.2 m during a period of swell (Figure 1.3c). (There were not enough effective degrees of freedom to properly calculate 95% confidence intervals for the mean H_s.) The near-bottom wave orbital velocities (Figure 1.3c) are the same order of magnitude as the alongshore depth-averaged velocities (Figure 1.3e).

The temperature difference (ΔT) between the top and bottom sensors on the thermistor

chain (1.12 m below the surface and 0.30 m above the bottom) at the 12 m isobath was, on average, $\overline{\Delta T} = 0.34 \pm 0.0025^{\circ}$ C (Figure 1.3d). Salinity was only measured on the 12 m mooring, near the bottom, and varied little over the observational period (mean of 35.33 $\pm$ 0.006 psu). For calculations of the Brunt Väisälä frequency (N^2), we apply this bottom salinity time series over the entire water column, recognizing that it may result in an underestimate of the stratification. In general, our estimated Brunt Väisälä frequencies are low and only rise above the Coriolis frequency in 8.3% and 26.8% of the vertical profiles from the 12mN and 20m moorings, respectively. Intermittent sharp changes in temperature are seen near the bottom of the 20m thermistor chain and are likely associated with shoaling internal waves. Overall, we consider the system to be weakly stratified. Richardson numbers (calculated at every depth where stratification could be estimated) were below the critical value of $Ri = 0.25$ (throughout the entire water column) over 99% and 95% of the sampling time at the 12mN and 20m offshore moorings, respectively, indicating that our sampling location is mostly vertically well-mixed. When performing logarithmic fits to estimate drag coefficients, we exclude any observations where $Ri > 0.25$.

Alongshelf current variability is dominated across the water column by the semidiurnal tidal cycle (Fig. 1.3e), and depth-averaged currents are incoherent (not phase-locked) with the surface pressure at the semidiurnal frequency (Fig. 1.3a). This will be discussed further in Section 5. The depth-averaged M_2 tidal ellipses at the 12 m moorings account for over 60% of the total variance and are oriented in the alongshore direction. Standard deviations for the depth-averaged alongshore tidal velocities at the three moorings were $\sigma = 0.14 - 0.17$ m s^{-1} (Fig. 1.3e). Cross-shelf currents were significantly weaker than those in the alongshelf direction; their standard deviations were an order of magnitude smaller than those for the alongshore velocities. The largest standard deviation in the cross-shelf currents was $\sigma = 0.023$ m s^{-1}, at the 20m ADCP (Fig. 1.3f).

1.4.1 Drag estimates

Drag coefficients were estimated using the resulting u_* from the log fits, following equation 1.9. In general, we found better fits for the 12mN velocity profiles, with 72% of the fits having $R^2 \geq 0.95$, while only 53% of the fits had $R^2 \geq 0.95$ at 12mS. The median value for C_D at the 12mN mooring is $C_D = 0.0080$ $[-0.002, +0.004]$; at 12mS, $C_D = 0.0023$ $[-0.0006, +0.0009]$. (The confidence intervals were computed by bootstrapping, which sometimes result in asymmetric uncertainties.) As mentioned previously, drag coefficient values from the log fits at 12mS were confirmed with two additional estimates using cospectral fits applied to velocities from both the ADV (Gerbi et al., 2008) and the ADCP (Kirincich et al., 2010; Kirincich and Rosman, 2011).

In general, drag at this site is weaker than what has been previously reported for other tropical coral reefs (e.g. Rosman and Hench (2011)), likely because of the study region's relatively low roughness (refer to Figure 1.2). There are spatial differences within the study region: the median C_D and z_0 are statistically significantly lower at 12mS than at 12mN. The values are not heavily influenced by current directionality: estimating different C_D for positive and negative alongshore velocities results in median values with overlapping confidence intervals. There is a statistically significant difference in C_D values estimated for northward and southward velocities only at the 12mS mooring when we consider the largest 25% of the velocities ($\mid U \mid > 0.17$ m s^{-1}). The current directionality did affect the fit profiles; a larger percentage of log fits met our quality standards when the depth-averaged alongshore velocities were directed southward (77% at 12mN and 63% at 12mS) rather than northwards (66% at 12mN and 41% at 12mS).

The statistics of the various parameters in equation 1.8 are presented in Table 1.1 and Table 1.4 for the 12 m moorings. For the purposes of estimating a bottom stress to include in our momentum budget calculations, we choose to use the time-varying results of the log fits (not the statistical averages) for added accuracy, given that drag coefficient can be a function of the wave-current velocity ratio, although tidal phase-averages of C_D do not vary significantly over a tidal cycle. Further, we do not consider the 20 m ADCP in our analysis because only a small

Table 1.1: Median values of log fit parameters taken from entire time series

	12mN	**12mS**
% with $R^2 \geq 0.95$	72%	53%
u_*	0.015 ± 0.002	0.0095 ± 0.0013
z_0	0.11 ± 0.04	0.0032 ± 0.003
z_{ref}	0 [-0, +0.01]	0 [-0, + 0.003]
δ	3.47 ± 0	3.76 ± 0
C_D	0.0080 [-0.002, +0.004]	0.0023 [-0.0006, +0.0009]
C_D^+	0.0068 [-0.002, +0.004]	0.0017 [-0.0006, +0.0008]
C_D^-	0.0090 ± 0.003	0.0026 [-0.0007, +0.0009]

Note. The asymmetric confidence intervals result from using bootstrap methods.
$^+$ Drag coefficients calculated using positive alongshore, depth-averaged velocities.
$^-$ Drag coefficients calculated using negative alongshore, depth-averaged velocities.

fraction of the log profiles met our quality standard, likely because the 20 m ADCP sampling scheme averaged to a lower vertical resolution than that for the 12 m moorings.

1.4.2 Momentum Balance

The largest terms in the momentum budget at both 12 m moorings are the unsteadiness, barotropic pressure gradient, advective acceleration, and bottom stress (estimated using a time-varying drag coefficient), with magnitudes $O\left(10^{-5}\right)$. These components are numbered in equation 1.4, and their time variability is presented in Figure 1.4, with 95% uncertainty intervals calculated using error propagation, as explained in Appendix B. Specifically, the unsteadiness and barotropic pressure gradient terms dominate the momentum budget at both 12 m moorings (Fig. 1.4a,b). The bottom stress magnitude at 12mN is comparable to that of the unsteadiness and pressure gradient; however, bottom stress is significantly smaller at 12mS (Figure 1.4e). The advective acceleration could be an important contributor during certain tidal phases, particularly at 12mS, where the bottom drag is weak. The alongshore component of the advective acceleration is mostly negative, while the cross-shore component is positive (Figure 1.4 c,d), resulting in mean values $O(10^{-5})$

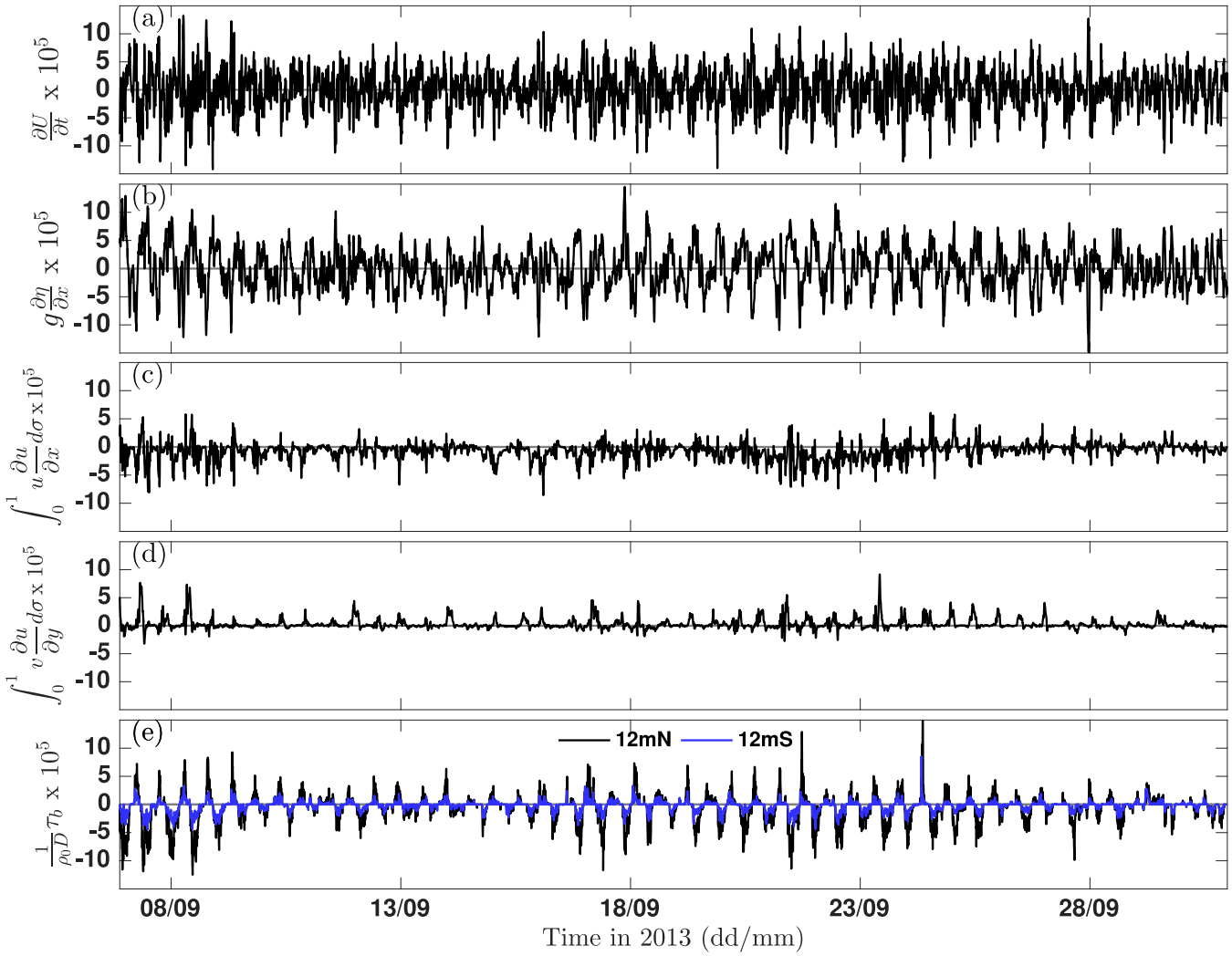

Figure 1.4: Dominant terms in the momentum budget, multiplied by a factor of 10^5. (a) Depth-averaged unsteadiness $\left(\frac{\partial U}{\partial t}\right)$ at 12mN; (b) Barotropic pressure gradient $\left(g\frac{\partial \eta}{\partial x}\right)$; (c) Depth-averaged alongshore advective acceleration $\left(\int_0^1 u\frac{\partial u}{\partial x}d\sigma\right)$; (d) Depth-averaged cross-shore advective acceleration $\left(\int_0^1 v\frac{\partial u}{\partial y}d\sigma\right)$; e) Bottom-drag $\left(\frac{1}{\rho_0 D}\tau_b\right)$ at 12mN and 12mS. The depth-averaged unsteadiness at 12mS has been omitted for graphic clarity, given its similarity to that at 12mN. The 95% confidence intervals are shaded in red, though their size (two to three orders of magnitude smaller than the terms) renders them difficult to observe.

(Table 1.2). This suggests that a net momentum flux is possible. However, the instrument array may not be dense enough to accurately capture the advective acceleration during the entire tidal cycle. These five terms fluctuate with a semidiurnal frequency, increasing and decreasing with a fortnightly cycle.

Table 1.2: Momentum budget terms statistics

Momentum budget term	12mN mean	12mN standard deviation	12mS mean	12mS standard deviation
$\frac{\partial U}{\partial t}$	1.06 x 10^{-7}	3.16 x 10^{-5}	8.69 x 10^{-8}	3.64 x 10^{-5}
$\int_0^1 v\frac{\partial u}{\partial y}$	2.79 x 10^{-6}	9.24 x 10^{-6}		
$\int_0^1 u\frac{\partial u}{\partial x}$	-1.17 x 10^{-5}	1.68 x 10^{-5}	-1.17 x 10^{-5}	1.68 x 10^{-5}
$-g\frac{\partial \eta}{\partial x}$		3.63 x 10^{-5}		3.63 x 10^{-5}
$\frac{1}{\rho_0 D}\tau_b$	-7.98 x 10^{-6}	2.75 x 10^{-5}	-4.75 x 10^{-6}	1.06 x 10^{-5}
$\frac{1}{\rho_0 D}\tau_s$	-4.40 x 10^{-7}	1.14 x 10^{-6}	-4.40 x 10^{-7}	1.14 x 10^{-6}
fV	4.23 x 10^{-7}	8.74 x 10^{-7}	3.25 x 10^{-7}	9.23 x 10^{-7}
$\frac{\sigma}{D}\left(\int_0^1 \frac{\partial u_i}{\partial \sigma}\left(u_j\frac{\partial D}{\partial x_j}+\frac{\partial D}{\partial t}\right)d\sigma\right)$	1.68 x 10^{-6}	2.34 x 10^{-6}	1.68 x 10^{-6}	2.34 x 10^{-6}

Note. A cross-shelf advective acceleration could not be calculated for the 12mS mooring.
Note. Per the definition of the sea surface displacement (Section 3), the mean barotropic pressure gradient is defined to be zero.

The wind stress, Coriolis force, and the remaining, resolvable non-linear terms are all, at least, an order of magnitude smaller than the numbered terms in equation 1.4. The nonlinear horizontal perturbation terms will be neglected because they do not vary on a tidal timescale, and their uncertainty is about the same magnitude as the terms themselves. The vertical acceleration term cannot be accurately quantified due to error in the vertical velocity measurement, but this term can be expected to be small, based on scaling considerations. Further, we cannot properly calculate the baroclinic terms because of the absence of a thermistor chain at the 12mS mooring. However, given that an instrument tower situated ~ 56 m south of the 12mN mooring, in the alongshore direction, carried three additional thermistors at 0.37 mab, 1.2 mab, and 2.4 mab, at least one of the baroclinic terms in equation 1.4 can be roughly estimated. Assuming that D remains the same between the 12mN thermistor chain and the instrument tower, and assuming that any density above 2.4 mab is constant at the instrument tower, thus resulting in an overestimate of horizontal density gradients,

$$\frac{gD}{\rho_0}\frac{\partial}{\partial x_i}\int_0^1\int_\sigma^1 \rho d\sigma \sim O\left(10^{-6}\right), \tag{1.10}$$

an order of magnitude smaller than the dominant terms. The statistics for the terms that could be fully quantified are displayed in Table 1.2.

The variability of the momentum budget terms (numbered in equation 1.4) is best examined as a function of tidal phase. We use the depth-averaged alongshore velocity to determine the M_2 phase, with the interval between velocity peaks defining one full tidal oscillation (Fig. 1.3e). The tidal phase is labeled as $\phi = \pi\frac{\Delta t}{T}$ for instances corresponding to a velocity accelerating in the southward direction and $\phi = \pi\frac{\Delta t}{T} + \pi$ for velocities accelerating in the northwards direction, where Δt is the time difference between the data and the previous maximum/minimum in the velocity, and T is the time elapsed between subsequent maxima and minima (i.e. the duration of one tidal oscillation). At every tidal oscillation, $\frac{|U|}{|U|_{\max}} > 0.25$, where $|U|$ is the velocity range and $|U|_{\max}$ is the maximum over the entire time series. In total, forty-two tidal cycles were observed.

Although the sea surface displacement (η) generally serves as a good marker of tidal phase in unstratified environments, in this case, η is incoherent with the momentum budget terms. For example, the pressure gradient and η show a coherence squared (Coh^2) of $\mathrm{Coh}^2 = 0.55$ at the semidiurnal frequency, while the pressure gradient and U are almost perfectly coherent ($\mathrm{Coh}^2 = 0.99$) at that same frequency. We argue here that the nearshore pressure gradient and the alongshore velocities are driven primarily by the internal tide, while the observed surface displacement is dominated by the barotropic tide. This will be revisited in Section 5, the discussion section.

As shown in Figure 1.5a, throughout a tidal oscillation, the pressure and the alongshore depth-averaged velocity are in quadrature; the maximum correlation ($r = 0.56$) between both occurs when the velocity leads the sea surface height signal by 3.5 hours, around a fourth of the M_2 tidal cycle. Further, we observe a large scatter in the displacement η, given its incoherence with the depth-averaged alongshore velocity U. The cross-shore velocity is weak and asymmetric throughout a tidal cycle, with smaller magnitudes during the latter half of the cycle.

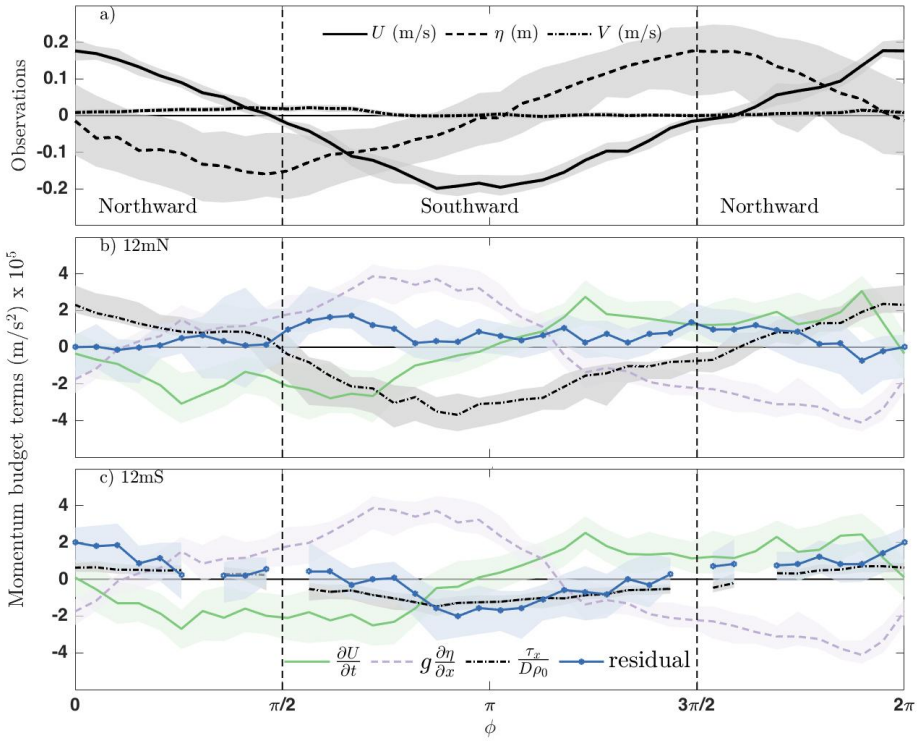

Figure 1.5: Tidal phase median values of (a) observed variables at 12mN, and estimated momentum budget terms at (b) 12mN and (c) 12mS, with shaded 95% confidence intervals from bootstrapping. Median values calculated from less than 25 valid estimates were not plotted. (The vertical black dashed lines indicate the transition between northwards and southwards mean flow.)

Following previous studies that neglect the advective acceleration due to instrument limitations or scaling arguments (Fewings and Lentz, 2010; Hickey, 1984; Lentz et al., 1999; Lentz and Raubenheimer, 1999), we first consider phase averages of the momentum budget unsteadiness, barotropic pressure gradient, and bottom drag (Figure 1.5b & c), having excluded the nonlinear inertial terms. Figure 1.5 also contains the phase-averaged residual momentum R necessary to close the budget, given as

$$\mathrm{R} = -\left(\frac{\partial U_i}{\partial t} + g\frac{\partial \eta}{\partial x_i} + \frac{\tau_b}{D\rho_0}\right). \tag{1.11}$$

Tidal phase averages of the momentum budget estimates show that unsteadiness and pressure

gradient are dominant terms at both 12 m moorings (Figure 1.5b & 1.5c). These are not in phase; the unsteadiness term is almost negligible when the pressure gradient is at its maximum. Bottom drag also plays a dominant role at 12mN, being of comparable magnitude as the unsteadiness and the pressure gradient, balancing the pressure gradient during almost half of the tidal cycle. The residual (R) at 12mN is near zero: the combination of the three dominant terms is sufficient to close the momentum budget, within uncertainty, during most of the tidal cycle (Figure 1.5b and Table 1.3). Although bottom drag at 12mS is weaker (Figure 1.5c), it offsets some of the barotropic pressure gradient when longshore velocities peak ($\phi \sim 0, \phi \sim \pi$). The magnitude of R at 12mS can surpass that of the bottom drag and even exceed that of the unsteadiness when $\phi \sim 0$ and $\phi \sim \pi$ (Figure 1.5c).

Comparing R at 12mS to our estimated advective acceleration from measurements (term 2 in equation 1.4):

$$\int_0^1 u_j \frac{\partial u_i}{\partial x_j} d\sigma \tag{1.12}$$

shows that the two agree within uncertainty when the depth-averaged alongshore velocity is southward ($\pi/2 < \phi < 3\pi/2$; Figure 1.6b). However, the observed advective acceleration fails to account for the residual when the currents are northward ($\phi \sim 3\pi/2$ to $\phi \sim \pi/2$; Figure 1.6b). Further, the smaller residual at 12mN (Figure 1.5b, Figure 1.6a) suggests that the advective acceleration as measured between the two sites is not representative at the northern site. This is all consistent with local acceleration of flow in the vicinity of the 12mS location for both northward and southward flow, as discussed at the end of this section. Alternatively, the residual in the 12mS momentum budget (Figure 1.5c, Figure 1.6b) may be a result of underestimated bottom drag from the log fits. Momentum budget closure can improve at 12mS by increasing the magnitude of the drag by a factor of 2 or 3, if advective acceleration is neglected. Nevertheless, we have likely not underestimated the bottom drag at 12mS, given that the same fitting methods and quality control

Table 1.3: Percentage of the tidal cycle when the momentum budget closes under different balances

Balance	Percent closure	
	12mN	12mS
$\frac{\partial U}{\partial t} = -g\frac{\partial \eta}{\partial x}$	27.5%	30.0%
$\int_0^1 u\frac{\partial u}{\partial x}d\sigma = -g\frac{\partial \eta}{\partial x}$	22.5%	22.5%
$g\frac{\partial \eta}{\partial x} = -\frac{1}{D\rho_0}\tau_b$	47.5%	27.3%
$\frac{\partial U}{\partial t} = -g\frac{\partial \eta}{\partial x} - \frac{1}{D\rho_0}\tau_b$	75.0%	60.6%
$\frac{\partial U}{\partial t} + \int_0^1 u\frac{\partial u}{\partial x}d\sigma = -g\frac{\partial \eta}{\partial x}$	25.0%	27.5%
$\frac{\partial U}{\partial t} + \int_0^1 v\frac{\partial u}{\partial y}d\sigma = -g\frac{\partial \eta}{\partial x}$	32.5%	
$\frac{\partial U}{\partial t} + \int_0^1 u\frac{\partial u}{\partial x}d\sigma = -g\frac{\partial \eta}{\partial x} - \frac{1}{D\rho_0}\tau_b$	25.0%	48.4 %
$\frac{\partial U}{\partial t} + \int_0^1 v\frac{\partial u}{\partial y}d\sigma = -g\frac{\partial \eta}{\partial x} - \frac{1}{D\rho_0}\tau_b$	77.5%	
$\frac{\partial U}{\partial t} + \int_0^1 u\frac{\partial u}{\partial x}d\sigma + \int_0^1 v\frac{\partial u}{\partial y}d\sigma = -g\frac{\partial \eta}{\partial x}$	37.5%	
$\frac{\partial U}{\partial t} + \int_0^1 u\frac{\partial u}{\partial x}d\sigma + \int_0^1 v\frac{\partial u}{\partial y}d\sigma = -g\frac{\partial \eta}{\partial x} - \frac{1}{D\rho_0}\tau_b$	45.0%	
$\frac{\partial U}{\partial t} = -\frac{1}{D\rho_0}\tau_b$	42.5%	51.5%
$\frac{\partial U}{\partial t} + \int_0^1 u\frac{\partial u}{\partial x}d\sigma = 0$	25.0%	32.5%
$\frac{\partial U}{\partial t} + \int_0^1 u\frac{\partial u}{\partial x}d\sigma = -\frac{1}{D\rho_0}\tau_b$	47.5%	45.5%

Note. A cross-shelf advective acceleration could not be calculated for the 12mS mooring.

were applied to the 12mN data and yielded the appropriate results to close the momentum budget at that location. Moreover, as mentioned in Section 4.1, the drag estimates at the 12mS mooring were confirmed with additional methods and data. In fact, if we retain the effects of advective acceleration at 12mS, an increase in bottom drag can only improve the momentum balance over part of the cycle, when alongshore velocity is southward, and leads to a larger net residual.

Finally, we can evaluate the role of the different terms in the momentum budget and their contribution to budget closure as a function of tidal phase. We evaluate model closure by estimating the phase averaged residual in the momentum budget, and quantifying the percentage of time that this residual differs from zero, within 95% confidence intervals, when we can consider the momentum budget as effectively closed. Statistics are summarized in Table 1.3.

A simple balance between the unsteady term and the barotropic pressure gradient,

$$\frac{\partial U_i}{\partial t} = -g\frac{\partial \eta}{\partial x_i}, \tag{1.13}$$

leads to phase-averaged momentum budget closure during 27%-30% of a tidal cycle at both 12 m moorings; this unsteady balance suggests that the frictional timescale for the alongshore flow

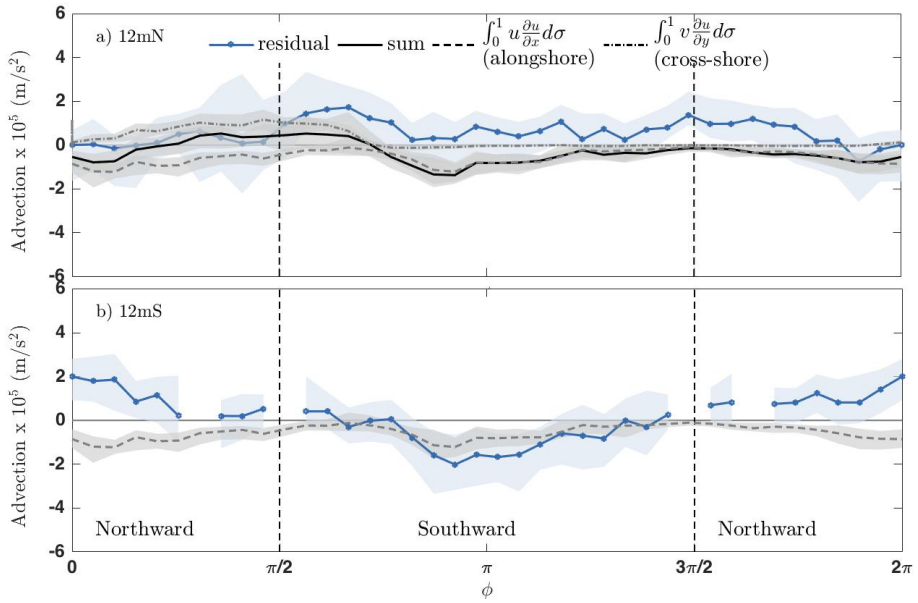

Figure 1.6: Tidal phase median values from the estimated total and individual components of the advective acceleration, as compared to the momentum budget residual, with shaded 95% confidence intervals from bootstrapping for (a) 12mN and (b) 12mS. Median values calculated from less than 25 valid estimates were not plotted. There is no estimate for the cross-shore advective acceleration at the 12mS site, so this term (and the sum of the terms) has been omitted from the lower plot.

on the inner shelf is comparable to the tidal timescale. Adding the bottom drag improves the closure of the budget dramatically (75% and 61% closure at 12mN and 12mS, respectively) since the term plays an important role in balancing the barotropic pressure gradient. The difference in percentage closure between mooring locations for this 3-term closure (including unsteadiness, barotropic pressure gradient, and bottom drag) is not statistically significant due to the small number of degrees of freedom (tidal phase bins). Note that including the cross-shore advective acceleration (Figure 1.6a) in the previous balance of unsteadiness, pressure gradient and bottom drag increases the percentage of closure at 12mN to 78% of the tidal cycle.

Although the alongshore advective acceleration does not improve the closure at 12mN, it is an important term at the 12mS mooring, as discussed above; in fact, the residual and the alongshore advective acceleration match, within uncertainties, when the velocities flow southward (Figure 1.6b). A budget at 12mS that includes the unsteadiness, bottom drag, alongshore advective acceleration, and barotropic pressure gradient closes 48% of the time. The percentage of net closure is limited because inclusion of the alongshore advective acceleration leads to excess momentum during northward flow. Table 1.3 shows the full balances and their percentage of closures throughout a tidal cycle.

The excess momentum noted above could be accounted for by a local acceleration at 12mS. For northward flow, a local acceleration at 12mS would require a positive gradient to the south of the site, with a negative gradient to the north, between 12mS and 12mN; for southward flow, the excess momentum at 12mS requires a negative velocity gradient between the two 12 m sites. The latter is consistent with the observations, resulting in advective acceleration estimates that do account for the residual in the 12mS momentum budget, while resolution of a gradient to the south of 12mS would require measurements at a third site. This emphasizes the importance of understanding the impacts of the discretization necessary for calculating momentum budgets in the field and the influence of spatial offsets when estimating different terms. This issue of fully estimating the advective acceleration also highlights an important limitation of this study;

a denser instrument array is needed to better constrain the advective acceleration terms in the momentum budget. Similar research with instrumentation that can capture dynamics that are important on length scales shorter than $x \sim 250$ m (the alongshore distance between the 12mN and 12mS moorings), such as local advective acceleration, would be be valuable to fully assess the importance of these terms.

1.5 Discussion

The tidal momentum balance, developed here for the fore-reef region, is important in establishing the dominant forcing terms on a semidiurnal timescale. Of particular note is the importance of the bottom drag and the advective acceleration. The alongshore momentum budget at both sites reflects a combination of the momentum balance for a shallow-water wave (unsteadiness $\sim$ pressure gradient) along with the pressure/drag balance that is more commonly associated with shallow tropical reef flats (Hench et al., 2008; Lowe et al., 2009b, 2010; Monismith, 2014; Rogers et al., 2018). There is an additional, albeit small, influence of the cross-shore advective acceleration term. On the other hand, the alongshore tidal budget at 12mS suggests that advective acceleration is an equally important contributor to the momentum budget as the bottom drag, similar to what Rogers et al. (2015) found over a spur and groove formation on the fore-reef. We hypothesize that the imbalance at the 12mS mooring is associated with a local acceleration of the flow. A close examination of the bathymetry, along with in-situ diver observations, indicates that there is a large ($\sim$3 m) step 20-30 m to the south of the mooring site, that may play a role in this acceleration. This would explain why the alongshore advective acceleration term is not necessary for the 12mN momentum budget, while it is necessary for the 12mS budget. It also explains why, given our location for the advective acceleration estimate, it only contributes to closing the budget for one flow direction (southwards). Our observations of stronger alongshore velocities at 12mS (compared to alongshore velocities at 12mN) agree with this hypothesis of local acceleration.

Following Kumar et al. (2015), the relative importance of the advective acceleration to the bottom drag is highlighted by some elementary scaling analysis, using values from the 12mS mooring. The ratio of these two terms is roughly written as

$$p = \frac{U_j}{U_i} \frac{D\Delta U_i}{U_i C_D \Delta x_j}, \tag{1.14}$$

where $i, j = 1, 2$, U_i is a characteristic depth-averaged velocity, C_D is the drag coefficient, D is depth, and ΔU_i is the horizontal difference in depth-averaged velocity. Consider, the ratio of the alongshore advective acceleration to the bottom drag, using the standard deviations of the velocities as their characteristic magnitude. From our data at 12mS, $|\Delta U| \sim 0.029$ m s^{-1} and oscillates on a semidiurnal cycle, 180° out of phase with the depth-averaged velocity, suggesting convergence or divergence in the alongshore direction. Given $\Delta x = 257.5$ m, $U \sim 0.16$ m s^{-1}, $D \sim 12$ m, and $C_D \sim 0.0023$, the ratio of the alongshore advective acceleration to the bottom drag is $p = 3.7$, indicating that these are, roughly, of similar importance. This suggests that the advective acceleration could play an important role in reef environments with highly variable bathymetry.

As previously mentioned, the tidal phase averages were taken to follow the phase of the alongshore velocity (U), instead of the phase of the sea surface displacement (η), since the momentum budget terms have a much clearer coherence with the former. This suggests that internal tides may be playing a role in modifying the alongshore pressure gradient in the nearshore region. Oahu is in a region of intense internal tide activity. Using the Princeton Ocean Model (POM), Carter et al. (2008) estimate that 85% of the semidiurnal barotropic tidal energy lost over the Hawaiian Ridge is converted into internal tides. The energy flux of the semidiurnal internal tide is an order of magnitude larger than that of the diurnal internal tide (Smith et al., 2017). Specifically, given that our study site is near Kaena Ridge, observed to generate intense

internal tides (Nash et al., 2006), it is likely that the measured pressure gradients and the resulting velocities are primarily driven by the evanescent tail of the M_2 internal tide propagating in deeper stratified waters offshore, which influences the nearshore region, despite the lack of local stratification. Similar internal tidal currents have been previously observed at other unstratified locations in Hawaii (Smith et al., 2016).

The bottom drag plays a significant role in this momentum budget, particularly at 12mN; but the drag coefficients estimated here (median drag coefficients of $C_D = 0.0080$ $[-0.002, +0.004]$ and $C_D = 0.0023$ $[-0.0006, +0.0009]$ at 12mN and 12mS, respectively) are on the lower end of those previously reported for tropical coral reefs. According to a summary of C_D estimates provided by Rosman and Hench (2011), results from a variety of studies initially show drag coefficients ranging from $C_D = 0.009$ to $C_D = 0.8$. After converting the various formulations of C_D to a common definition, Rosman and Hench (2011) constrain this range to $C_D = 0.01 - 0.12$, closer to our estimates for the 12mN mooring. Some of the variability in C_D in the literature may be attributed to the depth dependence of C_D (Lentz et al., 2017; McDonald et al., 2006). Higher drag coefficient are reported in shallower environments, such as in Coronado et al. (2007; $C_D = 0.015$ when $D \sim 5$ m), Lentz et al. (2016; $C_D = 0.03$ when $D \sim 1.2$ m), Lowe et al. (2009b; $0.01 < C_D < 0.03$ in a reef-lagoon system), and Rogers et al. (2018; $C_D \sim \mathrm{O}(0.01)$ - $\mathrm{O}(0.1)$ when $D \sim 1 - 3$ m). However, if there is a large depth to hydrodynamic roughness ratio ($\frac{D}{z_0} > 100$, where z_0 is the hydrodynamic roughness) and a large depth to coral roughness ratio ($\frac{D}{h} > 10$, where h is the coral roughness), then $C_D \to 0.01$ (Lentz et al., 2017; McDonald et al., 2006). This may account for why the median C_D at 12mN is comparable to values estimated by Reidenbach et al. (2006) ($0.009 < C_D < 0.016$) in the forereef region, despite much larger roughness for the latter case (mean roughness of 20 cm with a 16 cm standard deviation). As in Reidenbach et al. (2006), both conditions $\left(\frac{D}{z_0} > 100, \frac{D}{h} > 10\right)$ are met at our study site, though our roughness estimates have large uncertainties and variability.

On the other hand, the phase-averaged C_D values calculated for our 12mS mooring, differ

from the estimated $C_D \approx 0.01$ for $\frac{D}{z_0} > 100$, given $\frac{D}{h} > 10$ (Lentz et al., 2017; McDonald et al., 2006); they are, instead, comparable to Reidenbach et al. (2006)'s estimate for a sandy bottom ($0.002 < C_D < 0.004$) and the canonical C_D for a sandy bed (Monismith, 2007). Wave spectra at both locations were nearly identical; the difference in drag between our northern and southern moorings is probably related to local differences in the physical roughness between sites, rather than an increase in the apparent roughness of the environment (Grant and Madsen, 1979).

1.6 Summary

The tidal momentum balances estimated here show the relevant forcing terms that dominate across a semidiurnal cycle at two different alongshore locations on the 12 m isobath of a fore-reef. Although the moorings are in an unstratified environment, coherence analyses suggest that the internal tide plays a role in setting the phase of the momentum budget terms. At the northernmost location, where no sharp changes in bathymetry were observed, the momentum balance is between the unsteadiness, pressure gradient, and bottom drag term. However, at the southernmost mooring, situated near a bathymetric step, the alongshore advective acceleration plays a comparable role to the bottom stress. At both locations, drag coefficients are $O\left(10^{-3}\right)$. The along-shore analysis presented here is of particular interest in adding to more extensive research on cross-shore momentum budgets over coral reefs. Particularly, the importance of the alongshore advective acceleration at the 12mS mooring suggests that variations in bathymetry, like those associated with spur and groove formations, can have consequences for alongshore physical and biological dispersion (e.g. sediments, pollutants, larvae).

Acknowledgments

This research was conducted with Government support under and awarded by the Department of Defense (DoD) through the National Defense Science and Engineering Graduate Fellowship (NDSEG) Program, as well as the Office of Naval Research award N00014-13-1-0340. Wind velocity output was acquired from Yi-Leng Chen (School of Ocean and Earth, Science and Technology; University of Hawai'i, Honolulu); we thank him for his permission and guidance. We also thank two anonymous reviewers for their comments and insight, which undoubtedly improved the final manuscript. Data used in this research are posted online as part of the UCSD Library Digital Collections (doi: 10.6075/J09G5K1F).

Chapter 1, in full, is a reprint of the paper "An Alongshore Momentum Budget Over a Fringing Tropical Fore-Reef" published in Journal of Geophysical Research: Oceans by I. B. Arzeno, S. N. Giddings, G. Pawlak, and M. Merrifield in 2018. The dissertation author was the primary investigator and author of this paper.

Appendix A: Log fits

For each time step, successive nonlinear fits with incremental depths are applied to non-interpolated velocity profiles to find the four parameters in equation 1.8. At a time t_i, a fit is done from the first bin (at $z \sim 1$ mab) to $z \sim 0.25D$, where D is the water depth. Then, the fit at t_i is repeated a number of times, each time adding an extra bin to the fit, until the last bin in the fit reaches $z = 0.40D$. The ADCP bins are considered to be independent, although some overlap is expected, since the length of the transmit pulse (0.37 m) is larger than the bin size (0.25 m). If $Ri > 0.25$ anywhere in the velocity profile, the fit is invalidated. The boundary layer thickness (δ) is defined as the highest bin in each fit. Of all the fits corresponding to t_i, only the one with the largest R^2 is saved, and it is only used in this analysis if $R^2 > 0.95$. The process is repeated three times at each location, using alongshore velocities with their associated instrument error (Appendix B) being (1) added, (2) subtracted, or (3) neglected.

Appendix B: Uncertainty calculations

Any term F in our analysis that is a function of independent variables χ_i has an uncertainty σ_F calculated according to error propagation

$$\sigma_F^2 = \sum_{i=1}^{N} \left(\frac{\partial F}{\partial \chi_i} \sigma_\chi \right)^2 . \tag{1.15}$$

The first type of uncertainty accounted for is instrument error. In particular, the uncertainty in ADCP velocities comes from long-term instrument accuracy ($\sigma_{\text{long}} \sim 0.0025$ m s^{-1}), heading and motion errors ($\sigma_{\text{head}} \sim 0.0005$ m s^{-1}), and statistical uncertainty after averaging pings ($\sigma_{\text{stat}} \sim 0.0014$ m s^{-1}). In total, the ADCP velocity error is $\sigma_{\text{u}} \sim 0.005$ m s^{-1}, before depth-averaging. The uncertainty in the ADCP timestamp ($\sigma_{\text{time}} \sim 0.01$ s), as well as from pitch and

roll, is taken from Giddings et al. (2014). The uncertainty in depth calculations is equal to that from the ADCP pressure sensor (0.1 % of the total pressure). The uncertainty in the pressure gradient stems from the error in the quartz pressure sensors (0.01 % of the total pressure).

To compute the uncertainty in the median momentum budget terms along a tidal cycle (Figure 1.5), phase averaging was performed three different ways: (1) using the terms with no uncertainty, (2) using the terms with the upper uncertainty limit applied, and (3) using the terms with the lower uncertainty limit applied. As part of the phase-averaging, the median is calculated from each of those three iterations, and we assign a 95% confidence interval from bootstrapping (with $n = 10,000$ random samplings). Figures 1.5 and 1.6 show the medians corresponding to the phase-averaging performed using data without uncertainty. However, the lower and upper bounds for the confidence intervals come from taking the minimum and maximum bootstrap uncertainty, respectively, in all three of the iterations previously described. The confidence intervals for the phase-averaged momentum budget terms are, presumably, conservative estimates of the true uncertainty. Error stemming from the GPS locations, rotations to the along and cross-shore axes, or interpolations/extrapolations are not accounted for.

Appendix C: Additional log fit statistics

Table 1.4: Mean values of log-fit parameters taken from entire time series

	12mN	**12mS**
% with $R^2 \geq 0.95$	72%	53%
u_*	0.016 ± 0.002	0.01 ± 0.0012
z_0	0.17 ± 0.05	0.028 [-0.01, + 0.02]
z_{ref}	0.029 [-0,.02 +0.002]	0.0018 [-0.0006, + 0.003]
δ	3.80 [-0.03, + 0.04]	3.68 [-0.03, + 0.04]
C_D	0.0086 [-0.003, +0.01]	0.0032 [-0.001, +0.002]
C_D^+	0.0076 [-0.003, +0.006]	0.0035 [-0.002, +0.005]
C_D^-	0.0094 [-0.003, +0.02]	0.0030 [-0.0008, +0.001]

Note. The asymmetric confidence intervals result from using bootstrap methods.
$^+$ Drag coefficients calculated using positive alongshore, depth-averaged velocities.
$^-$ Drag coefficients calculated using negative alongshore, depth-averaged velocities.

Chapter 2

Generation of Quasi-Biweekly Yanai Waves in the Equatorial Indian Ocean

Abstract

The spatial and temporal structure of quasi-biweekly Yanai waves in the Indian Ocean and their relationship to wind stress are uniquely described using satellite observations of sea level anomalies and wind velocities, previously approximated only using theory, numerical models, and discrete mooring observations. Yanai waves represent a significant contribution to antisymmetric sea level anomaly variability in the 10-20 day band. Robust climatologies produced using seventeen years of data (spanning 45°–95°E and 10°S–10°N) reveal a clear spatio-temporal pattern and are consistent with Yanai wave generation in the western equatorial Indian Ocean during monsoon seasons. Spectral and correlation analyses imply that Yanai waves are linearly forced by wind stress patterns with similar wavelengths. A new method of assembling data composites shows the first full structure of a vertical mode-2 Yanai wave moving across the equatorial Indian Ocean under westward propagating wind vortices.

Plain Language Summary

We use sea surface height (SSH) and wind velocity data gathered by satellites to study a large-scale wave in the Indian Ocean (also known as a Yanai wave) that has previously only been understood using theory, numerical models, and limited data. Yanai waves account for a significant portion of the 10–20 day variability in the equatorial Indian Ocean SSH. After analyzing seventeen years of satellite data (spanning 45°–95°E and 10°S–10°N), we deduce that Yanai waves with a period of around 14 days are generated, primarily, in the western part of the equatorial Indian Ocean during the summer and winter monsoons, a pattern that was not previously understood. We find that the wind structure driving these Yanai waves is a set of vortices with a similar scale as the wave itself. Finally, we come up with a method that allows us to visualize, for the first time in the literature, the full Yanai wave propagating across the equatorial Indian Ocean.

2.1 Introduction

Yanai waves (also known as mixed Rossby-gravity waves) contribute to intraseasonal variability and play a major role in driving convergent heat flux at the equator (Nagura et al., 2014; Smyth et al., 2015), upwelling (Horii et al., 2011; Kumar et al., 2012; Masumoto et al., 2008; Sengupta et al., 2004; Tsai et al., 1992), and, possibly, mixing in the abyssal ocean (Holmes et al., 2016). Although Yanai waves have been studied in the Atlantic and Pacific Ocean (Ascani et al., 2010; Bunge et al., 2007; Farrar and Durland, 2012; Lyman et al., 2007; Shinoda, 2012), this research focuses on the equatorial Indian Ocean, where prevalent oceanic, atmospheric, and biological patterns differ from other basins. (Schott and McCreary, 2001; Schott et al., 2009). This research aids in furthering our understanding of biogeochemical processes in the equatorial Indian Ocean. Planetary waves have been previously shown to play a role in observed chlorophyll patterns through horizontal advection (Killworth et al., 2004) and nutrient upwelling (Uz et al.,

2001). Studies in the tropical Pacific and Indian Ocean have shown chlorophyll enhancement associated with the presence of 20-day tropical instability waves (Strutton et al., 2001) and Yanai waves (Strutton et al., 2014).

Two main classes of Yanai waves have been studied in the Indian Ocean: low-frequency (period $\sim$ 26 days) and high-frequency (or quasi-biweekly) Yanai waves (period $\sim$ 15 days). Most earlier literature focuses on the generation of low-frequency Yanai waves in the western basin by direct wind forcing (Kelly et al., 1995; McCreary, 1984) and current instabilities (Kindle and Thompson, 1989; Moore and McCreary, 1990). Some recent research on low-frequency Yanai waves considers both of these generation mechanisms (Chatterjee et al., 2013) and also examines the presence of these waves in the central equatorial Indian Ocean (David et al., 2011). However, much of the recent research (and this work), focuses on the dynamics of higher frequency quasi-biweekly Yanai waves.

Sengupta et al. (2004) associate quasi-biweekly Yanai waves with a quasi-biweekly wind structure, described by Chen and Chen (1993) as a pair of coupled vortices that originate in the western Pacific and propagate westward/northwestward across the Indian Ocean. One of the vortices described by Chen and Chen (1993) is situated near the equator, where oceanic Yanai waves are present. The other vortex in the coupled pair, found around 15-20° North, is believed to play a role in monsoonal dynamics (Annamalai and Slingo, 2001; Chatterjee and Goswami, 2004; Chen and Chen, 1993). Sengupta et al. (2004) note that quasi-biweekly Yanai waves are absent in runs forced only by seasonal winds; and Rao et al. (2017) find a high coherence in the 10–20 day period band between meridional winds and meridional currents at one particular mooring. Miyama et al. (2006) discuss resonance between quasi-biweekly wind stress and quasi-biweekly Yanai waves using an analytical and numerical model. On the other hand, Chatterjee et al. (2013) show that quasi-biweekly Yanai waves can also be forced by current instabilities.

Much of the research concerning quasi-biweekly Yanai wave generation in the Indian Ocean is based on a combination of numerical models (Chatterjee et al., 2013; Miyama et al.,

2006; Ogata et al., 2008; Sengupta et al., 2004) and current velocity data from spatially sparse moorings, mostly focused in the eastern equatorial Indian Ocean (Masumoto et al., 2005; Murty et al., 2006; Rao et al., 2017). In this study we use publicly available satellite altimetry and scatterometer data to study the generation and characteristics of quasi-biweekly Yanai waves in the equatorial Indian Ocean, as part of the larger NASCar project (Centurioni et al., 2017). Our purpose is to provide a comprehensive picture of the spatio-temporal patterns of the equatorial Indian Ocean Yanai waves and their generation, using only observations.

2.2 Data and Analysis Methods

The satellite data used for this analysis consist of (1) daily delayed-time gridded sea surface heights (SSH) processed by the SL-TAC multimission altimeter data processing system and distributed by the European Copernicus Marine Environment Monitoring Service (CMEMS, 2019; Pujol et al., 2016); and (2) daily averages of wind velocities from the 6-hourly cross-calibrated, multiplatform (CCMP) ocean surface wind project (Atlas et al., 2011; NASA/GSFC/NOAA, 2009). Both data sets have a 0.25° x 0.25° horizontal resolution. The time period considered here is 1994-2010. We assume an error variance of 17 cm^2 for the Copernicus Marine Environment Monitoring System (CMEMS) altimetry product, based on a combination of uncorrelated noise in the along-track measurements (Table 1 in Fu and Cazenave (2000)), long-wavelength errors (Pujol et al., 2016), and uncertainty from creating a gridded map of merged data (Table 3 in Taburet et al. (2019)). We will also assume that daily averages of wind velocities have a maximum error variance of 2.9 m^2/s^2, which takes into consideration the variance derived from the difference between satellite measurements and moored buoys, as well as between the final mapped product and satellite measurements (Atlas et al., 2011). All variance is assumed to be white noise.

The Yanai wave sea surface displacement is described using the antisymmetric sea level anomaly (ASLA):

$$\mathrm{ASLA} = \frac{1}{2}\left(\mathrm{SLA}_n - \mathrm{SLA}_s\right), \tag{2.1}$$

where SLA_n and SLA_s are meridional averages of sea level anomalies north and south of the equator, respectively (Yanai and Murakami, 1970). Meridional averages are taken between $\pm 2.5^\circ$ and $\pm 3.5^\circ$, one to two Rossby radii away from the equator, where the Yanai wave SSH signal is strongest (Chatterjee et al., 2013; Tsai et al., 1992). Averaging reduces the ASLA variance from 17 cm^2 to 2.1 cm^2.

Figure 2.1a presents the 2D power spectral density (PSD) of ASLA vertical velocity (dASLA/dt), a quantity that can be readily compared to theory and applied to studies of biological productivity. PSDs presented here reflect an average of spectral analyses conducted using successive sub-records (each 2 years long), tapered using Kaiser-Bessel windowing and overlapped by 50%. No wavenumber band averaging was performed, in order to maintain the best wavenumber resolution. The frequency and wavenumber resolution are $1/(668$ days) and $\sim 1/(5350$ km), respectively. Though the merged SLA product resolves a spatial variability ~ 400 km near the equator, it only resolves a mean temporal variability ~ 10 days at the same locations (Pujol et al., 2016). Thus, the PSD amplitude at our periods of interest may be underestimated.

The most energetic regions in the 2D spectra (Figure 2.1a) fall along the theoretical Yanai wave dispersion curves for the first two baroclinic modes:

$$k = \frac{\omega}{c_n} - \frac{\beta}{\omega}, \tag{2.2}$$

where ω is the frequency, k is the zonal wavenumber, β is the meridional derivative of the Coriolis parameter, and c_n is the nth mode baroclinic Kelvin wave phase speed, following Chatterjee et al. (2013). The integrated variance in the wavenumber bands that intersect the dispersion curves

for the first three modes accounts for about 45% of the signal in the 10-20 day frequency band (Figure 2.1a). The Indian Ocean basin is too small for the 2D spectra to properly resolve the different Yanai wave vertical modes, in contrast to some previous studies in the Pacific Ocean, where the 2D spectra show a clear separation between different vertical modes (e.g. Farrar and Durland, 2012; Shinoda, 2012).

A separate spectral technique based on sea surface slope (Appendix A) is also employed to estimate wavenumber as a function of frequency in the western, central, and eastern equatorial Indian Ocean. This method complements the 2D PSD (Figure 2.1a), since it is not limited by the artificial discretization of wavenumbers associated with Fourier decomposition. Wavenumbers estimated using data between $70-90^{\circ}$E lie mostly along the Yanai wave dispersion curve for the first vertical mode ($n=1$) at 10–12 day periods, whereas values for k estimated using data between $50-70^{\circ}$E, along with a few k from the eastern region, lie mostly along the Yanai wave dispersion curve for the second vertical mode ($n=2$) at quasi-biweekly periods and longer (Figure 2.1a). The significant energy in the dASLA/dt PSD, with wavenumber estimates lying along the appropriate dispersion curves (showing a predominantly mode 2 signal in the western ocean and a predominantly mode 1 signal in the eastern ocean), confirms that satellite SLA data capture the equatorial Indian Ocean Yanai wave surface signature.

Although other mechanisms have been proposed for Yanai wave generation (e.g. Chatterjee et al., 2013), here we focus on wind forcing. As denoted in Miyama et al. (2006), the Yanai wave meridional wind forcing is associated with the meridional wind stress (τ^y), whereas the zonal wind forcing of Yanai waves is related to $(\sigma/\beta)\,\partial\tau^x/\partial y$, where τ^x is the zonal wind stress, σ is the wind frequency, and β is the meridional derivative of the Coriolis parameter. The wind stress $\left(\tau^i\right)$ is generally parameterized as

$$\tau^i = \rho_a C_D u_i^w (u_j^w u_j^w)^{1/2}, \tag{2.3}$$

where $\rho_a = 1$ kg/m^3, $C_D = 0.0013$ (Miyama et al., 2006), u_i^w is the ith component of the wind velocity, and $i = 1,2$ and $j = 1,2$ are the horizontal components of a variable, following Einstein notation. Both the meridional wind stress (τ^y) and the meridional gradient of the zonal wind stress ($\partial\tau^x/\partial y$) were averaged between 0.5°N and 0.5°S, in keeping with the 1° range chosen to average ASLA. The variances associated with τ^y and $\partial\tau^x/\partial y$ are 9.3x10^{-4} $\left(\mathrm{N/m^2}\right)^2$ and 3.3x10^{-8} $\left(\mathrm{N/m^3}\right)^2$, respectively.

Informed by the PSD (Figure 2.1a), we bandpass-filter the ASLA (with its respective error) in time to encompass 10–20 day variability; additionally, we low-pass filter the data in space to consider only wavelengths greater than 1500 km. The same processing is applied to τ^y and $\partial\tau^x/\partial y$. The resulting error associated with ASLA and wind-related quantities are an order of magnitude smaller than the band-passed signals themselves (Appendix B). Finally, the mean frequency of our bandpass-filtered $\partial\tau^x/\partial y$ is estimated for every location via spectral analysis and used to construct $(\sigma/\beta)\,\partial\tau^x/\partial y$.

2.3 Results

A subset of filtered data (Figure 2.1b–d) depicts wave phase in the ASLA time series propagating westward while groups advance eastward, as expected from theory. For the most part, τ^y, $(\sigma/\beta)\,\partial\tau^x/\partial y$, and ASLA exhibit concurring spatio-temporal patterns, with magnitudes modulated in space and time. Climatologies of τ_y and ASLA show peaks in amplitude from $50-70$°E in January and May–September, with minima in February–April and November–December (Figure 2.2 a–b and e–f). The peaks in τ^y and ASLA amplitude coincide with the Indian summer and winter monsoon seasons (Schott and McCreary, 2001). The climatology of $(\sigma/\beta)\,\partial\tau^x/\partial y$ shows a peak from $70-80$°E in November and has values that are an order of magnitude smaller than τ^y. Although wind forcing does not show any outstanding peaks in amplitude on the far eastern side of the basin, ASLA amplitudes escalate east of 80°E, as has

been previously noted in the literature (Chatterjee et al., 2013; Miyama et al., 2006; Sengupta et al., 2004).

Cross-spectral analysis between the meridional wind stress and ASLA shows that τ_y leads

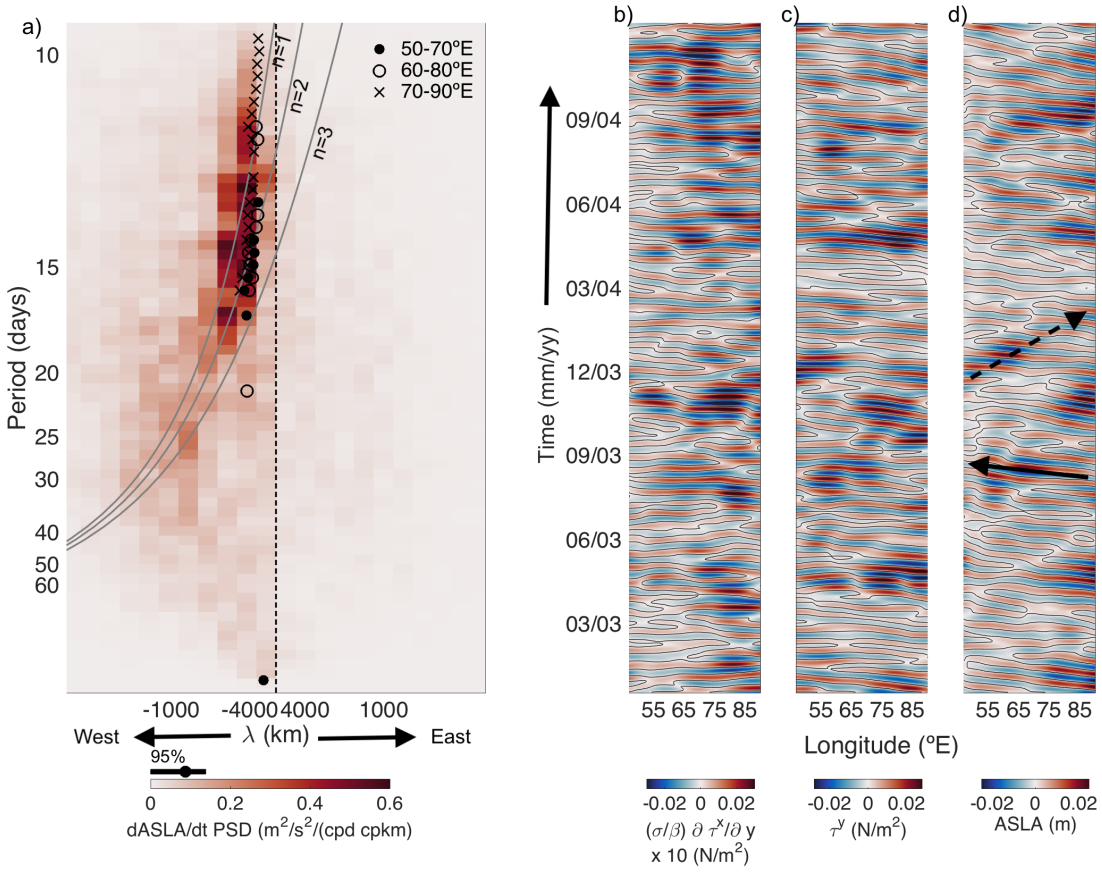

Figure 2.1: (a) 2D power spectral density (PSD, red colorbar) of ASLA vertical velocity (dASLA/dt), with dispersion curves for the first three Yanai wave vertical modes (n=1, 2, 3) in grey. The dots, circles, and crosses denote the wavenumbers estimated from the sea surface slope spectra (Appendix A) using three different longitudinal ranges representing the western, central, and eastern regions of the equatorial Indian Ocean (50–70°E, 60–80°E, and 70–90°E, respectively). The 95% confidence interval was estimated following Emery and Thomson (2001). (b–c) Hovmöller diagrams for zonal wind forcing $((\sigma/\beta)\partial\tau^x/\partial y)$ and meridional wind forcing (τ_y), averaged between 0.5°N and 0.5°S. (d) Hovmöller diagram of ASLA. A dashed black arrow highlights an example of eastward group propagation, and a solid black arrow shows westward phase propagation. Plots (b)–(d) include only 2 of the 17 years of data in our analysis. Signal error for both wind forcing and ASLA is an order of magnitude smaller and has not been included in the Hovmöller diagrams.

ASLA by about 2–3 days across the equatorial Indian Ocean. Cross-spectral analysis by Rao et al. (2017) also showed a 2-day lag between satellite wind data and current velocities from a mooring at the equator and 90° E. High coherence between τ_y and ASLA occurs between $50-60$°E at a period of around 16 days (Figure 2.2g), while lower coherence is seen to extend between

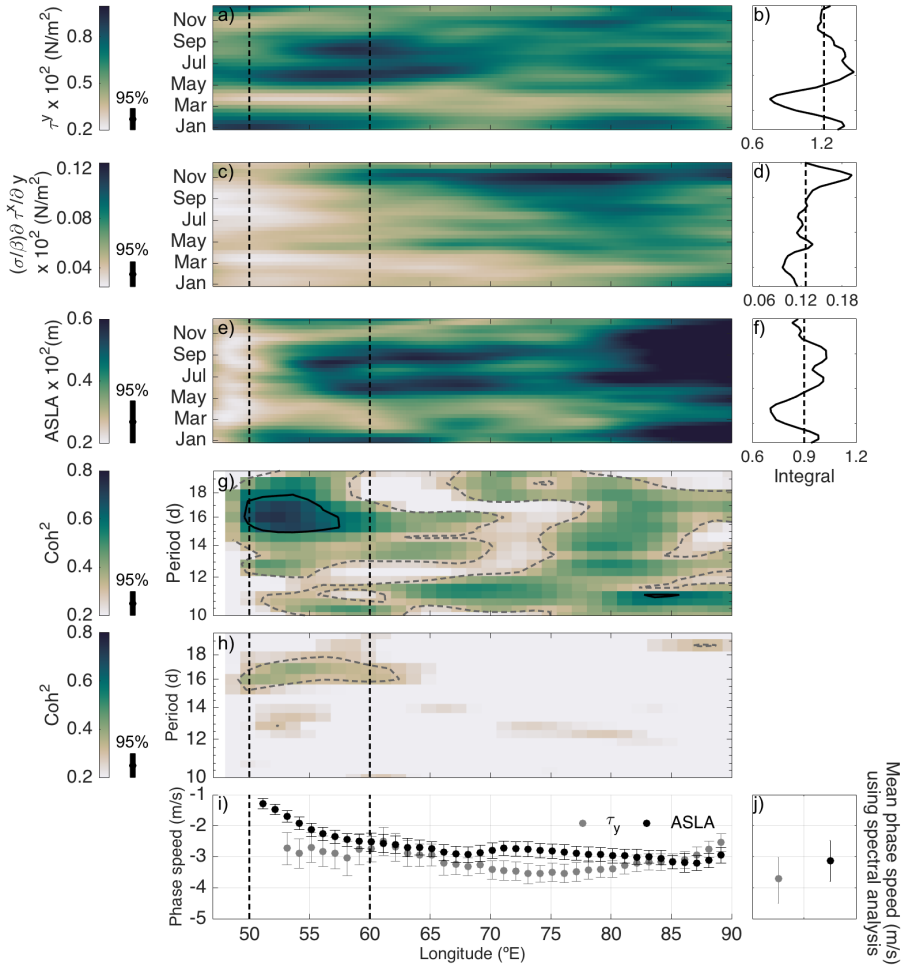

Figure 2.2: Climatologies (averages of magnitudes across 17 years) of meridional Yanai wave wind forcing, zonal Yanai wave wind forcing, and ASLA, as a function of longitude (a, c, e), and their respective zonal integrals (b, d, f). Squared coherence between (g) τ^y and ASLA and (h) $\partial\tau^x/\partial y$ and ASLA. Contours in the coherence plots delineate $\text{coh}^2 = 0.6$ (solid black line) and $\text{coh}^2 = 0.3$ (grey dashed line). All color plots have their 95% confidence intervals included alongside their respective colorbars. Estimates of westward phase speeds using auto-correlations (i) and cross-spectral analysis (j) are included, with 95% confidence intervals. Vertical dashed lines highlight longitudes where the largest coherence between τ^y and ASLA is observed.

periods of 10–20 days, east of 80°E. This agrees with the information in Figure 2.1a, where some wavenumbers estimated for the eastern region of the equatorial Indian Ocean correspond to shorter periods than those in the western basin. This could indicate that some Yanai waves on the eastern and western side of the Indian Ocean are generated locally and, hence, dynamically different. However, the lower coherence between wind and ASLA in the eastern region of the basin suggests that the signal in the eastern region of the basin is not locally generated. Some of these regions of lower coherence may also be attributed to the inertial response of the ocean, since the inertial period between 2.5°E and 3.5°E varies from 11.4 to 8.2 days, respectively. The coherence between $\partial\tau^x/\partial y$ and ASLA is much lower than that between τ_y and ASLA (Figure 2.2h), indicating that the meridional wind stress is the primary wind forcing for Yanai waves.

Phase speeds for τ_y and ASLA were estimated using auto-correlations (Figure 2.2i) and cross-spectral analysis (Figure 2.2j) among data at different longitudes (Appendix C). Both methods agree, within error bounds, though the average phase speed computed using cross-spectral analysis is slightly larger westward (i.e. more negative) than that from the auto-correlations. The average phase speed for τ_y was estimated to be -3.11 [-0.26, +0.45] m/s using auto-correlations and -3.70 [-0.80,+0.70] m/s using cross-spectral analysis. On the other hand, the average phase speed for ASLA was estimated to be -2.68 [-0.11, + 0.35] m/s using auto-correlations and -3.12 [-0.68,+0.64] m/s using cross-spectral analysis. Estimates of the ASLA phase speed from auto-correlations suggest that the magnitude gradually declines from east to west until about 55°E, where the magnitude decreases rapidly. The average period for 10–20 day ASLA, estimated using spectral analysis, varies with longitude, increasing steadily from 14.5 days on the eastern side of the basin to 16.5 days on the western side of the basin (not shown), mirroring the decrease in phase speed magnitude. These variations in period and phase speed may point to Doppler shifting from equatorial currents, discussed in Section 4. The mean period for 10–20 day wind stress remains steady (period $\sim$ 14 days) across longitudes. ASLA and τ_y wavelengths— estimated using auto-correlation phase speeds and mean periods— are comparable east of 55°E, where the

ASLA's average wavelength is $\lambda_{ASLA} = 3700 \pm 400$ km, roughly 63% of the equatorial Indian Ocean width. The average wind stress wavelength ($\lambda_{\tau_y} = 3700 \pm 600$ km) is mostly constant in longitude. West of 55°E, the ASLA's average wavelength is shorter ($\lambda_{ASLA} = 2300 \pm 700$ km).

A composite image of Yanai wave propagation (Figure 2.3 b–g) was assembled by averaging 10–20 day bandpass-filtered time series of satellite sea level anomalies and wind velocities as a function of a representative Yanai wave phase. To determine Yanai wave phase over the 17–year record of satellite observations, we use a time series ($\tilde{\Theta}(t)$) extracted using Hilbert Empirical Orthogonal Functions, (HEOFs; Barnett, 1983; Fewings, 2017), where each interval between peaks in $\tilde{\Theta}(t)$ constitutes one full Yanai wave oscillation ($\phi = 0 - 2\pi$).

Let $\zeta(x,t)$=[SLA$_n(x,t)$; SLA$_s(x,t)$] be a scalar field, where the spatial (x) and temporal (t) information are in the first and second dimension, respectively (SLA$_n$ and SLA$_s$ defined in equation 1). After normalizing each $\zeta(x,t)$ time series by its standard deviation, we construct a complex signal (χ) by adding a phase shift to the original signal, such that

$$\chi(x,t) = \zeta(x,t) + i\hat{\zeta}(x,t), \tag{2.4}$$

where $\hat{\zeta}(x,t)$ is the temporal Hilbert transform of ζ, and the Hilbert transform represents the original signal shifted in temporal phase by $-\pi/2$. As in classical Empirical Orthogonal Function (EOF) analysis, $\chi(x,t)$ can be decomposed into individual spatial and temporal components,

$$\chi(x,t) = \sum_m \Theta_m(t)\gamma_m^*(x), \tag{2.5}$$

where $\Theta(t)$ is the complex temporal amplitude, $\gamma(x)$ is the complex spatial amplitude, (*) represents the complex conjugate of a signal, and m is an orthogonal mode. We work with the real part of the complex components, since the imaginary part primarily represents a phase shift of the real

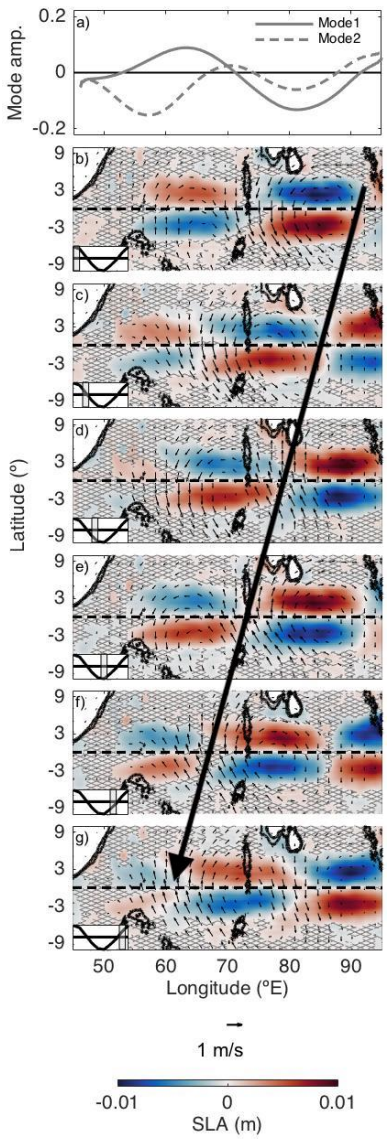

Figure 2.3: (a) Real part of the spatial amplitude pertaining to the first two ASLA HEOF modes (Re[$\gamma_{1,2}$]). (b-g) Phase averages of 10–20 day bandpass-filtered satellite SLA (color) and wind velocities (vectors). Averages were done following the phase of $\tilde{\Theta}(t)$, as described in Section 3. The insets show the average ASLA cycle (solid line) and the phase represented in each subplot (shaded area). The hatching denotes areas where SLA phase averages are not statistically different from zero. The arrow traces the propagation of a node throughout a cycle. Contours delineate the 0 and 1 km isobaths, from the ETOPO1 Global Relief Model.

part.

The first HEOF mode ($m = 1$) accounts for 37% of the variance in $\chi(x,t)$, and the real part of its spatial amplitude (Re[γ_1]) is antisymmetric about $\phi \sim 70°$E. The second HEOF mode ($m = 2$) describes 25% of the variance; Re[γ_2] is asymmetrical across longitudes and has peak amplitude on the western side of the basin (Figure 2.3a). Thus, we assume that the dominant Yanai wave structure is encompassed in the first HEOF mode. The relatively low variance explained by the first HEOF mode may be because our large array increases the potential that coherence is lost along the array (Merrifield and Guza, 1990).

The Yanai wave phase for the composite averages ($\tilde{\Theta}(t)$) is defined using the real part of the temporal amplitude for the first HEOF mode: $\tilde{\Theta}(t) = Re[\Theta_1(t)]$. It is important to note that $\tilde{\Theta}(t)$ is only a representative time series used to define the Yanai wave phase; the composites themselves were created by averaging the original satellite data. Composites made with the Yanai wave phase defined using time series from a specific location (for example, with the time series at 85°E) lead to images with enhanced amplitude near the time series location and lose some of the Yanai wave structure farther away, as seen in Ogata et al. (2008) and Sengupta et al. (2004). Our composites (Figure 2.3) provide a synoptic representation of the basin wide propagating Yanai wave structure.

The composites (Figure 2.3) are averages over 254 Yanai wave cycles (the cycles in $\tilde{\Theta}(t)$ with the largest amplitudes). The average period of $\tilde{\Theta}(t)$ is 14.0 ± 0.2 days. The average wavelength observed in the composites is $\lambda \sim 4100$ km. The average wind velocity structure in the composite exhibits a form reminiscent of a vortex propagating westward (Figure 2.3 b-g), consistent with the Chen and Chen (1993) description.

2.4 Discussion

Although the energy in ASLA is broad-banded in both frequency and wavenumber (Figure 2.1), the wave structure visible in the composite image is characterized by a distinct wavelength and period ($\lambda \sim 4100$ km and $T \sim 14.0$ days) that corresponds to an $n = 2$ Yanai wave (Chatterjee et al., 2013; Miyama et al., 2006; Ogata et al., 2008), where n refers to the vertical mode. This agrees with Miyama et al. (2006)'s finding that the second vertical mode is the most resonant biweekly mode in the equatorial Indian Ocean.

The phase speed for the wave structure shown in the composite is $c \sim -3.4$ m/s, within the error bars of the cross-spectral estimates (Figure 2.2j), slightly lower (stronger westward) than the auto-correlation estimates (Figure 2.2i), and falling within the values previously reported in studies using numerical models or discrete mooring (1.8–5.4 m/s and 2.5–5 m/s reported by Ogata et al. (2008) and Sengupta et al. (2004), respectively). The composite average wavelength is also within the uncertainty estimates of the mean wavelengths derived from the phase speed estimates in Figure 2.2i ($\lambda_{ASLA} = 3700 \pm 400$ km, $\lambda_{\tau_y} = 3700 \pm 600$ km) and within the ranges reported by Sengupta et al. (2004) for ASLA ($\lambda = 2100 - 6100$ km) and wind ($\lambda = 3000 - 4500$ km). Chen and Chen (1993) report a larger wavelength, $\lambda \sim 6000$ km, for the quasi-biweekly wind structure. The differences between the phase speeds/wavelengths from the Figure 2.3 composites and those from the Figure 2.2i autocorrelations are likely indicating that the Yanai wave signal recorded by the altimeters and reflected in Figure 2.2 is a superposition of various vertical modes, whereas the composites are focusing, largely, on one vertical mode ($n = 2$). In fact, the wavelengths from the auto-correlation analysis lie between the values expected for an $n = 1$ Yanai wave ($\lambda = 2600$ km) and an $n = 2$ Yanai wave ($\lambda = 4800$ km), assuming $T = 14$ days and taking the Kelvin wave phase speed from Chatterjee et al. (2013). This is not surprising since the data spans both dispersion curves (Figure 2.1a). The superposition of different vertical modes can lead to the creation of wave beams that transport energy downward and eastward, reflecting off the bottom

and pycnocline, and leading to eastern intensification of the Yanai wave signal (Chatterjee et al., 2013; Miyama et al., 2006; Moore and McCreary, 1990), as seen in Figure 2.2e. Energy that accumulates on the eastern basin is then redistributed by propagating as coastal-trapped Kelvin waves (McCreary, 1984).

Despite the differences between the ASLA and τ_y phase speeds, a similar average wavelength is estimated for both structures. The mean periods estimated for ASLA and τ_y, using spectral analysis, vary zonally, a result of Doppler shifting induced by the interaction of the ASLA signal with equatorial currents on the western side of the Indian Ocean. The current velocity needed to account for the difference between a $T_E = 16$ day period in the western Indian Ocean (where T_E represents the period measured relative to the Earth) and the average period in the first ASLA HEOF mode ($T = 14$ days, the intrinsic period, taken to be the period in the frame of reference of the current) can be estimated as

$$U = (\omega_E - \omega)/k, \tag{2.6}$$

where U is the current velocity, ω and ω_E are the intrinsic and observed frequencies, respectively, and k is the wavenumber ($k = -2\pi/3.7\text{x}10^6$ m, in this case). As a result, a period of $T = 14$ days can be Doppler shifted to $T_E = 16$ days with a current velocity of $U = 0.38$ m/s. The average velocity for the Indian Ocean South Equatorial Counter Current (SECC) has been reported as $U = 0.26 \pm 0.22$ m/s, at an average location of $2.6^\circ \pm 1^\circ$S (Beal et al., 2013). Given that ASLA is derived using meridional averages of data between $\pm 2.5 - 3.5^\circ$, it is possible that the SECC could be playing a role in shifting the observed ASLA period and, hence, phase speed. This Doppler shifting may also explain why the coherence in the western basin is strongest at periods closer to $T = 16$ days (Figure 2.2g).

Given that wavelength and period estimates for ASLA and τ_y are similar, we can deduce that the Yanai wave is a linear response to the meridional wind stress (Miyama et al., 2006). The

wind structure associated with the Yanai wave (Figure 2.3) is in general agreement with Chen and Chen (1993)'s observations of westward-propagating monsoon-related vortices. ASLA and τ_y climatology, along with spatial patterns in coherence (Figure 2.2), suggest that the strongest generation likely occurs between $55^\circ - 60^\circ$E, with potential for additional generation across the basin (for example, another area of high coherence is seen east of 80°E). This clarifies some general ambiguity in the literature about the Yanai wave generation location (e.g. Chatterjee et al., 2013; Miyama et al., 2006; Ogata et al., 2008; Sengupta et al., 2004). Moreover, temporal patterns of ASLA and τ_y amplitudes (Figure 2.2) suggest that Yanai waves are generated, primarily, during the monsoon seasons.

2.5 Summary

We present the first analysis of quasi-biweekly Yanai waves in the Indian Ocean that uses only satellite-based observations. The average wavelength and period of the 10–20 day bandpass filtered ASLA and τ_y signals agree ($\lambda \sim 3700$ km, T $\sim$ 14 days), and further analyses imply that the Yanai wave is a linear response to the meridional wind stress. Correlation analysis and phase-averaged composites suggest that the wave has characteristics corresponding to the first two vertical modes, though its properties resemble more closely those of the theoretical second mode. Climatology and cross-spectral analysis indicate that Yanai waves have a seasonal cycle, with the strongest signals present during the summer and winter monsoons; moreover, these analyses suggest that the western equatorial Indian Ocean is a primary generation site, although the reasons for this are unclear. The information gathered from these observations validate what has been deduced from numerical simulations, as well as shed light on potential upwelling and primary productivity patterns in the Indian Ocean. Moreover, the method employed for these composites can be used for future studies on the sea surface temperature signal and primary productivity associated with quasi-biweekly Yanai waves, as well as studies on longer period Yanai waves.

Acknowledgments

This study was conducted using publicly available data from the E.U. Copernicus Marine Environment Monitoring Service (CMEMS, 2019) and NASA's Physical Oceanography Distributed Active Archive Center (NASA/GSFC/NOAA, 2009). Funding was provided by the Office of Naval Research– under the NASCar DRI (Terri Paluskiewicz and Scott Harper), projects N00014-15-1-2303 and N00014-15-1-2319. I. B. Arzeno has also been funded through the National Defense Science & Engineering Graduate Fellowship (NDSEG) Program, as well as the Ford Foundation Dissertation Fellowship.

Chapter 2, in full, has been submitted for publication of the material as it may appear in Geophysical Research Letters (2020), by I. B. Arzeno, S. N. Giddings, G. Pawlak, and R. Pinkel. The dissertation author was the primary investigator and author of this paper.

Appendix A: Estimating Wavenumbers via Slope Spectra

Let F and G represent the Fourier transforms of the sea surface ($\overline{\mathrm{ASLA}(t)}$) and sea surface slope ($\mathrm{dASLA}/\mathrm{d}x(t)$), respectively. Then,

$$k^2(\omega) = \frac{GG^*}{FF^*}, \tag{2.7}$$

where the asterisk denotes the complex conjugate, allowing wavenumbers (k) to be estimated as a function of frequency (ω) for any region where $\overline{\mathrm{ASLA}(t)}$ and $\mathrm{dASLA}/\mathrm{d}x(t)$ are known (e.g. Pinkel, 1975).

For the purposes of this particular analysis, $\overline{\mathrm{ASLA}(t)}$ is taken to be a spatial average of $\mathrm{ASLA}(x,t)$ over three sections (western, central, and eastern) spanning 20° longitude ($50-70°\mathrm{E}$, $60-80°\mathrm{E}$, and $70-90°\mathrm{E}$). The slope ($\mathrm{dASLA}/\mathrm{d}x(t)$) is estimated by fitting a line to ASLA

(x,t) over each section. The slopes from all linear fits were used, regardless of their goodness of fit (R^2), to simplify the spectral analysis. However, 95% of the fits in our western, central, and eastern region had $R^2 > 0.82, 0.73,$ and 0.74, respectively. A coherence analysis was further performed between $\overline{\text{ASLA}}$ and $\text{dASLA}/\text{d}x$ to evaluate the wavenumbers derived from this method. The wavenumbers plotted in the manuscript correspond to frequencies where $\overline{\text{ASLA}}$ and $\text{dASLA}/\text{d}x$ had a coherence above 0.65 (Figure 2.1). This cutoff was established by averaging the top 5% coherence values among the three regions.

Appendix B: Estimating Uncertainties

B.1: Uncertainties in Measurements

As specified in Section 2, the error variance associated with the CMEMS product is assumed to be white noise with a variance $\sigma^2 = 17$ cm^2. The error in ASLA is, then, estimated via error propagation:

$$\sigma_F^2 = \sum_{i=1}^{N} \left(\frac{\partial F}{\partial \chi_i} \sigma_\chi \right)^2, \tag{2.8}$$

where F is a function of independent variables χ_i and has a standard error σ_F. For every longitude in our domain, a time series of random numbers is generated from a standard normal distribution with a variance corresponding to the instrument noise. This time series (denoted here as D_n) is added to the original data (denoted as D_o). Both D_n and D_o are filtered in time and space, as explained in Section 2 of the manuscript, and their difference $(D_n - D_o)$ is saved. This process is repeated 500 times. The standard deviation of all the differences is used as the final measurement error in our analyses. We applied the same method to the wind stress data.

B.2: Confidence Intervals

When possible, confidence intervals about the mean are formed using propagation of error (equation 2.8) and Student's t-distribution. In some instances, error propagation is not straightforward (e.g. when estimating the phase speed average, where each phase speed has a unique confidence interval, explained in Appendix C). When the error cannot be propagated, upper (lower) bounds for an estimator are found by repeating an estimate using the upper (lower) bounds of the data, resulting in conservative and, potentially, asymmetric confidence intervals.

Appendix C: Estimating Phase Speeds

Phase speeds were estimated through auto-correlations and cross-spectral analysis. Cross-correlations were performed between unique grid point pairs separated a distance of 2,000 km or less, over 50-day time intervals. This was repeated throughout the 17-years of data. For each 50-day cross-correlation, the resulting maximum correlation value, along with the corresponding time lag (δt) and the separation distance between the point pair considered (δx), were saved and assigned a spatial position equal to the average longitude of the point pair, $\langle \text{lon} \rangle$. The resulting δt and δx were binned, according to $\langle \text{lon} \rangle$. Linear fits, weighted by the correlation value, were applied over δt and δx, producing an estimate of phase speed for each 50-day time interval at each longitude bin, with corresponding confidence intervals. Fits with a goodness of fit of $R^2 < 0.8$ (~ 10 % of the fits) were rejected. This R^2 cutoff was selected to minimize fit rejection. A final average phase speed was estimated for each location, using the results from the 50-day correlations over the 17-year time series (60–150 degrees of freedom for each average; Figure 2.2).

Cross-spectral analysis was performed in a similar fashion, between each unique grid point pair that was separated by a distance of 2,000 km or less, over the entire time series (not parsed into 50-day intervals to preserve frequency resolution). As such, the resulting phase

speeds are best shown as an average over the basin. Coherence and phase difference ($\delta\phi$) were saved as a function of frequency and assigned a spatial position equal to the average longitude of the point pair, $\langle \text{lon} \rangle$. The resulting $\delta\phi$ and the corresponding separation distance (δx) were binned, according to $\langle \text{lon} \rangle$. Linear fits, weighted by coherence value, were applied over $\delta\phi$ and δx, resulting in a wavenumber estimate ($k = \delta\phi/\delta x$) for each frequency, and, subsequently, a phase speed ($c = \omega/k$), where ω is the frequency. Linear fits with $R^2 < 0.95$ (~ 6 % of the fits) were rejected. A final average phase speed was estimated, using the values resulting from the linear fits for 10–20 day periods (Figure 2.2j).

Chapter 3

Generation of low-latitude seamount-trapped waves: a case study of the Seychelles Plateau

Abstract

Seamount-trapped waves are thought to influence their surrounding ecosystem; however, trapped waves are not well-studied in near-equatorial settings, where stratification is strong and Burger numbers (S) are large. We use daily output (2005-2009) from the global 0.1° Parallel Ocean Program Model 2 (POP2) to examine the presence of topographically-trapped baroclinic waves around the Seychelles Plateau ($S > 100$) in the tropical Indian Ocean. POP2 output shows persistent oscillations propagating anticyclonically around the Seychelles Plateau, with periods of 15–16 days. An idealized stratified seamount-trapped wave model is used to support the existence of trapped waves with similar periods and characteristics akin to higher mode ($m = 4 - 6$, where m is the vertical mode number) internal Kelvin waves. Energy flux maps using POP2 output suggest that equatorial Yanai waves generate the trapped waves on the western and south-western

flanks of the Seychelles Plateau, with most of the energy entering the system near the surface. Anticyclonic energy flux persists throughout the water column and along most of the Plateau circumference, diminishing on the eastern flank of the Plateau, consistent with Yanai wave destructive interference. Current velocity measurements from moorings atop the Plateau contain energy at similar periods to the trapped-wave present in POP2, supporting the existence of such dynamics. Seamount-trapped waves can provide a pathway by which some equatorial planetary wave energy gets redistributed to smaller scales and greater depths.

Plain Language Summary

Internal waves in the vicinity of seamounts are thought to contribute to ecological productivity, yet there is a lack of research on the physical dynamics of these processes around tropical seamounts. For this reason, we use five years (2005–2009) of daily output from the POP2 numerical model to study 15–16 day oscillations around the Seychelles Plateau in the tropical Indian Ocean. We refer to these oscillations as "trapped waves" because they resemble waves that propagate continuously along the Plateau slope, rather than radiating away from the topography, as free waves do. We ran a simplified model with a circular seamount to test whether such waves can exist, given the period and vertical structure exhibited in the POP2 model. We created maps of energy pathways using POP2 output and identified planetary equatorial waves (Yanai waves) as the main driving force for the Plateau-trapped wave. Although Yanai waves mainly input energy into the Plateau system near the western and south-western flanks of the seamount, the Plateau-trapped waves propagate that energy throughout the water column and along the Plateau circumference. Measurements of currents help support the ideas put forth using the numerical model output.

3.1 Introduction

Seamounts have long been lauded as biological hot spots, following evidence that they can retain material such as larvae (Chapman and Haidvogel, 1992; Goldner and Chapman, 1997; Mullineau and Mills, 1997) and support elevated biomass (Clark et al., 2010; Dower et al., 1992; Morato et al., 2010; Rowden et al., 2010b). Seamounts have also been recognized as sites with significant mixing and dissipation (Egbert and Ray, 2003; Lueck and Mudge, 1997; Toole et al., 1997). Although the evidence supporting the biological significance of seamounts is still inconclusive (Rowden et al., 2010a; White et al., 2007), seamounts remain an active area of research due to their ubiquitous nature (Wessel et al., 2010), their potential for bio-physical interactions (Lavelle and Mohn, 2010), and their contributions to mixing and dissipation.

An interesting feature of seamounts is their ability to support anticyclonic topographically-trapped waves that enhance energy from selective subinertial frequencies (Brink, 1990, 1995; Haidvogel et al., 1993). Numerical models show that these trapped waves can be excited by offshore barotropic currents, amplifying energy near the seamount by up to four orders of magnitude, relative to that found in the far-field (Brink, 1990; Haidvogel et al., 1993). The resonance around the seamount is less pronounced and more broad-banded if the offshore currents exciting the trapped wave are horizontally sheared, rather than horizontally uniform (Haidvogel et al., 1993); and the resonant frequency of the seamount need not match the exact frequency of the forcing in order to drive a trapped wave (Codiga, 1997; Haidvogel et al., 1993). Although research suggests that any ambient current may generate seamount-trapped waves, many of the existing observational, analytic, and numerical studies focus on trapped waves generated from tidal interactions (e.g. Brink, 1995; Chapman, 1989; Codiga and Eriksen, 1997; Haidvogel et al., 1993; Hunkins, 1986). Since tidal frequencies are superinertial at low latitudes (hence, not trapped), this also implies that most existing seamount-trapped wave research is focused on mid- and high-latitudes. Hence, there is a gap of research on seamount-trapped waves at low

latitudes, though we can rely on some coastal-trapped wave literature (e.g. Brink, 1982) to guide our understanding.

Low latitudes are characterized by having large baroclinic Rossby radii of deformation (L_R; Chelton et al., 1998). Analogous to coastal-trapped waves (e.g. Huthnance, 1978; Rhines, 1970), the relationship between the topographic lengthscale (L_H) and L_R influences the features of seamount-trapped waves. This relationship is summarized in the Burger number (S),

$$S = \frac{L_R^2}{L_H^2} = \frac{N^2 H^2}{f^2 L_H^2}, \tag{3.1}$$

where H is the water depth, N is the buoyancy frequency, f is the Coriolis parameter, and L_H is taken to be the radius of the plateau. Regions with $S > 0.25$ cannot support barotropic trapped waves; as the Burger number increases further, lower baroclinic modes also cease to be trapped, since their frequencies become superinertial, allowing energy to leak out to the deep ocean (Brink, 1989; Dale and Sherwin, 1996; Huthnance, 1978). Trapped waves with larger Burger numbers ($S \gg 1$, as can be found in the tropics) approximate internal Kelvin waves, rather than shelf waves (Huthnance, 1978; Rhines, 1970).

Here, we discuss the generation of resonant trapped waves around the Seychelles Plateau, a large elliptical seamount in the southwestern equatorial Indian Ocean, extending from approximately 3.5° S to 6.5° S and 53.5°E to 57.5°E (Figure 3.1a). It is an area of interest given its steep slopes of O(0.05), shallow average depth (60–100 m), large size ($\sim$ 200 km x $\sim$ 300 km), and location in a uniquely dynamical tropical ocean. The principal atmospheric driver of the Indian Ocean is the seasonal Indian monsoon; during boreal winter (summer), northeasterly (southwesterly) winds are present over India and veer as they cross the Equator, becoming northwesterly (southeasterly) winds over the Seychelles (Schott and McCreary, 2001; Schott et al., 2009). Arzeno et al. (in review) suggest that equatorial intraseasonal fluctuations in the monsoonal wind stress generate quasi-biweekly (period around 14 days) Yanai waves near the western basin (50–60° E). Sengupta et al. (2004) have observed in their numerical model that

Yanai waves generate coastal-trapped waves upon incidence on eastern boundaries, motivating our examination of the interaction of Indian Ocean Yanai waves with the Seychelles Plateau. Castillo-Trujillo et al. (in prep.) note that most of the variability atop the Seychelles Plateau is found at periods of 10–40 days; at least one of their current velocity instruments showed a peak in energy near periods of 16 days.

As part of the larger North Arabian Sea Circulation autonomous research (NASCar) project (Centurioni et al., 2017) funded by the Office of Naval Research (ONR), our goal is to examine the generation of seamount-trapped waves by equatorial Yanai waves. This paper is organized as follows: in Sections 2 and 3, we provide information on the Parallel Ocean Program (POP2) numerical model used to study the dynamics around the Seychelles Plateau and describe the trapped wave signatures observed in model output, respectively. In Section 4, we make use of an idealized seamount-trapped wave model (Brink, 1989, 2018) to explore the resonant solution to a simplified seamount, comparing that to what is seen in POP2. In Section 5, we estimate energy fluxes using POP2 output, and in Section 6, we briefly comment on current velocity observations taken atop the Plateau. In Section 7, we discuss results and summarize the findings.

3.2 POP2 Model Description

The results from this study are mainly based on output from an atmospheric reanalysis forced coupled ocean/sea ice simulation using CICE4 (Hunke et al., 2010) and the global Los Alamos National Laboratory Parallel Ocean Program Model 2 (POP2), run in the Community Earth System Model (CESM) framework (Hurrell et al., 2013). POP2 is a primitive equation z-coordinate model with a nominal 0.1° horizontal grid and 42 depth levels with a vertical resolution that varies from $\Delta z \sim 10$ m at the surface to $\Delta z \sim 250$ m at depth. Construction of the model bathymetry is described in McClean et al. (2011). Surface forcing is taken from the Coordinated Ocean-ice Reference Experiment-II corrected interannual forcing (CORE-II CIAF; Large and

Yeager, 2004, 2009). Density is calculated from the 25-term equation of state for seawater found in McDougall et al. (2003). Vertical mixing is parameterized using the K-profile parameterization (KPP; Large et al., 1994). Subgrid-scale horizontal mixing is parameterized using biharmonic operators, with the values of viscosity and diffusivity scaling with the grid spacing (Maltrud et al., 1998). In these runs, viscosity and diffusivity at the equator are $\nu_0 = -2.7$ x 10^{10} m^4/s and $\kappa_0 = -0.3$ x 10^{10} m^4/s, respectively (Wang et al., 2018). The model was spun up between 1948–1958. There is a free surface, and tides are excluded.

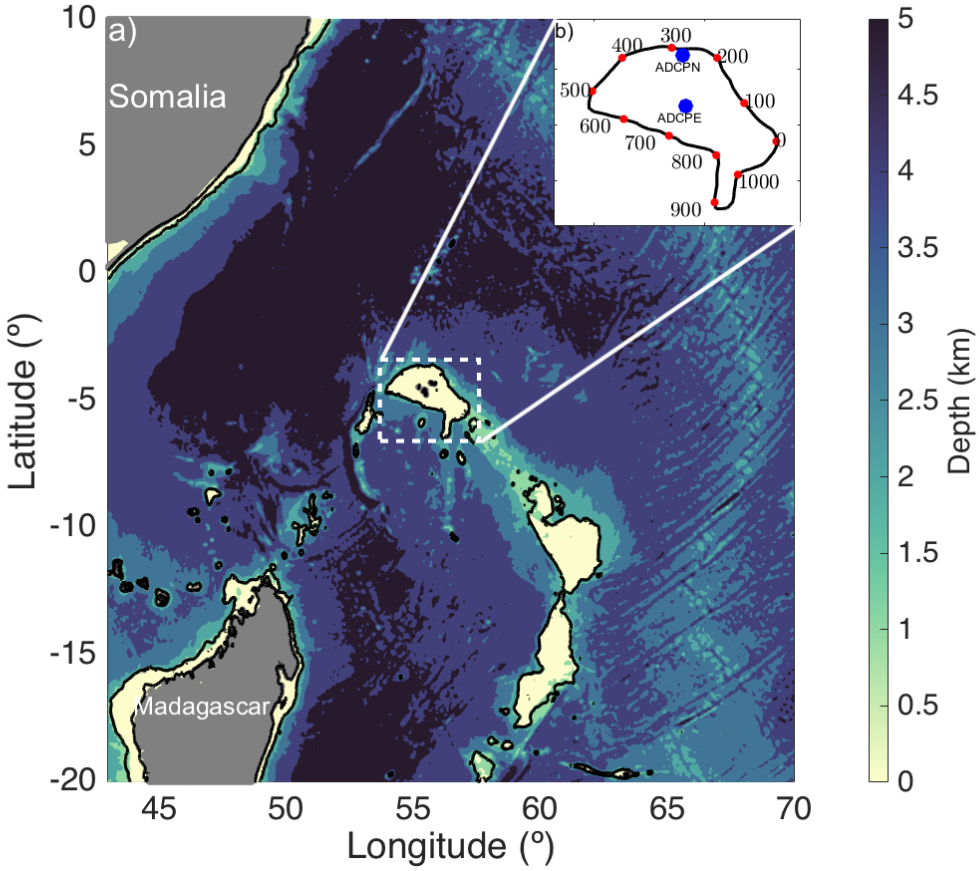

Figure 3.1: (a) Location of the Seychelles Plateau (enclosed by dashed white lines) in the tropical western Indian Ocean. Bathymetry from the ETOPO1 Global Relief Model is shown in color. Black contours delineate the 0- and 1-km isobaths. Land is shaded in grey.(b) Distance (in km) from a southeastern point on the POP2 1-km isobath (black contour). Distance increases counterclockwise around the Plateau. Blue dots shows the locations of current velocity measurements discussed in Section 6.

The POP2/CICE4 model has been recently used in McClean et al. (2018); Palóczy et al. (2018); Wang et al. (2018) and Castillo-Trujillo et al. (in prep.). Wang et al. (2018) validated the POP2 output over the Indian Ocean, north of 5°S, by comparing climatologies of the sea surface height (SSH) field in POP2 with Archiving, Validation, and Interpretation of Satellite Oceanographic (AVISO) altimetry data, provided by Copernicus Marine Environment Monitoring Service (http://www.marine.copernicus.eu). Wang et al. (2018) also compared climatologies of the upper ocean density distribution with the gridded ARGO product (Roemmich and Gilson, 2009). Using both datasets, Wang et al. (2018) saw general agreement between large-scale features of the observations and the POP2 model output. Castillo-Trujillo et al. (in prep.) validate the region of the south-western tropical Indian Ocean by comparing climatologies of AVISO SSH and geostrophic velocities with those found in the POP2 model, focused specifically on the Seychelles Plateau. The model showed stronger geostrophic velocities than those derived from AVISO SSH, and there were slight spatial differences in the location of the SSH anomaly zero-crossings; however, there was overall agreement between the model and observations (Castillo-Trujillo et al., in prep.).

In this study, we use five years of daily averaged POP2 model output from 2005–2009. The model output used is bandpass-filtered with a second-order Butterworth filter to include variations with periods between 10–20 days, to capture dynamics of the quasi-biweekly Yanai wave in the tropical Indian Ocean.

3.3 Overview of POP2 Model Results

3.3.1 Yanai wave

Spectra and composites were formed following the methods in Arzeno et al. (in review) to compare the Yanai wave signal in POP2 model output with the Yanai wave signal in composites constructed using satellite observations (Arzeno et al., in review). Yanai waves are characterized

by their antisymmetric sea level anomalies (ASLA):

$$\mathrm{ASLA} = \frac{1}{2}\left(\mathrm{SLA_n} - \mathrm{SLA_s}\right), \tag{3.2}$$

where $\mathrm{SLA_n}$ and $\mathrm{SLA_s}$ are sea level anomalies averaged meridionally between 2–3°N and 2–3°S, respectively (Yanai and Murakami, 1970). The 2D power spectral density (PSD) of ASLA vertical velocities (dASLA/dt) show enhanced energy in areas intersected by the Yanai wave dispersion curves (Figure 3.2a), suggesting that the model captures the observed quasi-biweekly Yanai wave signal.

We create composites of Yanai wave propagation using sea surface height (SSH). Each composite (Figure 3.2 c–h) was formed by averaging 10–20-day bandpass-filtered time series, at each available grid point, as a function of phase (ϕ). A time series $\Theta_Y(t)$ was used to determine the phase.

Following Arzeno et al. (in review), $\Theta_Y(t)$ is defined using Hilbert Empirical Orthogonal Function (HEOF) analysis of 10–20 day bandpass-filtered ASLA. The first and second HEOF modes capture 45% and 26% of the variance in model ASLA, respectively, similar to the results in Arzeno et al. (in review) using satellite data (37% and 25% for mode 1 and mode 2, respectively). Given that the first HEOF mode is zonally symmetric (Figure 3.2b) and captures most of the variance, we define $\Theta_Y(t)$ as the amplitude time series of the first HEOF mode, which is assumed to be representative of the Yanai wave signal. One full Yanai wave cycle ($\phi = 0 - 2\pi$) is defined using the time between two peaks in $\Theta_Y(t)$.

Similar to the satellite composites in Arzeno et al. (in review) the phase averaged composites using POP2 output (Figure 3.2 c–h) show the Yanai wave SSH signal progressing westward, as expected from theory. The Yanai wave SSH signal is seen to extend as far west as the Seychelles Plateau, as noted in Arzeno et al. (in review). The composite amplitudes are notably lower in the western basin, a concept discussed in Sengupta et al. (2004) as eastern intensification. The Yanai wavelength and period at 2.5°S are $\lambda \sim 4600$ km and $T = 13.4 \pm 0.4$ days, respectively,

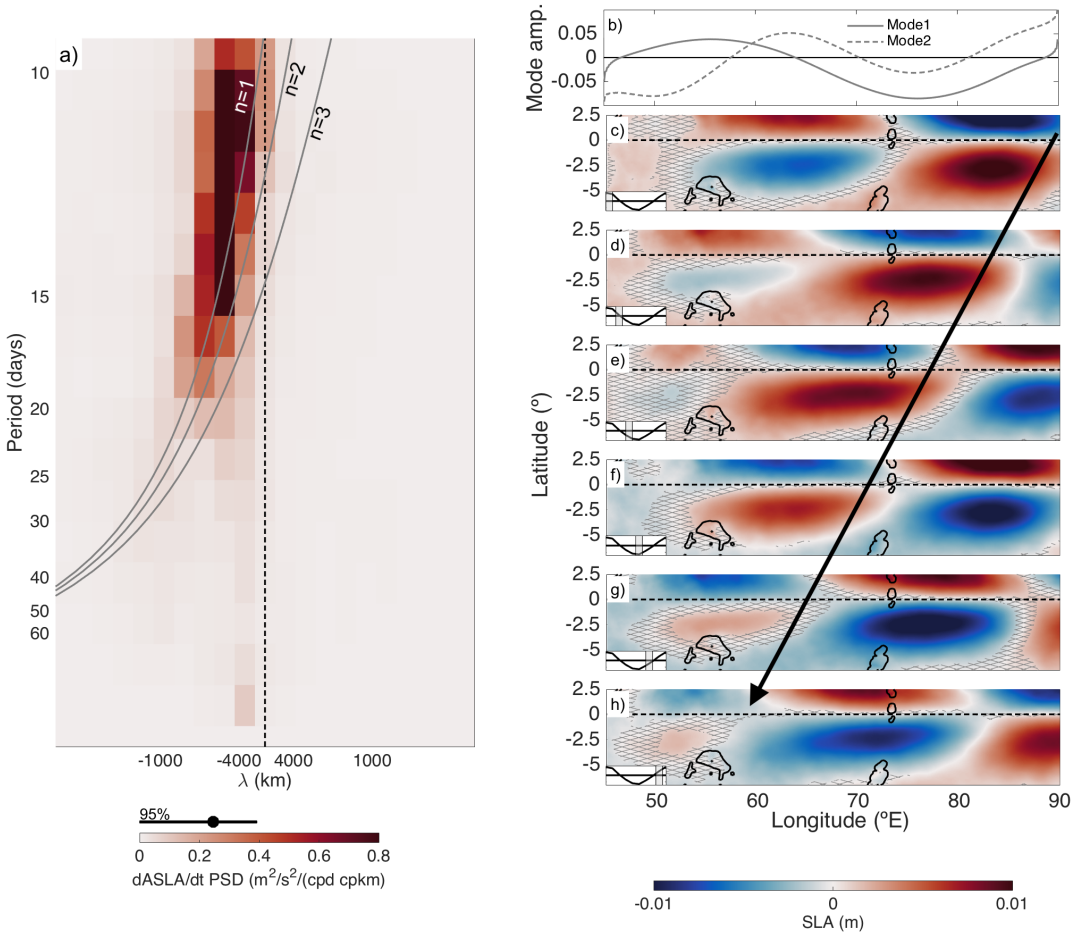

Figure 3.2: (a) 2D power spectral density (PSD) of ASLA vertical velocity (dASLA/dt), with dispersion curves for the first three Yanai wave modes in grey. The 95% confidence interval was estimated following Emery and Thomson (2001). (b) Real part of the spatial amplitude pertaining to the first two ASLA HEOF modes. (c–h) Phase averages of 10–20 day bandpass-filtered POP2 SSH output. Averages were done as a function of the phase of Θ_Y, using the methods described in Arzeno et al. (in review). The insets show the average Θ_Y cycle (solid line) and the phase represented in each subplot (shaded area). The hatching denotes areas where SSH phase averages are not statistically different from zero for a p-value of 0.05. The arrow traces the propagation of a node throughout a cycle. Contours delineate the 0 and 1 km isobaths, from the POP2 model bathymetry.

resulting in a phase speed of $c \sim 4.0$ m/s. The model composite wavelength is similar to that found in satellite data ($\lambda \sim 4100$ km; Arzeno et al., in review). However, the average Yanai wave period and phase speed in the model are shorter and faster than those resulting from composites using satellite data, respectively (T$\sim$ 14 days, $c \sim 3.4$ m/s using satellite data; Arzeno et al., in

review).

3.3.2 Dynamics around the Seychelles Plateau

We shift our attention to the Seychelles Plateau. From here on, all variables discussed will refer to 10–20 day bandpass-filtered time series. The 1-km isobath inside the box in Figure 3.1a is used to demarcate the Seychelles Plateau. Virtual moorings extracted along the 1-km isobath are used to show properties as a function of distance around the Plateau (Figure 3.1b). These time series (discussed as pertaining to the virtual moorings) are actually spatial averages over a ~ 60 km $\times \sim 30$ km area, where the 60 km and 30 km segments cover, roughly, the alongshore and offshore directions.

Temperatures extracted at 150 m along the virtual mooring locations (Figure 3.1b) show periods of oscillations generally propagating anticyclonically around the Seychelles Plateau (Figure 3.3a), interspersed with periods where oscillations seem to impact all moorings simultaneously. The maximum and minimum temperature anomalies at this depth are 0.66°C and -0.71°C, respectively. To further study the dominant characteristics of these oscillations, HEOF analysis was applied to the density time series at the virtual mooring locations. The first HEOF mode captures over 50% of the density variance in the 10–20-day band at depths below 120 m and over 70% of the variance between $z \sim 450$ m and $z \sim 800$ m. At depths below 120 m, the first density HEOF mode has the spatial structure of an azimuthal wavenumber 1 wave, with positive and negative anomalies on opposite sides of the Plateau. HEOF analysis was repeated using density output from the virtual moorings at all depths below 120 m, as opposed to parsing the analysis by depth, as previously done. Following this procedure, the first HEOF mode captures 42% of the variance; the amplitude time series for the first HEOF mode ($\Theta_P(t)$), which we assume is representative of the trapped-wave around the Seychelles Plateau, has bulk and peak periods of 15 and 16 days, respectively.

Composites of temperature and vertical velocity around the Seychelles Plateau were

created as a function of phase, using $\Theta_P(t)$ to determine the phase (Figure 3.3b, c). One full wave cycle ($\phi = 0 - 2\pi$) is defined using the time between two peaks in $\Theta_P(t)$. At ~ 580 m, where HEOF analysis captured over 70% of the variance in its first mode, the trapped wave signature clearly propagates anticylonically (counterclockwise in the southern hemisphere) around the Plateau. Although the temperature signal at this depth is negligible, the vertical velocity is comparable to equatorial upwelling in the Pacific (Johnson et al., 2001) and the monthly upwelling induced by Ekman pumping around the Plateau (Yokoi et al., 2008), which has been linked to elevated chlorophyll patterns (Dilmahamod et al., 2016; Resplandy et al., 2009). Vertical velocities appear to lead the temperature in phase.

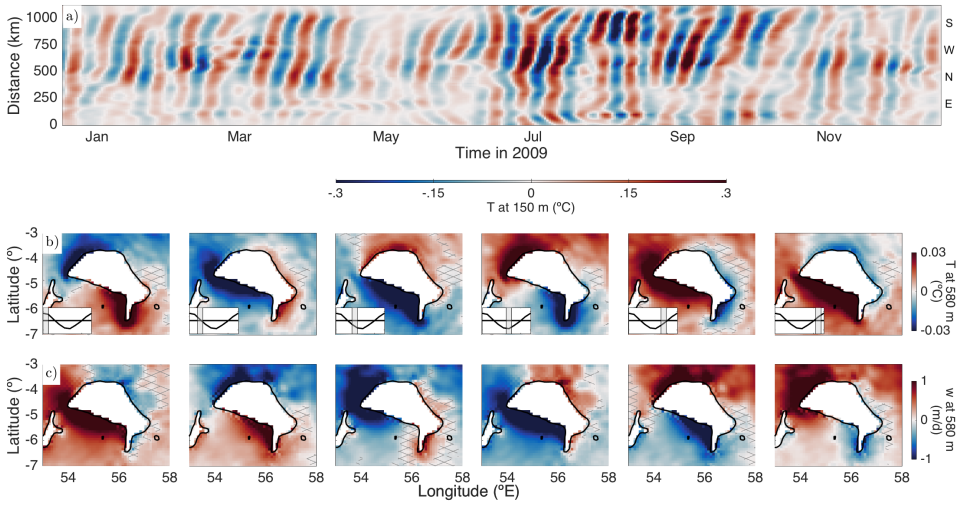

Figure 3.3: (a) Hovmöller diagram of 10–20-day bandpass-filtered temperature anomalies at 150 m, taken over the 1-km isobath. The time series shown span 1 year out of our 5-year model output. Distances around the Plateau are depicted in Figure 3.1b, where 0 km is at the southeast point. General cardinal directions are provided to the right of the Hovmöller diagram to orient the reader with respect to the Plateau. (b-c) Composites of 10–20 day temperature anomalies (b) and vertical velocities (c) at $z \sim 580$ m, created using Θ_P, as explained in Section 3.3. Shaded areas denote regions where the mean is not significantly different from zero for a p-value of 0.05. Insets in row (b) mark the phase of Θ_P corresponding to each column.

The amplitude time series representative of the Yanai wave ($\Theta_Y(t)$) and the oscillations around the Plateau ($\Theta_P(t)$) have a maximum amplitude correlation of $|-0.51| \pm 0.07$ (where the negative indicates an inverse correlation) when $\Theta_P(t)$ lags $\Theta_Y(t)$ by 5 days and the correlation

is weighted by $\Theta_Y(t)$, emphasizing the relationship between the Plateau-trapped wave and the Yanai wave when the Yanai wave has the most energy. The relationship between the Yanai wave and the Plateau oscillations is explored further in Section 5.

3.4 Idealized Seamount-Trapped Wave Model

3.4.1 Idealized Model Setup

To further investigate whether the persistent oscillations around the Seychelles Plateau agree with the theory describing seamount-trapped waves, we compare the characteristics of the signal in our POP2 model output with the results of an idealized stratified seamount-trapped wave model (Brink, 1989, 2018).

The idealized model defines a pressure structure

$$P = P'(r,z)\exp\left[i\left(\omega t + n\theta\right)\right], \tag{3.3}$$

where P is in cylindrical coordinates (r,θ,z), P' is an amplitude, ω is the wave frequency, and n is the azimuthal wavenumber. The model setup is axisymmetric, admits a single stratification and bathymetric profile for the entire domain, and uses the f-plane and Boussinesq approximations. Radial velocities and pressure perturbations decay to zero with distance from the seamount. The model is driven by an arbitrary forcing applied through the surface boundary condition (free surface), and no flow is allowed through the bottom. Although this idealized model has the option to account for the presence of a mean flow and bottom stress, we choose to neglect these for simplicity.

We ran the idealized model using an average bathymetric profile (Figure 3.4a), estimated from model bathymetry. Each cross-section is normal to the model's 1-km contour and extends a distance inward equal to the plateau radius (r_P). We choose $r_P = 160$ km, consistent with the

approximate circumference of the Seychelles plateau at the 1-km isobath. We extracted a total of 129 cross-sections from POP2 (each cross-section spaced 5–15 km apart, covering the entire 1-km contour); however, about half of those cross-sections were eliminated from consideration, due to locally complex bathymetry. For example, we eliminated cross-sections with bathymetry that was never deeper than 3.5 km or cross-sections that intersected shallow protrusions, such as another island or seamount, such that they would make an axisymmetric seamount with a very different structure to the Seychelles Plateau. In the end, we include 80 cross-sections (Figure 3.4b) in our averages.

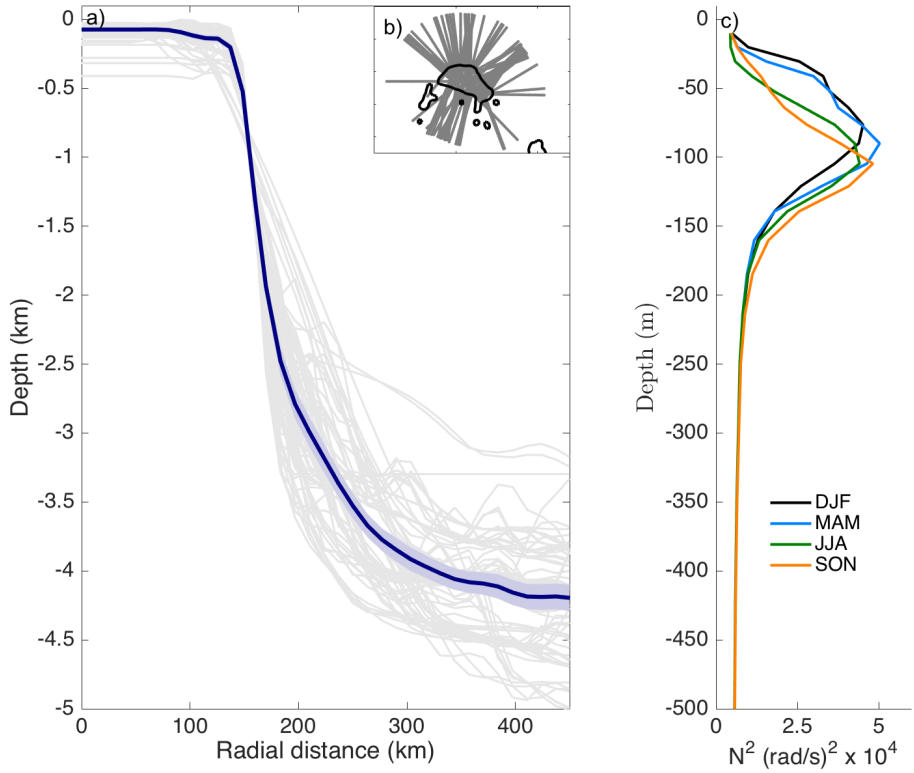

Figure 3.4: (a) Cross-sectional bathymetry from all 80 POP2 cross-sections (grey) and mean bathymetry (blue line) with 95% confidence intervals (blue shading). The mean bathymetry is used in the idealized seamount-trapped wave model. (b) POP2 cross-section locations. (c) Average stratification profiles from POP2 cross-sections, per season.

Stratification profiles (N^2),

Table 3.1: Parameter inputs in the idealized model

Parameter	Values
nn	160, 180, 200
mm	40, 60, 80
[a] f (rad/s) x 10^5	0.941, 1.21, 1.47
L_o (km)	475, 525, 575
[b] T_i (days)	10, 11, 12, 13, 14, 15, 16, 17, 18, 19, 20

[a] The Coriolis frequencies correspond to latitudes $\phi = 3.7°$S, 4.75°S, and 5.8° S, spanning the Plateau.
[b] Period corresponding to the initial frequency guess (ω_i).

$$N^2 = -(g/\rho_0)\,\partial\rho/\partial z \tag{3.4}$$

where $\rho_0 = 1026$ kg/m^3, were also extracted along the same cross-sections. Following Castillo-Trujillo et al. (in prep.), we divide and average our N^2 profiles into four seasons: December–February, March–May, June–August, and September–November. Profiles were also averaged radially and across the 80 cross-sections (Figure 3.4). In general, $N \sim O(10^{-2})$; and seasonal changes in stratification are mainly reflected in the depth of maximum N^2, varying between 75 m (DJF) and 105 m (SON) (Figure 3.4c). Moreover, we varied the number of gridpoints in the horizontal (nn) and vertical (mm), the extent of the outer boundary (L_o), the Coriolis frequency (f), and the initial guesses for the resonant frequency (ω_i). The various parameter values are shown in Table 3.1.

The model admits only anticyclonic subinertial wave solutions and solves for a resonance frequency (ω, with nominal accuracy of 0.1%) using iteration, given a fixed azimuthal wavenumber (following the results presented in Section 3, we look specifically for an azimuthal mode 1 wave). The idealized model outputs a modal structure for each resonant frequency corresponding to the input parameters. We neglect any results that are sensitive to L_o, nn, or mm (i.e., we neglect results where a change in these parameters caused a change in the resonant period by over half a day, which is a 5% change for our lowest period, 10 days).

3.4.2 Idealized Model Results

According to the idealized model, a circularly symmetric seamount with characteristics similar to the Seychelles Plateau should support the existence of azimuthal wavenumber 1 trapped waves with periods between 10–20 days and vertical mode numbers $m = 4 - 6$ (Figure 3.5a). The vertical mode number is estimated as the number of zero crossings in the seamount bottom velocity (and not the number of zero-crossings in a vertical profile, away from the seamount, as noted in Brink (2018)). The bulk and peak periods found from the HEOF analysis around the Plateau suggests that the oscillations in Figure 3.3 could be attributed to an $m = 5$ or an $m = 6$ baroclinic seamount-trapped wave.

The resonant period in the idealized model varies with changes in Burger number (Figure 3.5). Burger numbers (S; equation 3.1) were estimated using $L_H = r_p = 160$ km (the radius of the plateau in the idealized model), $H = 4$ km, varying f (Table 3.1), and the depth-median value of the four average stratification profiles (Figure 3.4b). Coriolis frequency is the main parameter influencing S in this study (Figure 3.5b), as changes in f vary S significantly more than changes in N. Given our large S ($S \gg 1$), we expect trapped waves in these frequencies to exist as higher modes (see, for example, Figure 4 in Brink (1989)), since lower modes (higher frequencies) are superinertial and not trapped. The large S also suggests that the trapped waves around the Seychelles Plateau are likely to behave like internal Kelvin waves (Huthnance, 1978; Rhines, 1970).

Kelvin wave characteristics are apparent in the nearly horizontal isopleths output in the idealized model alongshore velocity modal structure (Figure 3.6, top left). For comparison, alongshore velocities were extracted from four sets of POP2 cross-sections spaced ~ 250 km apart (Figure 3.6 top right). Each set of alongshore velocities is obtained from five cross-sections covering a distance of 50 km in the alongshore direction. The cross-sections in each set were averaged to spatially smooth the data. An empirical orthogonal function (EOF) analysis was performed across each average cross-section to extract the modal structures of the alongshore

velocity. The first and second EOFs accounted for 33–36% and 13–21% of the variance, respectively. The spatial EOF structures in all four sections are more complex than the modal structure presented in the idealized model (Figure 3.6); bathymetry seems to play a crucial role. The modal structure in the idealized model has a zero-crossing atop the Plateau that is captured by the second EOF mode in all four POP2 cross-sections. However, in general, the modal structures do not fully agree between the idealized model and the POP2 cross-sections; the azimuthal velocities across the four POP2 sections show $m \sim 2$ or $m \sim 3$ wave structures. The third EOF (not shown) consists of lower vertical modes.

The idealized model could be estimating an incorrect modal structure, such as seen in

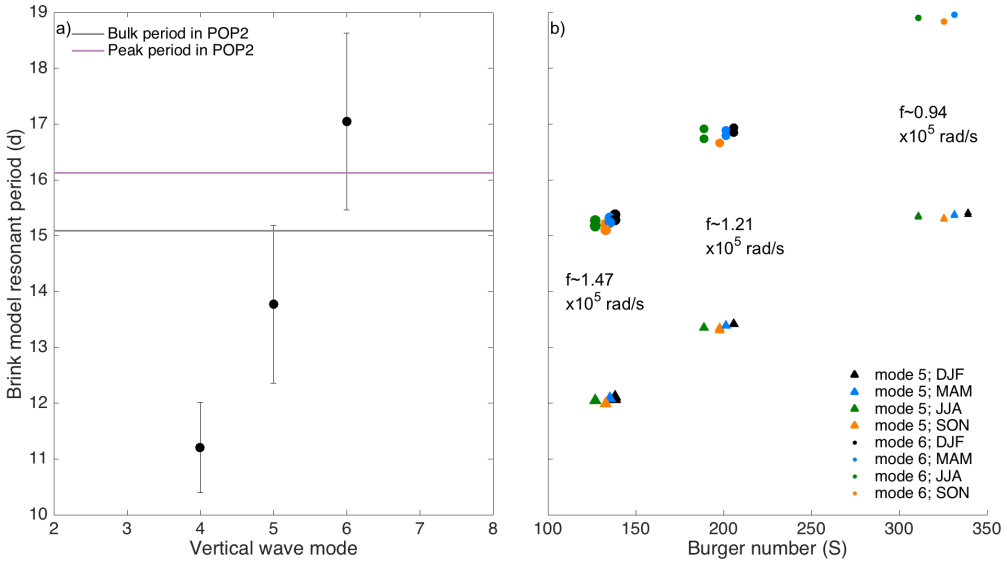

Figure 3.5: (a) Mean resonant period corresponding to the various vertical modal structures given by the idealized model. Error bars represent one standard deviation. Each average is done over 24–40 resonant periods. Horizontal lines mark the average bulk and peak periods of the 10–20 day POP2 HEOF structure described in Section 2, along with 95% confidence intervals (shaded). (b) Resonant periods corresponding to vertical modes 5 and 6, as a function of Burger number ($S = N^2H^2/\left(f^2L^2\right)$). Colors represent the different stratification profiles used in the idealized model (see Figure 3.4). There are multiple resonant periods for each combination of N^2 and f, corresponding to different initial guesses; some of these dots rest on top of each other and are not visible if different initial guesses result in the same resonant period. The size of the marker corresponds to the magnitude of the Coriolis parameters used for each run represented on the plot. The Coriolis parameter magnitude corresponding to each grouping is also noted.

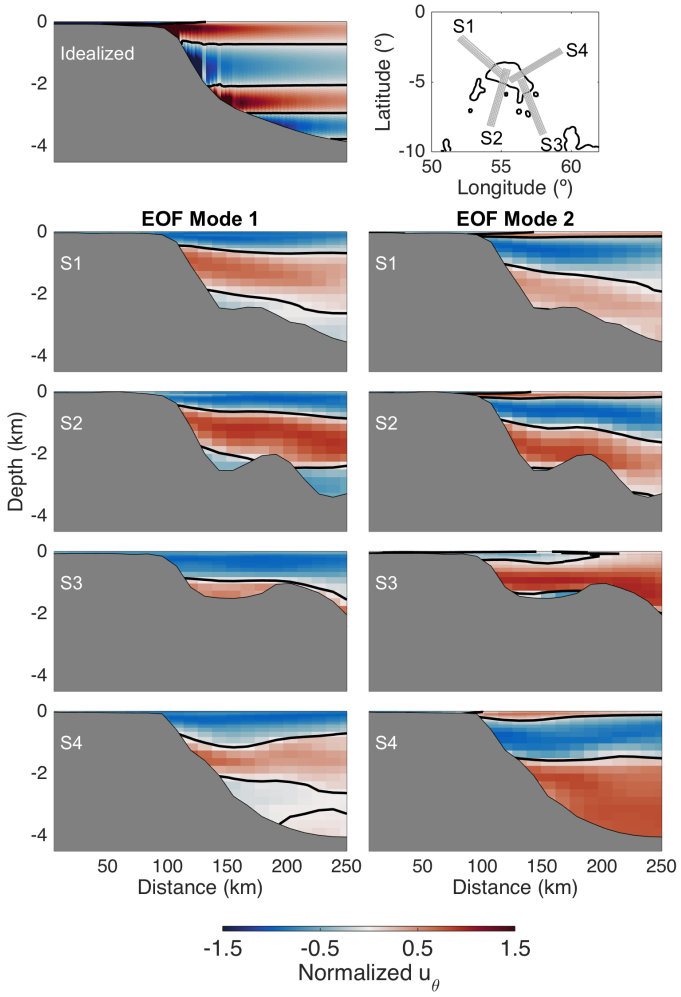

Figure 3.6: Azimuthal velocity (u_θ) modal structures from the idealized seamount-trapped wave model (top left) and four sets of cross-sections around the Seychelles Plateau 1-km isobath (cross-section locations are shown in grey in the top right plot, with the 1-km isobath contoured in black). The structure from the idealized model is a mode $m = 5$ wave, with one zero-crossing near the top of the Plateau and another near the very bottom. Modal structures from the POP2 cross-sections (rows 2–5) are found with empirical orthogonal function (EOF) analysis. Azimuthal velocities are normalized by the maximum value in each cross-section, such that all cross-sections can be portrayed with one color scale.

Brink (1982) and Brink (1999). This is supported by the disagreement between the estimated phase speeds in POP2 and those expected from an internal mode $m = 5$ or $m = 6$ Kelvin wave. Chelton et al. (1998)'s estimates of first baroclinic gravity wave phase speeds near the Seychelles Plateau ($c_1 = 2.8$ m/s) suggest that internal Kelvin waves with modes $m = 5$ and $m = 6$ should have phase speeds of $c_5 = 0.56$ m/s and $c_6 = 0.47$ m/s, respectively. However, taking a wavelength

$\lambda \sim 1000$ km and periods of $T \sim 15$ days and $T \sim 16$ days, we estimate that the wave around the Seychelles Plateau travels with a phase speed of $c_P \sim 0.77$ m/s and $c_P \sim 0.72$ m/s, respectively, faster than the estimates for an internal Kelvin wave of either mode. Brink (1999) found that the estimated resonant frequencies using a circularly symmetric bathymetry are higher than what is expected for an elliptical geometry, such as the Seychelles Plateau. Thus, it is possible that the resonant period for the Seychelles Plateau corresponds to a mode $m = 4$ wave, which is estimated to have a higher frequency in the idealized model. The phase speed for a mode 4 internal Kelvin wave is $c_4 = 0.70$ m/s, closer to c_P, estimated for a wave around the Plateau. The differences between the modal structures in POP2 and the idealized model could also be attributed to variations in the stratification profile and the bathymetry, as well as our neglect of friction and mean currents. Regardless, the idealized model confirms that a trapped wave with periods close to 15 days should exhibit characteristics of a higher mode internal Kelvin wave.

3.5 Energy Flux

We use POP2 model output to examine 10–20 day horizontal energy fluxes in the tropical Indian Ocean to (1) further understand the connection between Yanai waves and trapped waves around the Seychelles Plateau, as well as (2) comment on energy redistribution around the Plateau. For our purposes, we define energy flux (F) as pressure work:

$$F_i = \left\langle u_i' p' \right\rangle, \tag{3.5}$$

where u_i' and p' are the baroclinic velocity and baroclinic pressure perturbation at a certain depth, respectively, and $\langle\rangle$ represents a mean over a wave period. The baroclinic pressure perturbations are deduced from a vertical integral of density anomalies associated with the wave. Following Kunze et al. (2002) and MacKinnon and Gregg (2003),

$$p'(z) = \frac{g}{\rho_0}\left[\int_z^0 \rho'(z^*)dz^* - \frac{1}{H}\int_{-H}^0\int_z^0 \rho'(z^*)dz^*dz\right], \tag{3.6}$$

where the primes denote perturbations associated with the wave, H is bathymetry, $\rho_0 = 1026$ kg/m^3, and the asterisks denote dummy variables. Baroclinic velocities are defined as deviations from the depth-averaged velocity:

$$u_i'(z) = u_i(z) - \frac{1}{H}\int_{-H}^0 u_i(z)dz. \tag{3.7}$$

.

While pressure work is often used as analogous to energy flux, Longuet-Higgins (1964) showed that Rossby wave pressure work is not equivalent to energy flux if the energy flux is estimated as $F = Ec_g$, where E is the energy density and c_g is the group velocity. We hypothesize that the same holds for Yanai waves, given that low-frequency Yanai waves behave like Rossby waves. For now, we will proceed using equation (3.6) and discuss the definition of energy flux further in section 7.

Wave-related perturbations were represented using 10–20 -day bandpass-filtered phase-averaged variables. Phase averages were conducted as described in section 3, using $\Theta_Y(t)$ or $\Theta_P(t)$ to determine the phases.

Depth-integrated fluxes—resulting from variables averaged using $\Theta_Y(t)$ and $\Theta_P(t)$ (Figure 3.7)—are eastward near the equator, as expected for a Yanai wave from theory. The magnitude of the horizontal energy flux differs if $\Theta_Y(t)$ or $\Theta_P(t)$ are used to define the temporal phases: $F(x,y)$ estimated using $\Theta_Y(t)$ shows consistent magnitudes above $F \sim 0.2$ W/m eastward of 65° E. If $\Theta_P(t)$ is used, then $F > 0.2$ W/m between $\sim 55°$ E and $\sim 65°$ E, with decaying magnitudes east of that. The similar spatial patterns, as well as previous work by Arzeno et al. (in review) that suggests Yanai wave generation occurs as far west as 50° E, implies that both Figure 3.7a

and Figure 3.7c capture the same Yanai wave structure, with magnitudes highlighting different regions of the same spatially varying wave. Close-ups of the Seychelles Plateau (Figures 3.7b, d) show anticyclonic energy flux, with greater magnitude around the western and south-western sides of the Plateau. The energy flux around the Seychelles Plateau seems to be connected to the energy flux from the Yanai wave. Furthermore, the energy flux on the eastern side of the Seychelles Plateau appears to be diminished by the opposite-signed flux from the Yanai wave. From here on, the baroclinic velocities, pressure perturbations, and energy fluxes discussed will refer to those estimated from phase averages using $\Theta_P(t)$.

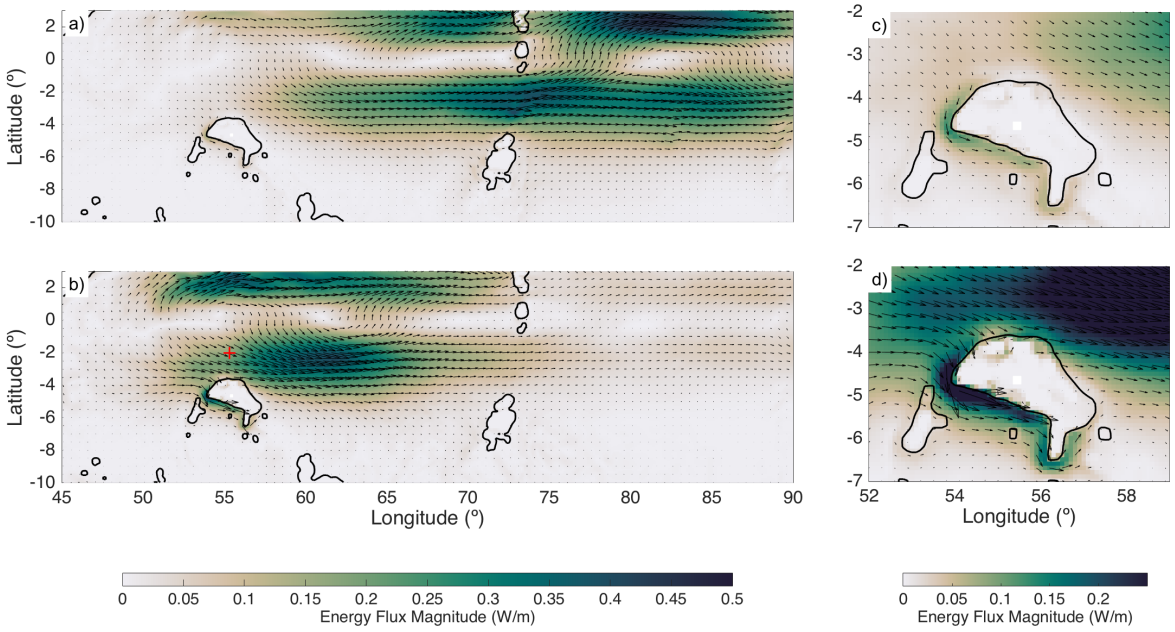

Figure 3.7: Depth-integrated horizontal pressure work (F) estimated from phase averages using (a,b) $\Theta_Y(t)$ or (c,d) $\Theta_P(t)$. Black contour delineates the 1 km isobath in POP2. The red cross denotes the location of the northern pressure measurements in Figure 3.9.

To better understand the energy flux around the plateau, we divide F into azimuthal and radial components (F_θ, F_r), where the azimuthal is defined using the angle of the 1-km isobath. The azimuthal energy flux is positive counterclockwise (the direction of trapped wave propagation), and radial energy flux is positive if energy is entering the Plateau (right-handed coordinate system). Azimuthal and radial energy fluxes were extracted from the virtual moorings

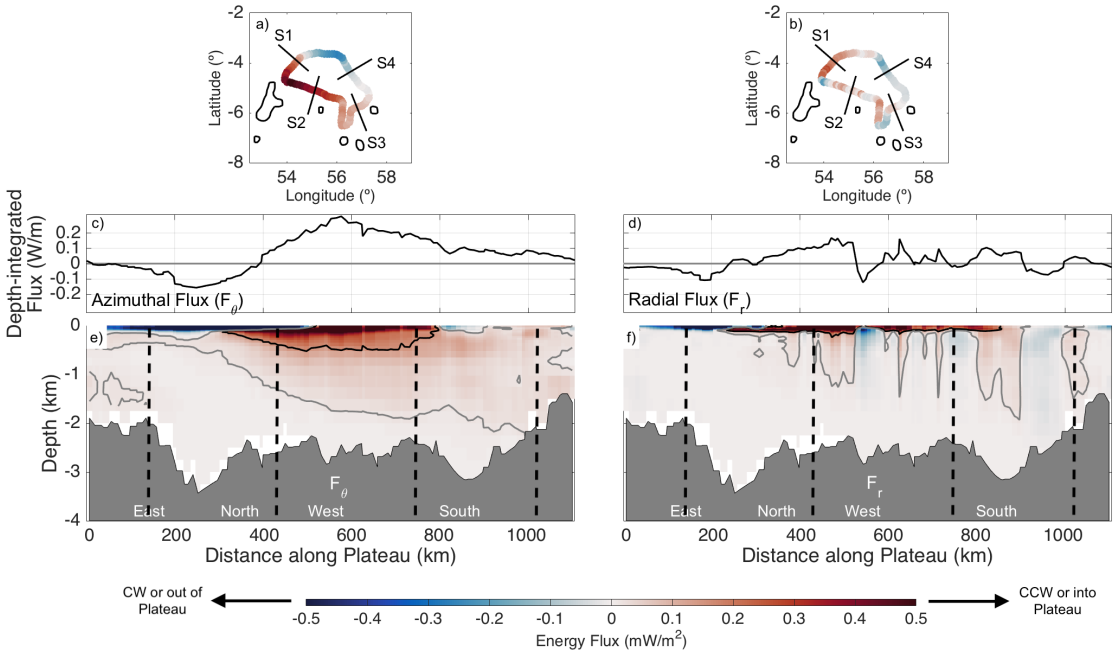

Figure 3.8: Azimuthal and radial energy flux around the Seychelles Plateau integrated over the water column (a–d) and as a function of depth(e,f), with distances depicted in Figure 3.1b. General cardinal directions appear near the bottom to orient the reader. The black and grey contours mark F=0.15 mW/m^2 and F=0.015 mW/m^2, respectively. Solid black lines in (a) and (b) and dashed black lines in (e) and (f) depict the locations of the four sets of cross-sections in Figures 3.3 and 3.10.

on the 1-km isobath (Figure 3.1b), spatially averaged over a $\sim$ 60 km $\times$ $\sim$ 30 km area, as mentioned in section 3.2.

Azimuthal energy flux is mostly positive along the Plateau (Figure 3.8a, 3.8c, 3.8e, with distances specified in Figure 3.1b), suggesting that energy is propagating anticyclonically, as is expected from a seamount-trapped wave. Surface-intensified energy flux stems from the Yanai wave interacting with the Plateau; since the Yanai wave energy flux is eastward, this gets projected (near the surface) unto the Plateau as counterclockwise (positive) and clockwise (negative) energy flux from 600–800 km and 0–600 km, respectively. Radial energy fluxes (Figure 3.8b, 3.8d, 3.8f) show that most of the energy gets injected into the Plateau region over the top 150 m. Azimuthal energy fluxes larger than 0.015 mW/m^2 (Figure 3.8e) extend down into the water column and around most of the Plateau, suggesting that the seamount-trapped wave could be a mechanism by

which surface-intensified Yanai wave energy gets vertically redistributed.

Baroclinic velocities associated with the seamount-trapped wave (not shown) are O(0.01) m/s; these form coherent beams extending along the entire Plateau, with phase propagating upwards, supporting downward energy propagation. Snapshots of baroclinic pressure perturbations (Figure 3.9) also show the beam-like structure below $z \sim 150$ m. Phase-averaged pressure perturbations were extracted from a point just north of the Plateau (red cross in Figure 3.7) as a proxy of the Yanai wave signal. The pressure signal apparent in the top $z \sim 150$ m on the northern and western/southwestern edges of the Plateau matches the Yanai wave pressure signal, showing the connection between the Yanai wave and the trapped wave, as well as potential for signal interference. Integrating Figure 3.8e vertically (Figure 3.8c) and assuming that the southern regions of the Plateau ($\sim$ 800 and 1000 km) are less influenced by the planetary wave suggests that the Yanai wave likely contributes $F_\theta \sim \pm 0.1 - 0.2$ W/m.

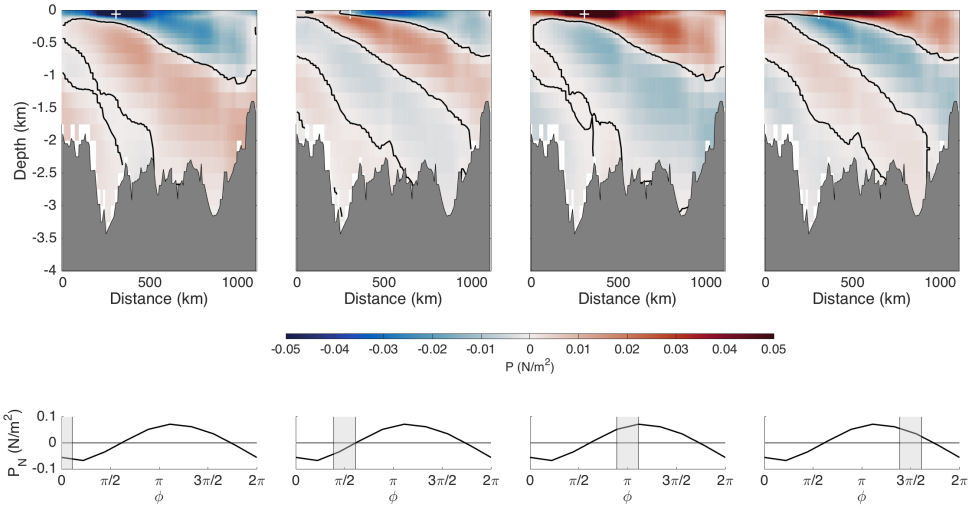

Figure 3.9: Top: Phase-averages of baroclinic pressure perturbations around the Seychelles Plateau 1-km isobath, with distances depicted in Figure 3.1b. Bottom: Baroclinic pressure perturbations from a point north of the Plateau, at 2°S and 55.3°E, depicted in Figure 3.7 with a red cross. Pressure perturbations were extracted at z=150 m. The white cross in the top row shows the corresponding 1-km isobath Plateau location that is due south of the measurements in the bottom row.

Azimuthal energy fluxes along the four sets of cross-sections in Figure 3.6 show the

seamount-trapped wave signal propagating counterclockwise (positive F_θ) around the Plateau (Figure 3.10). The Yanai wave signal is highlighted in both F_θ and F_r. The F_θ contribution from the Yanai wave appears as negative (clockwise) surface-intensified energy flux in S1 and S4. Some of the positive surface-intensified F_θ in S2 can also be attributed to the passing Yanai wave. The F_r contribution from the Yanai wave appears as a positive (into the Plateau) surface-intensified signal in S1 and S2 and as a negative (out of the Plateau) surface-intensified signal in S4. The trapped wave has a narrower cross-sectional extent in S1, where the Yanai wave energy flux direction is opposite that of the trapped wave; and the wave is weak in S4, presumably from destructive interference caused by the Yanai wave.

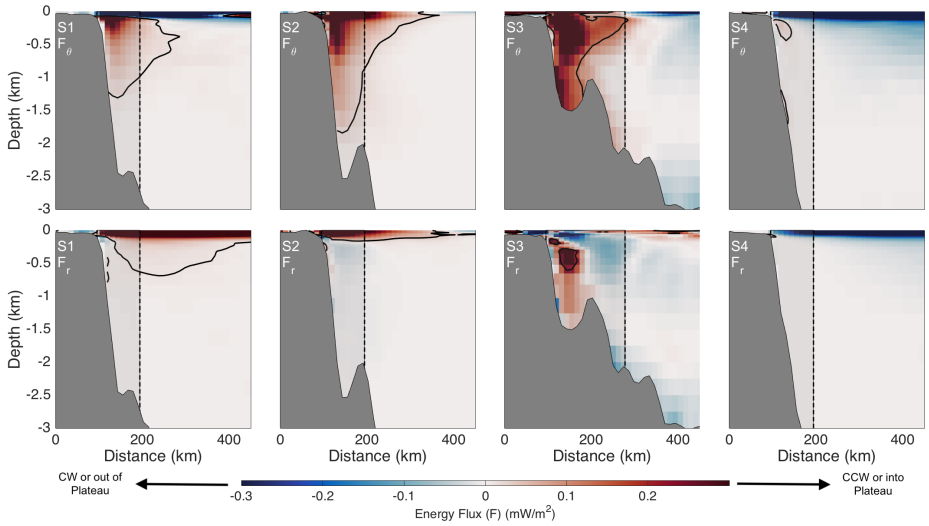

Figure 3.10: Azimuthal (top) and radial (bottom) energy flux across the four cross-section sets in Figure 3.6. Each set consists of 5 individual cross-sections, which we average. Positive F_θ is counterclockwise around the Plateau. The black contour marks $F_\theta = 0.015$ mW/m^2. The shaded region depicts the area over which F_θ is integrated to estimate F_θ^T (equation 3.9).

Assuming that our seamount-trapped wave should behave like a mode 4 internal Kelvin wave (section 4.2), we expect the wave amplitude to extend about a baroclinic Rossby radius away from the Plateau ($L_R \sim 75$ km for a mode 4 wave, if the latitude in consideration is 3.7°S, the northern edge of the Plateau). For each cross-section, we can estimate the total azimuthal energy flux attributed to the trapped wave by vertically integrating F_θ across the entire water

column and radially integrating F_θ from the location of the 200-m isobath (where the Plateau edge generally ends) up to 75-km away from the 1-km isobath (which defines the general Plateau shape). In other words, if L_0 and L_1 are the location of the 200-m and 1-km isobath, respectively, then the total positive azimuthal energy flux (F_θ^T) is

$$F_\theta^T = \int_{L_0}^{L_1+L_R} \int_{-H(r)}^{0} F_\theta(r,z)\,dz\,dr. \tag{3.8}$$

Across the four cross-sections, the total positive azimuthal energy flux ranged $F_\theta^T = 0.73 - 14$ kW, while the integrated radial energy flux (positive and negative along the entire Plateau circumference) totaled 20 kW (Table 3.2), suggesting that dissipation may play an important role in the trapped-wave system. As discussed in section 7, these values depend on having defined the correct angle of rotation and capturing the correct cross-sectional structure of the trapped wave. As such, the numbers are only meant to paint a general picture of the dynamics.

Table 3.2: Integrated Energy Flux (kW)

Section	0 to 380 m	380 m to 1380 m	1380 m to 2500 m	All z
F_θ Section 1	6.4	3.6	0.22	9.4
F_θ Section 2	8.9	5.6	1.2	14
F_θ Section 3	2.4	2.9	1.9	6.4
F_θ Section 4	0.26	0.38	0.28	0.73
F_R^a	17	3.9	-1.1	20

[a] Integrated along entire Plateau circumference.

To examine whether the seamount-trapped wave may impact energy redistribution in the vertical plane, we look at the integrated azimuthal and radial energy flux across three segments of the water column (chosen based on the vertical distribution of radial energy flux in Figure 3.11). Most of the radial energy flux enters the system in the top 380 m (Figure 3.11 and Table 3.2). However, the radial energy flux is outward (negative) below $z \sim -1380$ m, whereas azimuthal energy continues to be fluxed anticyclonically at those depths in all four cross-sections (Figure

3.10 and Table 3.2), implying that energy is not entering the system locally at depth; rather, energy at depth likely stems from the trapped wave dynamics.

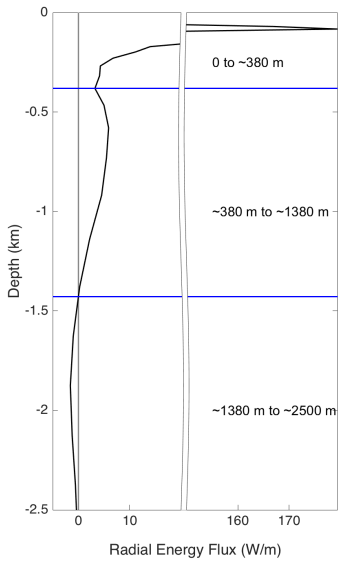

Figure 3.11: Radial energy flux integrated along the Plateau circumference (defined by the 1-km isobath, as in Figure 3.1b). Blue horizontal lines divide three depth ranges that appear distinct because they are bounded by (i) a local minimum or (ii) a zero crossing in the radial energy flux. These depth ranges are referenced in Table 3.2.

3.6 Local Observations

Observations gathered over the Seychelles Plateau (Figure 3.1b) show energy at quasi-biweekly periods, potentially supporting the existence of trapped waves. As part of the ONR NASCar research initiative (Castillo-Trujillo et al., in prep.; Centurioni et al., 2017), current velocities were measured near the northern edge of the Seychelles Plateau, as well as near the central island of Mahé using 300 kHz and 600 kHz RD Instruments acoustic Doppler current profilers (from here on referred to as ADCPN and ADCPE, respectively). ADCPN was moored 4.7 m above the bottom, on the 52-m isobath and sampled for $\sim$ 3 months in 2018, while ADCPE was bottom-mounted on the 30-m isobath and sampled for $\sim$ 30 months between 2015 and 2019.

Both ADCPs sampled at 0.5 Hz. ADCPN and ADCPE resolved velocity profiles in 2 m and 1.5 m vertical bins, respectively.

Time series were averaged in 17-minute blocks of time, with 50% overlap. Depth-averaged currents (bandpass-filtered to retain 10–20 day variability) at ADCPN and ADCPE reach magnitudes near 8 cm/s and 19 cm/s, respectively. Depth-averaged rotary spectra peak near the 15-day period and show more anticyclonic than cyclonic energy at ADCPE, in agreement with Codiga (1993)'s findings, concluding that the dominant balance on the Plateau is inertial in the presence of seamount-trapped waves. Rotary spectra at ADCPN show nearly equal energy at cyclonic and anticylonic orientations. It is possible that (a) ADCPN is detecting the Yanai wave signature, rather than motions associated with a seamount-trapped wave or (b) that the ADPCN time series is too short to properly capture the seamount-trapped wave signal that Codiga (1993) describes. However, this current velocity data encourages future observations around the Plateau edge.

3.7 Discussion and Conclusion

Previous studies on seamount-trapped wave dynamics have focused on regions outside of the tropics, where Burgers numbers are relatively small and trapped waves can be excited by tidal currents (e.g. Brink, 1995; Codiga and Eriksen, 1997; Hunkins, 1986). This study examines trapped waves around the Seychelles Plateau, located in the tropical Indian Ocean, a low-latitude, high Burger number environment. Exploring the role of seamount-trapped waves in the energy pathway is particularly relevant considering that equatorial regions are noted to have low dissipation and diapycnal diffusivity rates (Gregg et al., 2003; Kunze et al., 2006). Seamount-trapped waves such as those found around the Seychelles Plateau may play an important role in transferring energy from larger planetary wave scales to smaller wavelengths.

The magnitude of the seamount-trapped wave azimuthal energy flux around the Seychelles

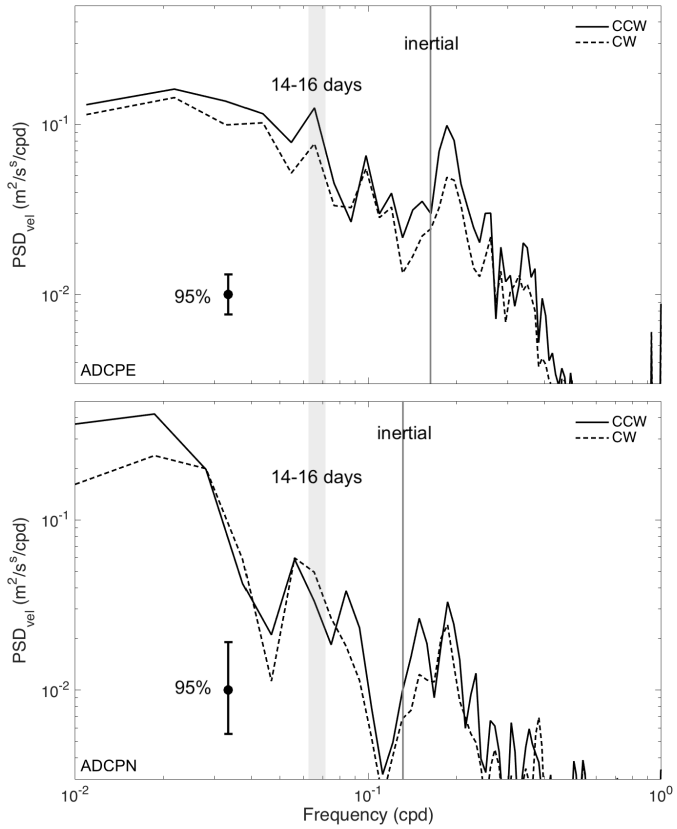

Figure 3.12: Rotary spectra of depth-averaged ADCPE (top) and ADCPN (bottom) velocities, with 95% confidence intervals. Frequencies corresponding to 14–16 day periods are shaded in grey. The local inertial frequency for each ADCP is marked by a grey vertical line.

Plateau is comparable to average downward vertical energy flux estimates for Yanai waves in the Indian and Pacific Oceans (Eriksen and Richman, 1988; Smyth et al., 2015) and to near-inertial windwork in the Indian Ocean (Alford, 2001, 2003). However, the azimuthal energy flux around the Seychelles Plateau is 2–3 orders of magnitude smaller than the zonal energy flux for quasi-biweekly Yanai waves in the Pacific Ocean (Eriksen and Richman, 1988), and there are no measurements of zonal Yanai wave energy flux in the Indian Ocean. Integrating the Yanai wave zonal pressure work in depth and across the equatorial waveguide ($\sim 3^\circ$S to 3°N) yields a pressure work of $F_x \sim 1200$ kW around 55° E. In comparison, the maximum azimuthal energy flux estimated around the Plateau is $F_\theta = 14$ kW (Table 3.2), around 1% of the zonal Yanai wave

pressure work.

Although the pressure work estimated for the seamount-trapped wave is equivalent to the energy flux, the same is not true for Yanai waves. Pressure work in Rossby waves has a non-divergent component that does not contribute to wave energy flux (Durland and Farrar, 2020; Longuet-Higgins, 1964). Using simple scaling, we can estimate the magnitude of the non-divergent term relative to the total pressure work of the Yanai wave. Equation (19) in Durland and Farrar (2020) defines the divergent part of the depth-integrated barotropic pressure work ($\mathbf{S}_d$) as

$$\mathbf{S}_d = gh\eta\mathbf{u} - g^2\hat{\mathbf{e}}_z \times \nabla\left(\frac{h}{f}\frac{\eta^2}{2}\right), \tag{3.9}$$

where h is the water depth, η is the sea surface displacement, $\mathbf{u}$ is the full velocity vector, f is the Coriolis parameter, and $\hat{\mathbf{e}}_z$ is the local vertical unit vector. The second term on the right-hand side (rhs) is the non-divergent part of the full pressure work, while the first term on the rhs is the full pressure work. Although this equation represents a depth-integrated view of the barotropic energy flux, it can be adapted for the baroclinic case. The ratio of the non-divergent to full pressure work can be expressed as

$$R_S \sim g\eta/(2fUL), \tag{3.10}$$

where L is a representative lengthscale by which to scale the gradient, and U is a representative velocity. Taking $g\eta = p'/\rho$, where p' are pressure perturbations, then

$$R_S \sim P'/(2\rho fUL), \tag{3.11}$$

where P' is a representative scale for the Yanai wave pressure perturbations. Since the non-divergent component of the pressure work contains a cross-product, if we are interested in estimating the Yanai wave zonal energy flux, we should consider changes in η^2 in the meridional direction. Taking $L \sim 100$ km as the relevant meridional lengthscale over which η^2 changes (e.g. Figure 3.2), $\rho \sim 1000$ kg/m^3, and $f \sim 1 \times 10^{-6}$ rad/s (the order of magnitude of the Coriolis parameter from about $0.5^\circ - 3.5^\circ$), then the non-divergent term accounts for a hundredth of the total pressure work in the Yanai wave, the same magnitude as the azimuthal energy flux in the seamount-trapped wave. Near the Seychelles Plateau, where $f \sim 1 \times 10^{-5}$ rad/s, the non-divergent component of the pressure work is only a thousandth of the total pressure work; and we can assume that pressure work is an acceptable estimate for the zonal energy flux. Closer to the equator, P' is an order of magnitude smaller than U, but $f \to 0$, and the non-divergent term makes up a larger fraction of the pressure work. Hence, by using pressure work in our study, we are probably under-estimating the total Yanai wave energy flux.

Our estimates of F_θ and F_r around the Plateau are also inexact, since they depend on the angle used to rotate the zonal and meridional components of energy flux. As seen in Figure 3.10, most of the cross-sections show almost no radial energy flux at depth. However, the significant positive (inward) F_r at S3 suggests that the angle of the 1-km isobath is not the correct rotation angle for the azimuthal energy flux at that location. Thus, the total azimuthal energy flux across S3 may be larger than 6.4 kW (Table 3.2). The positive F_r below ~ 500 m shown in Figure 3.8f could also be an artifact of the incorrect rotation. Nonetheless, Figure 3.8 and Figure 3.10 taken together suggest that the trapped wave is a mechanism by which energy input into the system by Yanai waves gets redistributed vertically. Moreover, the F_θ values in Table 3.2 provide a general range of estimates of energy extracted from planetary waves and available for mixing and dissipation in the Plateau system.

We have presented here a segment of the equatorial Indian Ocean energy pathway; energy that is transmitted from the wind to quasi-biweekly Yanai waves (e.g. Arzeno et al., in review;

Sengupta et al., 2004) can become trapped around submarine structures, such as the Seychelles Plateau, before, ultimately, dissipating. Understanding these pathways is particularly relevant to regions of low diapycnal diffusivity, such as the tropics. Moreover, the vertical velocities induced by the trapped wave are on the same order as those resulting from upwelling in the productive Seychelles-Chagos Thermocline Ridge (Yokoi et al., 2008). The trapped wave could contribute to mixing, raising the nutricline and enhancing primary productivity. This work puts forth the need for further measurements in the tropical Indian Ocean to explore the interactions between planetary waves and seamounts near the equatorial waveguide.

Acknowledgments

The work presented here has been carried out with funding from the Office of Naval Research (ONR)– under the NASCar DRI (Terri Paluskiewicz and Scott Harper), projects N00014-15-1-2303, N00014-15-1-2319, and N00014-15-1-2189. The POP simulation used Yellowstone (ark:/85065/d7wd3xhc) computer resources provided by the National Center for Atmospheric Research (NCAR)'s Climate Simulation Laboratory (CSL), sponsored by the National Science Foundation (NSF). I. B. Arzeno has been funded through the National Defense Science & Engineering Graduate Fellowship (NDSEG) Program, as well as the Ford Foundation Dissertation Fellowship. The authors would also like to acknowledge Ken Brink (WHOI) and Rob Pinkel (UCSD-SIO) for their infinitely valuable contributions.

Chapter 3, in full, is currently being prepared for submission for publication of the material to Journal of Geophysical Research: Oceans by I. B. Arzeno, S. N. Giddings, G. Pawlak, J. L. McClean, and H. Wang. The dissertation author was the primary investigator and author of this paper.

Bibliography

Alford, M. H. (2001). Internal swell generation: The spatial distribution of energy flux from the wind to mixed layer near-inertial motions. *Journal of Physical Oceanography*, 31(8):2359–2368.

Alford, M. H. (2003). Improved global maps and 54-year history of wind-work on ocean inertial motions. *Geophysical Research Letters*, 30(8).

Annamalai, H. and Slingo, J. (2001). Active/break cycles: Diagnosis of the intraseasonal variability of the Asian summer monsoon. *Climate Dynamics*, 18(1-2):85–102.

Arzeno, I. B., Collignon, A., Merrifield, M., Giddings, S. N., and Pawlak, G. (2018). Oceanographic data taken over a fringing coral reef near Makua Beach, Oahu, Hawai'i (2013). *UC San Diego Library Digital Collections*.

Ascani, F., Firing, E., Dutrieux, P., McCreary, J. P., and Ishida, A. (2010). Deep equatorial ocean circulation induced by a forced–dissipated Yanai beam. *Journal of Physical Oceanography*, 40(5):1118–1142.

Atlas, R., Hoffman, R. N., Ardizzone, J., Leidner, S. M., Jusem, J. C., Smith, D. K., and Gombos, D. (2011). A cross-calibrated, multiplatform ocean surface wind velocity product for meteorological and oceanographic applications. *Bulletin of the American Meteorological Society*, 92(2):157–174.

Barnett, T. (1983). Interaction of the monsoon and Pacific trade wind system at interannual time scales part I: The equatorial zone. *Monthly Weather Review*, 111(4):756–773.

Beal, L. M., Hormann, V., Lumpkin, R., and Foltz, G. (2013). The response of the surface circulation of the Arabian Sea to monsoonal forcing. *Journal of Physical Oceanography*, 43(9):2008–2022.

Black, K. P. (1993). The relative importance of local retention and inter-reef dispersal of neutrally buoyant material on coral reefs. *Coral Reefs*, 12(1):43–53.

Brink, K. (1982). A comparison of long coastal trapped wave theory with observations off Peru. *Journal of Physical Oceanography*, 12(8):897–913.

Brink, K. (1989). The effect of stratification on seamount-trapped waves. *Deep Sea Research Part A. Oceanographic Research Papers*, 36(6):825–844.

Brink, K. (1990). On the generation of seamount-trapped waves. *Deep Sea Research Part A. Oceanographic Research Papers*, 37(10):1569–1582.

Brink, K. (1995). Tidal and lower frequency currents above Fieberling Guyot. *Journal of Geophysical Research: Oceans*, 100(C6):10817–10832.

Brink, K. (1999). Island-trapped waves, with application to observations off Bermuda. *Dynamics of Atmospheres and Oceans*, 29(2-4):93–118.

Brink, K. (2018). Seamount-or lake/basin-trapped waves with stratification, topography, mean flow and bottom friction in Matlab.

Bunge, L., Provost, C., and Kartavtseff, A. (2007). Variability in horizontal current velocities in the central and eastern equatorial Atlantic in 2002. *Journal of Geophysical Research: Oceans*, 112(C2).

Carter, G. S., Merrifield, M., Becker, J. M., Katsumata, K., Gregg, M., Luther, D., Levine, M., Boyd, T. J., and Firing, Y. (2008). Energetics of M_2 barotropic-to-baroclinic tidal conversion at the Hawaiian Islands. *Journal of Physical Oceanography*, 38(10):2205–2223.

Centurioni, L. R., Hormann, V., Talley, L. D., Arzeno, I., Beal, L., Caruso, M., Conry, P., Echols, R., Fernando, H. J., Giddings, S. N., Gordon, A., Graber, H., Harcourt, R. R., Jayne, S. R., Jensen, T. G., Lee, C. M., Lermusiaux, P. F., L'Hegaret, P., Lucas, A. J., Mahadevan, A., L., M. J., Pawlak, G., Rainville, L., Riser, S. C., Seo, H., Shcherbina, A. Y., Skyllingstad, E., Sprintall, J., Subrahmanyam, B., Terrill, E., Todd, R. E., Trott, C., Ulloa, H. N., and Wang, H. (2017). Northern Arabian Sea Circulation-Autonomous Research (NASCar): A RESEARCH INITIATIVE BASED ON AUTONOMOUS SENSORS. *Oceanography*, 30(2):74–87.

Chapman, D. C. (1989). Enhanced subinertial diurnal tides over isolated topographic features. *Deep Sea Research Part A. Oceanographic Research Papers*, 36(6):815–824.

Chapman, D. C. and Haidvogel, D. B. (1992). Formation of Taylor caps over a tall isolated seamount in a stratified ocean. *Geophysical & Astrophysical Fluid Dynamics*, 64(1-4):31–65.

Chatterjee, A., Shankar, D., McCreary, J., and Vinayachandran, P. (2013). Yanai waves in the western equatorial Indian Ocean. *Journal of Geophysical Research: Oceans*, 118(3):1556–1570.

Chatterjee, P. and Goswami, B. (2004). Structure, genesis and scale selection of the tropical quasi-biweekly mode. *Quarterly Journal of the Royal Meteorological Society*, 130(599):1171–1194.

Chelton, D. B., DeSzoeke, R. A., Schlax, M. G., El Naggar, K., and Siwertz, N. (1998). Geographical variability of the first baroclinic Rossby radius of deformation. *Journal of Physical Oceanography*, 28(3):433–460.

Chen, T.-C. and Chen, J.-M. (1993). The 10–20-day mode of the 1979 Indian monsoon: Its relation with the time variation of monsoon rainfall. *Monthly Weather Review*, 121(9):2465–2482.

Clark, M. R., Rowden, A. A., Schlacher, T., Williams, A., Consalvey, M., Stocks, K. I., Rogers, A. D., O'Hara, T. D., White, M., Shank, T. M., and Hall-Spencer, J. M. (2010). The ecology of seamounts: structure, function, and human impacts. *Annual Review of Marine Science*, 2:253–278.

CMEMS (2019). Global ocean gridded L4 sea surface heights and derived variables reprocessed (1993-ongoing). http://marine.copernicus.eu/services-portfolio/access-to-products/?option=com_csw&view=details&product_id=SEALEVEL_GLO_PHY_L4_REP_OBSERVATIONS_008_047.

Codiga, D. L. (1993). Laboratory realizations of stratified seamount-trapped waves. *Journal of Physical Oceanography*, 23(9):2053–2071.

Codiga, D. L. (1997). Physics and observational signatures of free, forced, and frictional stratified seamount-trapped waves. *Journal of Geophysical Research: Oceans*, 102(C10):23009–23024.

Codiga, D. L. and Eriksen, C. C. (1997). Observations of low-frequency circulation and amplified subinertial tidal currents at Cobb Seamount. *Journal of Geophysical Research: Oceans*, 102(C10):22993–23007.

Coles, D. (1956). The law of the wake in the turbulent boundary layer. *Journal of Fluid Mechanics*, 1(2):191–226.

Coronado, C., Candela, J., Iglesias-Prieto, R., Sheinbaum, J., López, M., and Ocampo-Torres, F. (2007). On the circulation in the Puerto Morelos fringing reef lagoon. *Coral Reefs*, 26(1):149–163.

Cowen, R. K., Lwiza, K. M., Sponaugle, S., Paris, C. B., and Olson, D. B. (2000). Connectivity of marine populations: open or closed? *Science*, 287(5454):857–859.

Dale, A. C. and Sherwin, T. J. (1996). The extension of baroclinic coastal-trapped wave theory to superinertial frequencies. *Journal of Physical Oceanography*, 26(11):2305–2315.

David, D. T., Kumar, S. P., Byju, P., Sarma, M., Suryanarayana, A., and Murty, V. (2011). Observational evidence of lower-frequency Yanai waves in the central equatorial Indian Ocean. *Journal of Geophysical Research: Oceans*, 116(C6).

Dilmahamod, A., Hermes, J., and Reason, C. (2016). Chlorophyll-a variability in the Seychelles–Chagos Thermocline Ridge: Analysis of a coupled biophysical model. *Journal of Marine Systems*, 154:220–232.

Douillet, P., Ouillon, S., and Cordier, E. (2001). A numerical model for fine suspended sediment transport in the southwest lagoon of New Caledonia. *Coral Reefs*, 20(4):361–372.

Dower, J., Freeland, H., and Juniper, K. (1992). A strong biological response to oceanic flow past Cobb seamount. *Deep Sea Research Part A. Oceanographic Research Papers*, 39(7-8):1139–1145.

Durland, T. S. and Farrar, J. T. (2020). Another note on Rossby wave energy flux. *Journal of Physical Oceanography*, 50(2):531–534.

Egbert, G. D. and Ray, R. D. (2003). Semi-diurnal and diurnal tidal dissipation from TOPEX/Poseidon altimetry. *Geophysical Research Letters*, 30(17).

Emery, W. and Thomson, R. (2001). *Data analysis methods in physical oceanography, Second and revised version*. Elsevier Science BV, Ameterdam, the Netherlands.

Eriksen, C. C. and Richman, J. G. (1988). An estimate of equatorial wave energy flux at 9-to 90-day periods in the central Pacific. *Journal of Geophysical Research: Oceans*, 93(C12):15455–15466.

Farrar, J. T. and Durland, T. S. (2012). Wavenumber–frequency spectra of inertia–gravity and mixed Rossby–gravity waves in the equatorial Pacific Ocean. *Journal of Physical Oceanography*, 42(11):1859–1881.

Fewings, M. R. (2017). Large-scale structure in wind forcing over the California Current System in summer. *Monthly Weather Review*, 145(10):4227–4247.

Fewings, M. R. and Lentz, S. J. (2010). Momentum balances on the inner continental shelf at Martha's Vineyard Coastal Observatory. *Journal of Geophysical Research: Oceans*, 115(C12).

Fu, L.-L. and Cazenave, A. (2000). *Satellite altimetry and earth sciences: a handbook of techniques and applications*, volume 69. Elsevier.

Gerbi, G. P., Trowbridge, J. H., Edson, J. B., Plueddemann, A. J., Terray, E. A., and Fredericks, J. J. (2008). Measurements of momentum and heat transfer across the air–sea interface. *Journal of Physical Oceanography*, 38(5):1054–1072.

Giddings, S. N., Monismith, S. G., Fong, D. A., and Stacey, M. T. (2014). Using depth-normalized coordinates to examine mass transport residual circulation in estuaries with large tidal amplitude relative to the mean depth. *Journal of Physical Oceanography*, 44(1):128–148.

Gilg, M. R. and Hilbish, T. J. (2003). The geography of marine larval dispersal: coupling genetics with fine-scale physical oceanography. *Ecology*, 84(11):2989–2998.

Goldner, D. R. and Chapman, D. C. (1997). Flow and particle motion induced above a tall seamount by steady and tidal background currents. *Deep Sea Research Part I: Oceanographic Research Papers*, 44(5):719–744.

Gove, J. M., McManus, M. A., Neuheimer, A. B., Polovina, J. J., Drazen, J. C., Smith, C. R., Merrifield, M. A., Friedlander, A. M., Ehses, J. S., Young, C. W., Dillon, A. K., and Williams, G. J. (2016). Near-island biological hotspots in barren ocean basins. *Nature communications*, 7(1):1–8.

Grant, W. D. and Madsen, O. S. (1979). Combined wave and current interaction with a rough bottom. *Journal of Geophysical Research: Oceans*, 84(C4):1797–1808.

Grant, W. D. and Madsen, O. S. (1986). The continental-shelf bottom boundary layer. *Annual Review of Fluid Mechanics*, 18(1):265–305.

Green, A. L., Maypa, A. P., Almany, G. R., Rhodes, K. L., Weeks, R., Abesamis, R. A., Gleason, M. G., Mumby, P. J., and White, A. T. (2015). Larval dispersal and movement patterns of coral reef fishes, and implications for marine reserve network design. *Biological Reviews*, 90(4):1215–1247.

Gregg, M. C., Sanford, T. B., and Winkel, D. P. (2003). Reduced mixing from the breaking of internal waves in equatorial waters. *Nature*, 422(6931):513–515.

Haidvogel, D. B., Beckmann, A., Chapman, D. C., and Lin, R.-Q. (1993). Numerical simulation of flow around a tall isolated seamount. Part II: Resonant generation of trapped waves. *Journal of Physical Oceanography*, 23(11):2373–2391.

Hench, J. L., Leichter, J. J., and Monismith, S. G. (2008). Episodic circulation and exchange in a wave-driven coral reef and lagoon system. *Limnology and Oceanography*, 53(6):2681–2694.

Hickey, B. M. (1984). The fluctuating longshore pressure gradient on the Pacific Northwest shelf: A dynamical analysis. *Journal of Physical Oceanography*, 14(2):276–293.

Hitzl, D. E., Chen, Y.-L., and Van Nguyen, H. (2014). Numerical simulations and observations of airflow through the ‘Alenuihāhā Channel, Hawai’i. *Monthly Weather Review*, 142(12):4696–4718.

Holmes, R. M., Moum, J. N., and Thomas, L. N. (2016). Evidence for seafloor-intensified mixing by surface-generated equatorial waves. *Geophysical Research Letters*, 43(3):1202–1210.

Horii, T., Masumoto, Y., Ueki, I., Kumar, S. P., and Mizuno, K. (2011). Intraseasonal vertical velocity variation caused by the equatorial wave in the central equatorial Indian Ocean. *Journal of Geophysical Research: Oceans*, 116(C9).

Hunke, E. C., Lipscomb, W. H., Turner, A. K., Jeffery, N., and Elliott, S. (2010). CICE: the Los Alamos Sea Ice Model documentation and software user’s manual version 4.1 LA-CC-06-012. *T-3 Fluid Dynamics Group, Los Alamos National Laboratory*, 675:500.

Hunkins, K. (1986). Anomalous diurnal tidal currents on the Yermak plateau. *Journal of Marine Research*, 44(1):51–69.

Hurrell, J. W., Holland, M. M., Gent, P. R., Ghan, S., Kay, J. E., Kushner, P. J., Lamarque, J.-F., Large, W. G., Lawrence, D., Lindsay, K., Lipscomb, W. H., Long, M. C., Mahowald, N., Marsh, D. R., Neale, R. B., Rasch, P., Vavrus, S., Vertenstein, M., Bader, D., Collins, W., Hack, J. J., Kiehl, J., and Marshall, S. (2013). The community earth system model: a framework for collaborative research. *Bulletin of the American Meteorological Society*, 94(9):1339–1360.

Huthnance, J. M. (1978). On coastal trapped waves: Analysis and numerical calculation by inverse iteration. *Journal of Physical Oceanography*, 8(1):74–92.

Jaramillo, S. and Pawlak, G. (2011). AUV-based bed roughness mapping over a tropical reef. *Coral Reefs*, 30(1):11–23.

Johnson, G. C., McPhaden, M. J., and Firing, E. (2001). Equatorial Pacific Ocean horizontal velocity, divergence, and upwelling. *Journal of Physical Oceanography*, 31(3):839–849.

Kelly, B. G., Meyers, S. D., and O'Brien, J. J. (1995). On a generating mechanism for Yanai waves and the 25-day oscillation. *Journal of Geophysical Research: Oceans*, 100(C6):10589–10612.

Killworth, P. D., Cipollini, P., Uz, B. M., and Blundell, J. R. (2004). Physical and biological mechanisms for planetary waves observed in satellite-derived chlorophyll. *Journal of Geophysical Research: Oceans*, 109(C7).

Kindle, J. C. and Thompson, J. D. (1989). The 26-and 50-day oscillations in the western Indian Ocean: Model results. *Journal of Geophysical Research: Oceans*, 94(C4):4721–4736.

Kirincich, A. R., Lentz, S. J., and Gerbi, G. P. (2010). Calculating reynolds stresses from ADCP measurements in the presence of surface gravity waves using the cospectra-fit method. *Journal of Atmospheric and Oceanic Technology*, 27(5):889–907.

Kirincich, A. R. and Rosman, J. H. (2011). A comparison of methods for estimating Reynolds stress from ADCP measurements in wavy environments. *Journal of Atmospheric and Oceanic Technology*, 28(11):1539–1553.

Kitheka, J. U. (1997). Coastal tidally-driven circulation and the role of water exchange in the linkage between tropical coastal ecosystems. *Estuarine, Coastal and Shelf Science*, 45(2):177–187.

Kumar, N., Feddersen, F., Uchiyama, Y., McWilliams, J., and O'Reilly, W. (2015). Midshelf to surfzone coupled ROMS–SWAN model data comparison of waves, currents, and temperature: Diagnosis of subtidal forcings and response. *Journal of Physical Oceanography*, 45(6):1464–1490.

Kumar, S. P., David, T. D., Byju, P., Narvekar, J., Yoneyama, K., Nakatani, N., Ishida, A., Horii, T., Masumoto, Y., and Mizuno, K. (2012). Bio-physical coupling and ocean dynamics in the central equatorial Indian Ocean during 2006 Indian Ocean Dipole. *Geophysical Research Letters*, 39(14).

Kunze, E., Firing, E., Hummon, J. M., Chereskin, T. K., and Thurnherr, A. M. (2006). Global abyssal mixing inferred from lowered ADCP shear and CTD strain profiles. *Journal of Physical Oceanography*, 36(8):1553–1576.

Kunze, E., Rosenfeld, L. K., Carter, G. S., and Gregg, M. C. (2002). Internal waves in Monterey submarine canyon. *Journal of Physical Oceanography*, 32(6):1890–1913.

Large, W. G., McWilliams, J. C., and Doney, S. C. (1994). Oceanic vertical mixing: A review and a model with a nonlocal boundary layer parameterization. *Reviews of Geophysics*, 32(4):363–403.

Large, W. G. and Yeager, S. G. (2004). Diurnal to decadal global forcing for ocean and sea-ice models: The data sets and flux climatologies.

Large, W. G. and Yeager, S. G. (2009). The global climatology of an interannually varying air–sea flux data set. *Climate Dynamics*, 33(2-3):341–364.

Lavelle, J. W. and Mohn, C. (2010). Motion, commotion, and biophysical connections at deep ocean seamounts. *Oceanography*, 23(1):90–103.

Lentz, S., Churchill, J., Davis, K., Farrar, J., Pineda, J., and Starczak, V. (2016). The characteristics and dynamics of wave-driven flow across a platform coral reef in the Red Sea. *Journal of Geophysical Research: Oceans*, 121(2):1360–1376.

Lentz, S., Davis, K., Churchill, J., and DeCarlo, T. (2017). Coral reef drag coefficients–water depth dependence. *Journal of Physical Oceanography*, 47(5):1061–1075.

Lentz, S., Guza, R., Elgar, S., Feddersen, F., and Herbers, T. (1999). Momentum balances on the North Carolina inner shelf. *Journal of Geophysical Research: Oceans*, 104(C8):18205–18226.

Lentz, S. and Raubenheimer, B. (1999). Field observations of wave setup. *Journal of Geophysical Research: Oceans*, 104(C11):25867–25875.

Lentz, S. J., Churchill, J. H., and Davis, K. A. (2018). Coral reef drag coefficients—Surface gravity wave enhancement. *Journal of Physical Oceanography*, 48(7):1555–1566.

Li, L. and Chen, Y.-L. (2017). Numerical simulations of two trapped mountain lee waves downstream of Oahu. *Journal of Applied Meteorology and Climatology*, 56(5):1305–1324.

Longuet-Higgins, M. S. (1964). On group velocity and energy flux in planetary wave motions. In *Deep Sea Research and Oceanographic Abstracts*, volume 11, pages 35–42. Elsevier.

Lowe, R. J. and Falter, J. L. (2015). Oceanic forcing of coral reefs. *Annual Review of Marine Science*, 7:43–66.

Lowe, R. J., Falter, J. L., Monismith, S. G., and Atkinson, M. J. (2009a). A numerical study of circulation in a coastal reef-lagoon system. *Journal of Geophysical Research: Oceans*, 114(C6).

Lowe, R. J., Falter, J. L., Monismith, S. G., and Atkinson, M. J. (2009b). Wave-driven circulation of a coastal reef–lagoon system. *Journal of Physical Oceanography*, 39(4):873–893.

Lowe, R. J., Hart, C., and Pattiaratchi, C. B. (2010). Morphological constraints to wave-driven circulation in coastal reef-lagoon systems: A numerical study. *Journal of Geophysical Research: Oceans*, 115(C9).

Lueck, R. G. and Mudge, T. D. (1997). Topographically induced mixing around a shallow seamount. *Science*, 276(5320):1831–1833.

Lyman, J. M., Johnson, G. C., and Kessler, W. S. (2007). Distinct 17-and 33-day tropical instability waves in subsurface observations. *Journal of Physical Oceanography*, 37(4):855–872.

MacKinnon, J. and Gregg, M. (2003). Shear and baroclinic energy flux on the summer New England shelf. *Journal of Physical Oceanography*, 33(7):1462–1475.

Maltrud, M. E., Smith, R. D., Semtner, A. J., and Malone, R. C. (1998). Global eddy-resolving ocean simulations driven by 1985–1995 atmospheric winds. *Journal of Geophysical Research: Oceans*, 103(C13):30825–30853.

Masumoto, Y., Hase, H., Kuroda, Y., Matsuura, H., and Takeuchi, K. (2005). Intraseasonal variability in the upper layer currents observed in the eastern equatorial Indian Ocean. *Geophysical Research Letters*, 32(2).

Masumoto, Y., Horii, T., Ueki, I., Hase, H., Ando, K., and Mizuno, K. (2008). Short-term upper-ocean variability in the central equatorial Indian Ocean during 2006 Indian Ocean Dipole event. *Geophysical Research Letters*, 35(14).

McClean, J. L., Bader, D. C., Bryan, F. O., Maltrud, M. E., Dennis, J. M., Mirin, A. A., Jones, P. W., Kim, Y. Y., Ivanova, D. P., Vertenstein, M., Boyle, J. S., Jacob, R. L., Norton, N., Craig, A., and Worley, P. H. (2011). A prototype two-decade fully-coupled fine-resolution CCSM simulation. *Ocean Modelling*, 39(1-2):10–30.

McClean, J. L., Bader, D. C., Maltrud, M. E., Evans, K. J., Taylor, M., Tang, Q., Ivanova, D., Veneziani, C., Ritchie, J., Branstetter, M. L., and Mahajan, S. (2018). High-resolution fully-coupled acme v0. 1 approximate present day transient climate simulations. In *2018 Ocean Sciences Meeting*. AGU.

McCreary, J. P. (1984). Equatorial beams. *Journal of Marine Research*, 42(2):395–430.

McDonald, C., Koseff, J., and Monismith, S. (2006). Effects of the depth to coral height ratio on drag coefficients for unidirectional flow over coral. *Limnology and Oceanography*, 51(3):1294–1301.

McDougall, T. J., Jackett, D. R., Wright, D. G., and Feistel, R. (2003). Accurate and computationally efficient algorithms for potential temperature and density of seawater. *Journal of Atmospheric and Oceanic Technology*, 20(5):730–741.

Merrifield, M. and Guza, R. (1990). Detecting propagating signals with complex empirical orthogonal functions: A cautionary note. *Journal of Physical Oceanography*, 20(10):1628–1633.

Miyama, T., McCreary, J. P., Sengupta, D., and Senan, R. (2006). Dynamics of biweekly oscillations in the equatorial Indian Ocean. *Journal of Physical Oceanography*, 36(5):827–846.

Monismith, S. G. (2007). Hydrodynamics of coral reefs. *Annuual Review of Fluid Mechanics*, 39:37–55.

Monismith, S. G. (2014). Flow through a rough, shallow reef. *Coral Reefs*, 33(1):99–104.

Moore, D. W. and McCreary, J. P. (1990). Excitation of intermediate-frequency equatorial waves at a western ocean boundary: With application to observations from the Indian Ocean. *Journal of Geophysical Research: Oceans*, 95(C4):5219–5231.

Morato, T., Hoyle, S. D., Allain, V., and Nicol, S. J. (2010). Seamounts are hotspots of pelagic biodiversity in the open ocean. *Proceedings of the National Academy of Sciences*, 107(21):9707–9711.

Mullineau, L. S. and Mills, S. W. (1997). A test of the larval retention hypothesis in seamount-generated flows. *Deep Sea Research Part I: Oceanographic Research Papers*, 44(5):745–770.

Murty, V., Sarma, M., Suryanarayana, A., Sengupta, D., Unnikrishnan, A., Fernando, V., Almeida, A., Khalap, S., Sardar, A., Somasundar, K., and Ravichandran, M. (2006). Indian moorings: Deep-sea current meter moorings in the eastern equatorial Indian Ocean. *CLIVAR Exchanges*, 11(4).

Nagura, M., Masumoto, Y., and Horii, T. (2014). Meridional heat advection due to mixed Rossby-gravity waves in the equatorial Indian Ocean. *Journal of Physical Oceanography*, 44(1).

NASA/GSFC/NOAA (2009). Cross-Calibrated Multi-Platform ocean surface wind vector L3.0 first-look analyses. ver. 1.

Nash, J. D., Kunze, E., Lee, C. M., and Sanford, T. B. (2006). Structure of the baroclinic tide generated at Kaena Ridge, Hawai'i. *Journal of Physical Oceanography*, 36(6):1123–1135.

Nezu, I. and Rodi, W. (1986). Open-channel flow measurements with a laser Doppler anemometer. *Journal of Hydraulic Engineering*, 112(5):335–355.

Nunes, V. and Pawlak, G. (2008). Observations of bed roughness of a coral reef. *Journal of Coastal Research*, pages 39–50.

Ogata, T., Sasaki, H., Murty, V., Sarma, M., and Masumoto, Y. (2008). Intraseasonal meridional current variability in the eastern equatorial Indian Ocean. *Journal of Geophysical Research: Oceans*, 113(C7).

Palóczy, A., Gille, S. T., and McClean, J. L. (2018). Oceanic heat delivery to the Antarctic continental shelf: Large-scale, low-frequency variability. *Journal of Geophysical Research: Oceans*, 123(11):7678–7701.

Pinkel, R. (1975). Upper ocean internal wave observations from FLIP. *Journal of Geophysical Research*, 80(27):3892–3910.

Pujol, M.-I., Faugère, Y., Taburet, G., Dupuy, S., Pelloquin, C., Ablain, M., and Picot, N. (2016). DUACS DT2014: the new multi-mission altimeter data set reprocessed over 20 years. *Ocean Science*, 12(5):1067–1090.

Rao, R., Horii, T., Masumoto, Y., and Mizuno, K. (2017). Observed variability in the upper layers at the Equator, 90 degrees E in the Indian Ocean during 2001–2008, 2: Meridional currents. *Climate Dynamics*, 49(3):1031–1048.

Reidenbach, M. A., Monismith, S. G., Koseff, J. R., Yahel, G., and Genin, A. (2006). Boundary layer turbulence and flow structure over a fringing coral reef. *Limnology and Oceanography*, 51(5):1956–1968.

Resplandy, L., Vialard, J., Lévy, M., Aumont, O., and Dandonneau, Y. (2009). Seasonal and intraseasonal biogeochemical variability in the thermocline ridge of the southern tropical indian ocean. *Journal of Geophysical Research: Oceans*, 114(C7).

Rhines, P. (1970). Edge-, bottom-, and Rossby waves in a rotating stratified fluid. *Geophysical and Astrophysical Fluid Dynamics*, 1(3-4):273–302.

Roemmich, D. and Gilson, J. (2009). The 2004–2008 mean and annual cycle of temperature, salinity, and steric height in the global ocean from the Argo Program. *Progress in Oceanography*, 82(2):81–100.

Rogers, C. S. (1990). Responses of coral reefs and reef organisms to sedimentation. *Marine ecology progress series*, 62(1):185–202.

Rogers, J. S., Maticka, S. A., Chirayath, V., Woodson, C. B., Alonso, J. J., and Monismith, S. G. (2018). Connecting flow over complex terrain to hydrodynamic roughness on a coral reef. *Journal of Physical Oceanography*, 48(7):1567–1587.

Rogers, J. S., Monismith, S. G., Dunbar, R. B., and Koweek, D. (2015). Field observations of wave-driven circulation over spur and groove formations on a coral reef. *Journal of Geophysical Research: Oceans*, 120(1):145–160.

Rosman, J. H. and Hench, J. L. (2011). A framework for understanding drag parameterizations for coral reefs. *Journal of Geophysical Research: Oceans*, 116(C8).

Rowden, A. A., Dower, J. F., Schlacher, T. A., Consalvey, M., and Clark, M. R. (2010a). Paradigms in seamount ecology: fact, fiction and future. *Marine Ecology*, 31:226–241.

Rowden, A. A., Schlacher, T. A., Williams, A., Clark, M. R., Stewart, R., Althaus, F., Bowden, D. A., Consalvey, M., Robinson, W., and Dowdney, J. (2010b). A test of the seamount oasis hypothesis: seamounts support higher epibenthic megafaunal biomass than adjacent slopes. *Marine Ecology*, 31:95–106.

Schott, F. A. and McCreary, J. P. (2001). The monsoon circulation of the Indian Ocean. *Progress in Oceanography*, 51(1):1–123.

Schott, F. A., Xie, S.-P., and McCreary Jr, J. P. (2009). Indian Ocean circulation and climate variability. *Reviews of Geophysics*, 47(1).

Sengupta, D., Senan, R., Murty, V., and Fernando, V. (2004). A biweekly mode in the equatorial Indian Ocean. *Journal of Geophysical Research: Oceans*, 109(C10):1171.

Shinoda, T. (2012). Observation of first and second baroclinic mode Yanai waves in the ocean. *Quarterly Journal of the Royal Meteorological Society*, 138(665):1018–1024.

Smith, K. A., Merrifield, M. A., and Carter, G. S. (2017). Coastal-trapped behavior of the diurnal internal tide at O'ahu, Hawai'i. *Journal of Geophysical Research: Oceans*, 122(5):4257–4273.

Smith, K. A., Rocheleau, G., Merrifield, M. A., Jaramillo, S., and Pawlak, G. (2016). Temperature variability caused by internal tides in the coral reef ecosystem of Hanauma Bay, Hawai'i. *Continental Shelf Research*, 116:1–12.

Smith, S. D. (1988). Coefficients for sea surface wind stress, heat flux, and wind profiles as a function of wind speed and temperature. *Journal of Geophysical Research: Oceans*, 93(C12):15467–15472.

Smyth, W., Durland, T., and Moum, J. (2015). Energy and heat fluxes due to vertically propagating Yanai waves observed in the equatorial Indian Ocean. *Journal of Geophysical Research: Oceans*, 120(1):1–15.

Strutton, P. G., Coles, V., Hood, R., Matear, R., Mcphaden, M., and Phillips, H. (2014). Biogeochemical variability in the equatorial Indian Ocean during the monsoon transition. *Biogeosciences Discussions*, 11:6185–6219.

Strutton, P. G., Ryan, J. P., and Chavez, F. P. (2001). Enhanced chlorophyll associated with tropical instability waves in the equatorial Pacific. *Geophysical Research Letters*, 28(10):2005–2008.

Taburet, G., Sanchez-Roman, A., Ballarotta, M., Pujol, M.-I., Legeais, J.-F., Fournier, F., Faugere, Y., and Dibarboure, G. (2019). DUACS DT2018: 25 years of reprocessed sea level altimetry products. *Ocean Science*, 15(5):1207–1224.

Taebi, S., Lowe, R. J., Pattiaratchi, C. B., Ivey, G. N., Symonds, G., and Brinkman, R. (2011). Nearshore circulation in a tropical fringing reef system. *Journal of Geophysical Research: Oceans*, 116(C2).

Toole, J. M., Schmitt, R. W., Polzin, K. L., and Kunze, E. (1997). Near-boundary mixing above the flanks of a midlatitude seamount. *Journal of Geophysical Research: Oceans*, 102(C1):947–959.

Tsai, P. T., O'Brien, J. J., and Luther, M. E. (1992). The 26-day oscillation observed in the satellite sea surface temperature measurements in the equatorial western Indian Ocean. *Journal of Geophysical Research: Oceans*, 97(C6):9605–9618.

Uz, B. M., Yoder, J. A., and Osychny, V. (2001). Pumping of nutrients to ocean surface waters by the action of propagating planetary waves. *Nature*, 409(6820):597–600.

Wang, H., McClean, J. L., Talley, L. D., and Yeager, S. (2018). Seasonal cycle and annual reversal of the Somali Current in an eddy-resolving global ocean model. *Journal of Geophysical Research: Oceans*, 123(9):6562–6580.

Wessel, P., Sandwell, D. T., and Kim, S.-S. (2010). The global seamount census. *Oceanography*, 23(1):24–33.

White, M., Bashmachnikov, I., Arístegui, J., and Martins, A. (2007). Physical processes and seamount productivity. *Seamounts: Ecology, Fisheries and Conservation*, pages 65–84.

Williams, D. M., Wolanski, E., and Andrews, J. (1984). Transport mechanisms and the potential movement of planktonic larvae in the central region of the Great Barrier Reef. *Coral Reefs*, 3(4):229–236.

Wolanski, E. and Kingsford, M. J. (2014). Oceanographic and behavioural assumptions in models of the fate of coral and coral reef fish larvae. *Journal of The Royal Society Interface*, 11(98):20140209.

Yanai, M. and Murakami, M. (1970). Spectrum analysis of symmetric and antisymmetric equatorial waves. *Journal of the Meteorological Society of Japan. Ser. II*, 48(4):331–347.

Yokoi, T., Tozuka, T., and Yamagata, T. (2008). Seasonal variation of the Seychelles Dome. *Journal of Climate*, 21(15):3740–3754.